

# Squeezing atomic $p$ -orbital condensates for detecting gravitational waves

Xinyang Yu,<sup>1,2</sup> W. Vincent Liu,<sup>3,4</sup> and Xiaopeng Li<sup>1,2,5,6,7,\*</sup>

<sup>1</sup>State Key Laboratory of Surface Physics, Institute of Nanoelectronics and Quantum Computing, and Department of Physics, Fudan University, Shanghai 200433, China

<sup>2</sup>Shanghai Qi Zhi Institute, AI Tower, Xuhui District, Shanghai 200232, China

<sup>3</sup>Department of Physics and Astronomy, University of Pittsburgh, Pittsburgh, PA 15260, USA

<sup>4</sup>International Quantum Academy, Shenzhen 518048, China

<sup>5</sup>Hefei National Laboratory, Hefei 230088, China

<sup>6</sup>Shanghai Artificial Intelligence Laboratory, Shanghai 200232, China

<sup>7</sup>Shanghai Research Center for Quantum Sciences, Shanghai 201315, China

(Dated: November 12, 2024)

Precision gravitational wave measurement transforms research beyond general relativity and cosmology. Advances are made by applying quantum enhanced interferometry into the LIGO, Virgo and KAGRA detectors. Here, we develop an atomic sensor that employs a  $p$ -orbital Bose-Einstein condensate in an optical lattice to project gravitational wave signals into an orbital squeezed state. This entangled state couples linearly to the spacetime distortion signals received via a Michelson interferometer. Simulation data show that this sensor improves sensitivity over LIGO's quantum noise by approximately one order of magnitude and detection volume by  $\sim 10^3$  in key frequency regimes. Additionally, it reduces the required laser power by five orders of magnitude. These results suggest that atomic orbital squeezing offers a compelling alternative to conventional techniques, offering a qualitatively different avenue for gravitational wave-based detection of dark matter, black holes, and the equation of state in neutron stars.

*Introduction*— The successful detection of gravitational wave (GW) by LIGO marks more than a milestone in the three centuries of studying gravity. GWs are a natural prediction of Einstein equations, much like the electromagnetic (EM) waves are the results of Maxwell equations. Just as the advancement of EM wave science and technology has had a profound impact on fields from condensed matter physics, materials science, and chemistry to electrical engineering, precision measurement, navigation, radiation control, medical applications and many more, the discovery of GWs opens unprecedented prospects to influence a similarly broad range of disciplines in the future. A challenge to such exciting prospects is however how to improve the accuracy in measuring the GW, so that the information carried by it can be used to analyze the unknown properties that previously might have seemed not accessible. Notable examples include the cataclysmic events and exotic objects in galaxies, the equation of state and color superconducting vortex alignment in neutron stars [1], and cosmological dark matter distribution and how they couple to ordinary matter and electroweak forces [2–4]. It provides a search for new physics beyond the standard model of elementary particles. Among the most exciting is the search for the ultra-light scalar dark matter particles, for which direct upper limits more stringent than in the tests of equivalence principle are reported from gravitational wave detectors [5–7]. The recent analyses of models of stochastic gravitational waves show strong enough signals for ultralight dark matter candidates and dark radiations detectable by cosmic microwave background observatories

over a broad frequency range [8].

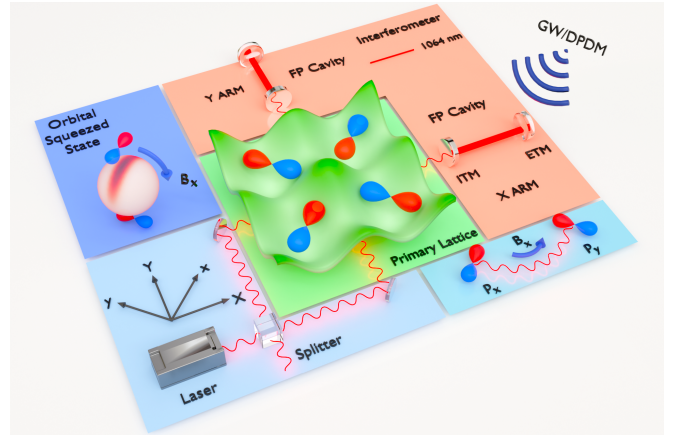


FIG. 1. **Schematic illustration of the orbital atomic sensor.** An orbital squeezed state is prepared by loading atoms into the  $p$ -orbital band of the primary optical lattice (shown in green). The incoming gravitational wave (GWs) or dark photon dark matter (DPDM) modifies the apparent distance between the Input Test Mass (ITM) and End Test Mass (ETM), causing lattice deformation and generating a pseudo-magnetic field ( $B_x$ ) that couples the degenerate  $p_x$  and  $p_y$  orbitals. The resulting orbital rotation can be detected through a time-of-flight experiment that measures the population difference between the two  $p$ -orbitals.

In atomic quantum technology, spin squeezing has emerged as a powerful technique for enhancing the sensitivity of magnetic field detection by suppressing quantum shot noise in the sensing signal—specifically, the spin Larmor precession angle—from the standard quantum limit to the Heisenberg limit [17]. However, due to

\* xiaopeng.li@fudan.edu.cn

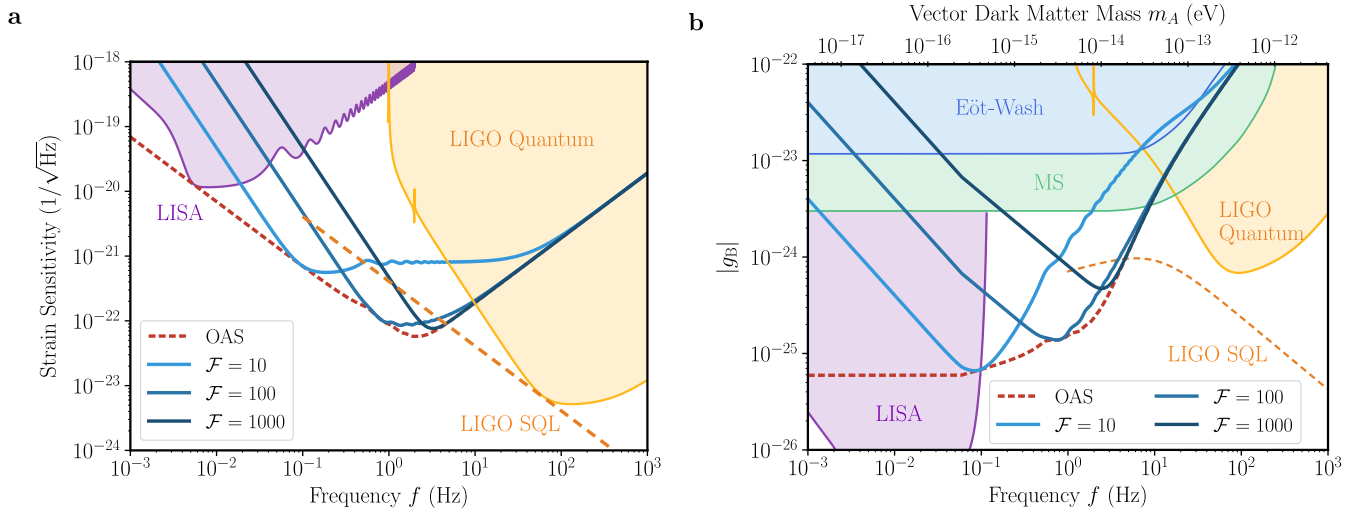


FIG. 2. **Sensitivity curve for detecting GW signals and constraints on DPDM coupling.** **a**, Sky- and polarization-averaged strain sensitivity curves of the orbital atomic sensor, compared with LIGO and LISA detection schemes [9, 10]. The orbital atomic sensor demonstrates advantageous sensitivity in specific frequency ranges for various choices of the finesse  $\mathcal{F}$  of the Fabry-Pérot (FP) cavity. The ‘red-dashed’ line represents the optimal sensitivity of the atomic sensor obtained by varying the cavity finesse. This shows an improvement of 8 dB over the standard quantum limit (SQL) of LIGO at frequencies below a critical value of  $f_c \simeq 1.87$  Hz. **b**,  $1\sigma$  upper limit on the dark photon/baryon coupling  $|g_B|$ , compared with limits from LIGO [6], LISA [10], Eöt-Wash [11, 12], and MICROSCOPE (MS) experiments [13–16]. For constraining  $|g_B|$ , a total observation time of two years is assumed for comparison. The orbital atomic sensor shows an improvement of approximately 17 dB over the MICROSCOPE experiment and 8 dB over the LIGO SQL in detecting dark photons with masses around  $5 \times 10^{-16}$  eV/ $c^2$  and  $4 \times 10^{-15}$  eV/ $c^2$ .

the equivalence principle, atomic spins are fundamentally decoupled from gravitational forces. Meanwhile, the motional degrees of freedom of atoms, which naturally couple to gravitational forces, have been successfully quantized through optical lattice confinement in cold atoms, resulting in discrete energy-separated orbitals [18–20]. Over the past several years, significant progress has been made in the quantum control of  $s$ ,  $p$ , and  $d$  orbitals [21–25]. This has led to the creation of exotic multi-orbital superfluids with vestigial orders [22, 24, 25] and the development of universal quantum orbital gates with fidelities reaching above 95% [21, 23].

Here, we construct an orbital atomic sensor by squeezing the orbital degrees of freedom of a Bose-Einstein condensate in the degenerate  $p_{x,y}$ -bands of an optical lattice (Fig. 1). The two-axis-counter-twisting (TACT) mechanism, which generates squeezing but is famously known challenging to engineer in spin systems [26–28], naturally emerges from the intrinsic interactions of the orbital atomic matter. This sensor is found to exhibit unprecedented precision in detecting orbital state rotation. It is then added to the LIGO interferometer for detecting gravitational waves, forming an atom-LIGO hybrid sensor. This hybrid design enables to obtain noise error suppression not only from the photon squeezing in the standard or future advanced LIGO but also from the additional atomic orbital squeezing. The combined sensitivity is determined by the atomic projection noise and the quantum noise in the photonic modes that couple

to  $p$ -orbital atoms. The former is suppressed by the TACT-induced orbital squeezing; the latter has much weaker strength than the photonic modes probed in the LIGO detector in low frequency regimes. Consequently, the atom-LIGO hybrid sensor exhibits about an order of magnitude improvement in the sensitivity over LIGO’s quantum noise (Fig. 2) while significantly reducing the laser power requirement. It is anticipated that the sensitivity improvement opens novel opportunities for gravitational wave observations.

*Squeezing atomic  $p$ -orbital states to Heisenberg limit*— We consider a large number ( $N$ ) of bosonic atoms loaded into the  $p$ -orbital bands of a bipartite optical lattice, described by a light potential  $V_{\text{lat}}$  with depth  $V_0$  (Fig. 1) [18, 29]. The  $p$ -orbital bands exhibit two inequivalent degenerate minima in quasi-momentum space denoted as  $|p_x\rangle$  ( $\equiv |\uparrow\rangle$ ) and  $|p_y\rangle$  ( $\equiv |\downarrow\rangle$ ) [20]. The two minima form a two-level (pseudo-spin-1/2) system, with its Hilbert space represented by a Bloch sphere (Fig. 1). Under the two-mode approximation, the quantum kinematics of the  $p$ -orbital many-body system is described by pseudo-spin- $N/2$  operators,  $\hat{\mathbf{J}} \equiv (\hat{J}_x, \hat{J}_y, \hat{J}_z)$  with  $\hat{J}_x = (\hat{p}_y^\dagger \hat{p}_x + \text{h.c.})/2$  transforming  $|p_{x,y}\rangle$  states into each other, and  $\hat{J}_z = (\hat{N}_x - \hat{N}_y)/2$  representing the condensed atom number difference between the two  $p$ -orbitals [30–35].

In the experiments, a  $p$ -orbital Bose-Einstein condensate with bosonic atoms condensing into one single min-

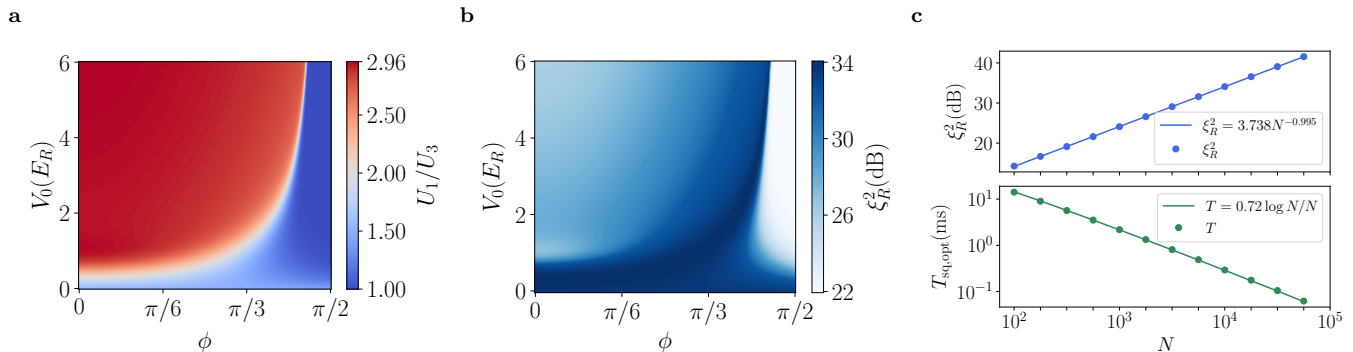


FIG. 3. **Orbital squeezing of the atomic sensor.** **a**, Ratio of interaction parameters  $U_1/U_3$  as a function of the primary lattice depth  $V_0$  and the phase difference  $\phi$  between the standing waves in the X and Y arms (Appendix. A). The interaction parameters in Eq. (1) exhibit significant tunability. The white region at  $U_1/U_3 = 2$  indicates TACT dynamics, while the red and blue regions approaching  $U_1/U_3 \rightarrow 3$  and  $U_1/U_3 \rightarrow 1$  reflect OAT dynamics. **b**, Optimal squeezing parameter  $\xi_R^2$  for  $N = 10^4$  atoms. TACT dynamics achieve an orbital squeezed state with  $\xi_R^2 \sim N^{-1}$ , reaching the Heisenberg limit, while OAT dynamics yield  $\xi_R^2 \sim N^{-2/3}$ . **c**, Scaling behavior of the optimal squeezing time  $T_{\text{sq,opt}}$  and the optimal squeezing parameter  $\xi_{R,\text{opt}}^2$  as a function of atom number  $N$  in the TACT regime. The optical lattice parameters used here are  $V_0 = 6E_R$  and  $\phi = 0.44875\pi$ .

imum has been prepared [18, 22]. Without loss of generality, we assume the state is  $|\Psi_0\rangle$ , with  $\hat{J}_z|\Psi_0\rangle = \frac{N}{2}|\Psi_0\rangle$ . This corresponds to a coherent spin state  $|\theta = 0, \varphi\rangle$  in the pseudo-spin representation, with  $\theta$  and  $\varphi$  the polar and azimuthal angles on the Bloch sphere. When subject to a pseudo-magnetic field  $\Delta\hat{H} = B_x\hat{J}_x$ , the pseudo-spin vector  $\mathbf{J}$  rotates around the  $x$ -axis, accumulating an angle  $\Delta\theta \propto B_x$ . Averaging over  $N$  independent atoms, the resolution for sensing the pseudo-magnetic field constrained by quantum shot noise corresponds to a standard quantum limit  $\Delta\theta_{\text{SQL}} = N^{-1/2}$  [36].

When the atomic interactions are introduced, the dynamics of the  $p$ -orbital system are governed by (Materials and Methods):

$$\hat{H} = (3U_3 - U_1)\hat{J}_x^2 - (U_1 - U_3)\hat{J}_y^2. \quad (1)$$

This interacting Hamiltonian  $\hat{H}$  is a combination of OAT  $\hat{J}_x^2$  (or  $\hat{J}_y^2$ ) and TACT  $\hat{J}_x^2 - \hat{J}_y^2$  interactions. It reduces to the OAT Hamiltonian when  $U_1 = U_3$  or  $U_1 = 3U_3$ , and to the TACT Hamiltonian when  $U_1 = 2U_3$ . In this  $p$ -orbital system, the ratio of  $U_3/U_1$  is largely tunable by adjusting the interfering laser beams forming the optical lattice (Fig. 3). With that the orbital-TACT Hamiltonian naturally emerges, in sharp contrast to spin systems where engineering the TACT Hamiltonian has fundamental challenges owing to the spin  $\text{SU}(2)$  symmetry [26–28].

In quench dynamics, we demonstrate the interaction effects transform the  $p$ -band condensate,  $|\Psi_0\rangle$ , into an orbital-squeezed state with its quantum shot-noise ( $\Delta\theta_{\text{proj}}$ ) suppressed. The extent of this suppression is quantified by the metrological squeezing parameter,  $\xi_R = \Delta\theta_{\text{proj}}/\Delta\theta_{\text{SQL}}$ , which is given by  $\xi_R^2 = N(\Delta J_\varphi)^2/|\langle J_z \rangle|^2$  [26, 37, 38], with  $J_\varphi = \cos\varphi J_x + \sin\varphi J_y$  and the squeezing angle  $\varphi$  defined such that  $(\Delta J_\varphi)^2$  is the

minimum variance perpendicular to the average spin direction. Our simulation results with  $N = 10^4$  (Fig. 3) reveal that optimal squeezing is achieved near the TACT regime. The time required to achieve this optimal squeezing ( $T_{\text{sq,opt}}$ ), is approximately 1 ms under standard experimental conditions [18]. The TACT dynamics produce an orbital squeezed state with  $\xi_R^2 \sim N^{-0.995}$ , indicating quantum enhancement in detecting the pseudo-magnetic field. This enhancement could advance sensitivity from the standard quantum limit to  $N^{-0.998}$ , approaching the Heisenberg limit ( $N^{-1}$ ), a fundamental lower bound set by the non-commutative nature of quantum mechanics [26].

*Atomic quantum sensing of gravitational waves*—When a gravitational wave (GW) passes through a Michelson interferometer, it curves the surrounding spacetime, altering the apparent length of the interferometer arms. This introduces round-trip phase shifts,  $\Delta\Phi_X$ , and  $\Delta\Phi_Y$  in the X and Y arms, respectively. The resulting differential phase  $\Delta\Phi = \Delta\Phi_X - \Delta\Phi_Y$ , the interference pattern of the laser intensity, as measured in LIGO [9]. In contrast, for our orbital atomic sensor, the differential phase  $\Delta\Phi$  causes a real-space deformation of the optical lattice potential. The interaction between GWs and our atomic sensor is described by an effective action (in natural units  $\hbar = c = 1$ ):

$$S = \int d^4x \sqrt{-g} \left[ g^{\mu\nu} \partial_\mu \Psi^\dagger \partial_\nu \Psi - V(\vec{x}, g^{\mu\nu}) |\Psi|^2 \right]. \quad (2)$$

Here  $g^{\mu\nu}$  is the curved spacetime metric,  $\Psi$  is the atomic field, and  $V = m^2/2 + V_{\text{lat}} + U_{\text{lat}}(\Phi_{X,Y})$  is the total potential including the atomic mass terms, the primary lattice potential  $V_{\text{lat}}$  for trapping atoms, and the signal lattice  $U_{\text{lat}}$  carrying the information of GW (Materials and Methods). In this setup, the direct coupling be-

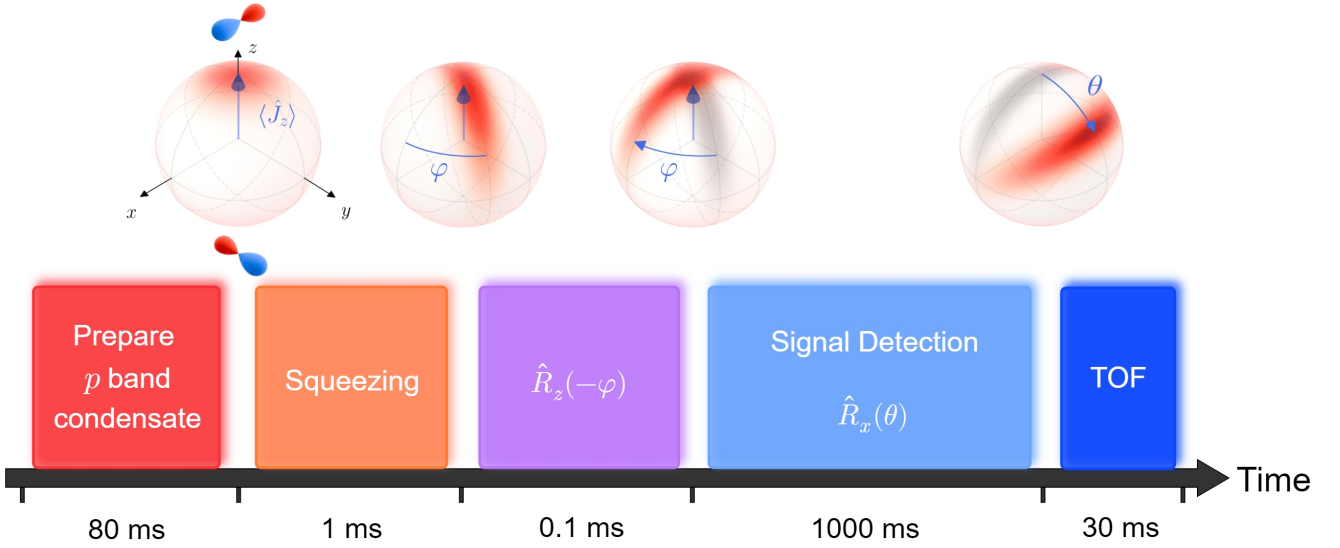


FIG. 4. **Time sequence of high-precision detection with the orbital atomic sensor.** Each measurement cycle consists of five steps: (1) Preparation of bosonic atoms in the condensate state of the  $p$ -orbital band, which takes approximately  $T_{\text{prep}} = 80$  ms [18]; (2) Interaction quench via Feshbach resonance techniques to achieve atom squeezing within  $T_{\text{sq}} = 1$  ms (Appendix C); (3) Adjustment of the optical lattice potential  $V_{\text{lat}}$  to align the most sensitive axis of the uncertainty ellipse along the  $x$ -axis within  $T_{\text{rot}} = 0.1$  ms (Supplementary Information); (4) Detection of the GW/DPDM by evolving the orbital squeezed state under the GW/DPDM-induced pseudo-magnetic field for a duration of  $T_{\text{lifc}} = 1000$  ms, within the cold atom lifetime; (5) Execution of a Time-of-Flight (TOF) experiment to measure the rotation angle  $\theta$  [18]. The total duration of a measurement cycle is  $T = T_{\text{prep}} + T_{\text{sq}} + T_{\text{rot}} + T_{\text{lifc}} + T_{\text{TOF}}$ .

tween GWs and cold atoms via the spacetime metric is about ten orders of magnitude smaller than the indirect coupling mediated by the deformation of lattice potential (Supplementary Materials). The GW-induced lattice deformation  $U_{\text{lat}}(\Phi_{X,Y})$  acts on the  $p$ -orbital atoms as a pseudo-magnetic field, and can be sensitively detected using orbital squeezed states (Fig. 1). The strength of the pseudo-magnetic field is  $B_x = \eta U_0 \Delta\Phi$ , where  $\eta \in (0, 1)$  is a dimensionless efficiency factor dependent on the characterization of the primary lattice  $V_{\text{lat}}$  (Materials and Methods). The depth  $U_0$  of the signal lattice  $U_{\text{lat}}$  is proportional to the laser power used to generate it, typically on the order of mW, which is several orders of magnitude smaller than the light power used by the standard LIGO.

The effective quantum Hamiltonian description for the  $p$ -orbital atoms interacting with GW-induced lattice distortion is:

$$\hat{H} = \hat{B}_x \hat{J}_x, \quad (3)$$

where  $\hat{B}_x$  further incorporates quantum fluctuations of light besides its averaging effect, namely the pseudo-magnetic field  $B_x$  (Materials and Methods). In this protocol, the orbital polarization  $\langle J_y \rangle$  is measured after a certain duration ( $T$ ) of evolution under this Hamiltonian, starting from the prepared orbital squeezed state (Fig. 4). The orbital rotation angle induced by light is  $\hat{\theta} = \int_0^T dt y(t) \hat{B}_x(t) / \hbar$  with  $y(t)$  a window function associated with the applied pulse sequences (Materials and

Methods). The measurement precision of  $\hat{J}_y$  is limited by noises from both atoms and photons as:

$$\langle J_y^2 \rangle = |\langle J_z \rangle|^2 ((\Delta\theta)_{\text{proj}}^2 + (\Delta\theta)_{\text{photon}}^2), \quad (4)$$

where  $(\Delta\theta)_{\text{proj}}^2 = \xi_R^2 / N$  accounts for the orbital projection noise in the initial atomic state, and  $(\Delta\theta)_{\text{photon}}^2 = \langle \hat{\theta}^2 \rangle$  represents the photonic quantum noise from the dark port input state (Materials and Methods).

The resulting strain sensitivity  $S_n = S_{\text{atom}} + S_{\text{photon}}$  for typical experimental parameters is presented in Fig. 2a. The orbital atomic sensor develops an optimal sensitivity around 1 Hz. Its performance is mainly limited by photon fluctuations at low frequencies, whereas at higher frequencies, it is constrained by both of increasing atomic projection noise and photon fluctuations. The sensitivity for frequency  $f$  below a critical frequency  $f_c \simeq 1.87$  Hz takes a form of,

$$S_{\text{OAS}}(f) = S_{\text{SQL}}(f) C_{\text{atom}}(f, T) \frac{(\Delta\theta)_{\text{proj}}}{\eta \sqrt{U_0 T}}. \quad (5)$$

Here,  $C_{\text{atom}}(f, T)$  is a coefficient dependent solely on the detecting protocol details (Supplementary Materials), and  $S_{\text{SQL}}(f) = 8\hbar / ML(2\pi f)^2$  represents the SQL of a conventional interferometric GW detector with test mass  $M$  and arm length  $L$ . It is evident that for  $f < f_c$ , the sensitivity of the atomic sensor exhibits the same scaling with respect to  $M$  and  $L$  according to the SQL



of a conventional detector. It nevertheless surpasses the limit by enhancing the phase precision of the atom or increasing the depth of the signal lattice, ensuring that  $C_{\text{atom}}(f, T)(\Delta\theta)_{\text{proj}}/\eta\sqrt{U_0 T} < 1$ . Without orbital squeezing, the atomic sensor behaves worse than the SQL of a conventional sensor (Supplementary Materials). For  $f > f_c$ , the sensitivity scales worse than a conventional detector due to the limited amount of atomic integration time (Supplementary Materials).

*Ultralight dark matter detection*—As interferometric gravitational-wave detectors are sensitive to ultralight dark matter [6, 39–41], our atomic sensor can be used to probe them as well. The ultralight dark photon dark matter  $A^\mu$  is expected to couple to normal matter current  $J_D^\mu$ , with  $D = B$  the baryon number. The Lagrangian describes this coupling is given by (in natural units  $\hbar = c = \epsilon_0 = 1$ ):

$$\mathcal{L} = -\frac{1}{4}F^{\mu\nu}F_{\mu\nu} + \frac{1}{2}m_A^2 A^\mu A_\mu - eg_D J_D^\mu A_\mu, \quad (6)$$

with  $F_{\mu\nu} = \partial_\mu A_\nu - \partial_\nu A_\mu$  the field strength tensor of dark photon,  $m_A$  the dark photon mass, and  $g_D$  the coupling constant normalized to the electromagnetic coupling  $e$ . This coupling also causes oscillations of the apparent length of the arms, altering the differential phase  $\Delta\Phi$ , which can be detected by our atomic sensors. The upper limit on  $g_D$  can therefore be calculated from the GW strain sensitivity, which is shown in Fig. 2b. Our sensor predicts 17 dB of magnitude decrease in the detectable upper limits of the  $U(1)_D$  coupling near  $m_A \sim 5 \times 10^{-16} \text{eV}/c^2$ , surpassing the current best constraints achieved by the MICROSCOPE experiment [13–16].

*Discussion*—We have developed an orbital atom-LIGO hybrid quantum sensor for the detection of gravitational waves and ultralight dark matter by precisely measuring the position of test masses. Our sensor operates with a remarkable reduction in laser power, using only  $10^{-5}$  of that required by LIGO, and has achieved an 8 dB improvement in sensitivity for low-frequency gravitational wave detection over the standard LIGO configuration. That corresponds to the increase of about three orders of magnitude in detection volume [42]. The sensor also tightens constraints on the  $U(1)_D$  dark gauge coupling in the sought-after ultralight mass range of  $10^{-17}$  to  $10^{-13} \text{eV}/c^2$ .

One key ingredient for the enhancement in the sensitivity is due to the orbital squeezing of the sensing atoms. Unlike spin squeezing, which is challenging to engineer due to the fundamental  $SU(2)$  symmetry, orbital squeezing naturally emerges when atoms are loaded into the symmetric (degenerate)  $p_{x,y}$  bands of an optical lattice. Besides detecting gravitational waves, the orbital atomic quantum sensor could also contribute to advancing other interferometry-based quantum technologies such as optical gyroscopes in inertia navigation and Fourier-transform spectroscopy in chemical analysis, for its outstanding sensitivity in measuring the phase accu-

mulation of the interferometer.

In our orbital atomic sensor, the photons traveling in the Michelson interferometer that acquire the gravitational wave signal interact quantum mechanically with the sensing atoms, which tends to slightly degrade the orbital squeezing and thus the detection sensitivity. Sensitivity improvements are expected through the application of advanced quantum control techniques. Additionally, the laser power used in the orbital atomic sensor is significantly lower than in LIGO, to preserve the stability of the cold atom sample. In principle, utilizing multiple ( $M$ ) cold atom samples sharing a light signal with a laser power comparable to that of LIGO could further enhance sensitivity by a factor of  $1/\sqrt{M}$ . At the same time, this sensitivity enhancement could be compromised by the technical noise of introducing multiple beam splitters, as unavoidable in parallelizing the orbital atomic sensors. These avenues warrant further investigation.

*Acknowledgments*—The authors wish to acknowledge helpful discussions with Rainer Blatt, Peter Zoller, Dan Stamper-Kurn, Bo Yan, Gordon Baym, Daniel Vanmaekelbergh and Cristiane Morais Smith. This work is supported by National Key Research and Development Program of China (Grant No. 2021YFA1400900), Innovation Program for Quantum Science and Technology of China (Grant No. 2024ZD0300100), National Natural Science Foundation of China (Grant No. 11934002), and Shanghai Municipal Science and Technology (Grant No. 2019SHZDZX01, 24DP2600100) (X.Y., X.L.), and by AFOSR Grant No. FA9550-23-1-0598, MURI-ARO Grant No. W911NF-17-1-0323 through UC Santa Barbara (W.V.L.). W.V.L. would like to express gratitude for the visit fellowship at the IQOQI Innsbruck, Austrian Academy of Sciences, where this manuscript was completed.

## Appendix A. $P$ -orbital bands in a bipartite square lattice

The primary trapping potential  $V_{\text{lat}}$  is created by counter-propagating laser beams with a wavelength of  $\lambda = 532\text{nm}$  along the  $X, Y$  directions (a detailed optical layout is provided in the Supplementary Materials). The potential is given by [18, 29]:

$$V_{\text{lat}}(\mathbf{r}) = -\frac{V_0}{4} |e^{i\mathbf{KX}} + e^{-i\mathbf{KX}} + e^{i\phi} (e^{i\mathbf{KY}} + e^{-i\mathbf{KY}})|^2.$$

Here,  $\mathbf{K} = 2\pi/\lambda$  is the wave-vector of the laser, and  $\phi$  denotes the phase difference between the two standing waves in the  $X, Y$  directions. Rotating the coordinate system by  $\pi/4$ , we reach the new axes  $x = (X + Y)/\sqrt{2}$  and  $y = (Y - X)/\sqrt{2}$  with lattice vectors  $\mathbf{a}_1 = a(1, 0)$  and  $\mathbf{a}_2 = a(0, 1)$ , where  $a = \lambda/\sqrt{2}$ . The  $D_4$  point group symmetry of  $V_{\text{lat}}$  yields two degenerate ground states,  $|p_{x,y}\rangle$ , in the  $p$ -bands of  $V_{\text{lat}}$ . These states are at time-reversal invariant quasi-momentum  $\mathbf{Q}_x = (\pi, 0)/a$  and  $\mathbf{Q}_y = (0, \pi)/a$ , respectively ( $k = 2\pi/a$  is the reciprocal

lattice constant). Although  $V_{\text{lat}}$  undergoes real-space deformation in the presence of GW/DPDM signals, it does not induce transitions between the  $p_{x,y}$  states due to lattice translation symmetry.

## Appendix B. Emergence of the orbital squeezing Hamiltonian

The two-mode approximation for  $p$ -orbital bosons is represented by the field operator:

$$\hat{\Psi}(\mathbf{r}) = \psi_x(\mathbf{r})\hat{p}_x + \psi_y(\mathbf{r})\hat{p}_y,$$

where  $\psi_\alpha(\mathbf{r})$  are the Bloch wavefunctions and  $\hat{p}_\alpha$  are the annihilation operators for each mode, satisfying  $[\hat{p}_\alpha, \hat{p}_\beta^\dagger] = \delta_{\alpha\beta}$  with  $\alpha, \beta = x, y$ . The contact atomic interaction can be formulated as  $\hat{H} = U_1(\hat{n}_x^2 + \hat{n}_y^2)/2 + 2U_2\hat{n}_x\hat{n}_y + U_3(\hat{p}_x^\dagger\hat{p}_x^\dagger\hat{p}_y\hat{p}_y + \text{h.c.})/2$  under the two-mode approximation. Here,  $\hat{n}_\alpha = \hat{p}_\alpha^\dagger\hat{p}_\alpha$  represents the number operator for the  $p_\alpha$  mode, and the total  $p$ -orbital number operator is  $\hat{N} = \hat{n}_x + \hat{n}_y$ . The interaction parameters  $U_{1,2,3}$  are derived from integrals over the Bloch functions [20]. Due to the time-reversal symmetry of the  $p$ -orbital modes,  $U_2$  equals to  $U_3$  (Supplementary Materials). Employing the Schwinger representation of angular momentum  $\hat{J}_i = 1/2 \sum_{\alpha\beta} \hat{p}_\alpha^\dagger \sigma_{\alpha\beta}^i \hat{p}_\beta$ ,  $i = x, y, z$  with  $\sigma^i$  the Pauli operators, yields the form of spin squeezing Hamiltonian Eq. (1) in the main text.

## Appendix C. Interaction control

The preparation of cold atomic  $p$ -orbital squeezing begins with a weakly interacting BEC in the excited band of a bipartite optical lattice [18, 22, 24]. Squeezing in the  $p$ -orbital is achieved by an interaction quench, where the interaction strength is abruptly increased. This is accessible to the current cold atom technology using Feshbach resonances. For instance, in  $^7\text{Li}$  atoms, a broad Feshbach resonance is present at approximately 737 G [43, 44]. The initial  $p$ -orbital BEC is formed with the weakly interacting state  $|F = 1, m_F = -1\rangle$ . The interaction quench is realized by driving a Raman transition that converts the atomic internal state to  $|F = 1, m_F = 1\rangle$ , which exhibits strongly repulsive interactions.

## Appendix D. Pseudo-magnetic field induced by GW or dark matter

The signal lattice  $U_{\text{lat}}$  used to detect GW/DPDM signal is generated by a laser with doubled wavelength  $2\lambda = 1064\text{nm}$ . This lattice is further coupled to the FP cavities at the end of Michelson interferometer arms to enhance

detecting sensitivity.  $U_{\text{lat}}$  has the expression:

$$-U_0 \left\{ 1 + \cos\left(\frac{kx}{2} + \Phi_x\right) \cos\left(\frac{ky}{2} + \Phi_y\right) + \cos\phi_U \left[ \cos\left(\frac{kx}{2} + \Phi_x\right) + \cos\left(\frac{ky}{2} + \Phi_y\right) \right] \right\}.$$

Here,  $U_0$  is its depth and must satisfy  $U_0 \ll V_0 = O(E_R)$  to ensure the validity of the two-mode approximation, the phase  $(\Phi_x, \Phi_y) = (\Phi_X + \Phi_Y, \Phi_Y - \Phi_X)/2$  where  $\Phi_{X,Y}$  are the phase accumulation of the  $2\lambda$ -laser in the X, Y arms with FP cavities, and  $\phi_U$  denotes the phase difference between the standing waves in the two arms. The direct coupling of bosons to GW/DPDM induces an energy shift in the  $p$ -orbital states in principle, but with a negligible strength (Supplementary Materials). In contrast, the GW/DPDM induced differential phase  $\Delta\Phi = \Delta\Phi_X - \Delta\Phi_Y$  produces a significant shift to the the signal lattice, leading to the Hamiltonian  $\hat{H}^U = \sum_{\alpha\beta} J_{\alpha\beta}^U \hat{p}_\alpha^\dagger \hat{p}_\beta$  with  $J_{\alpha\beta}^U = \int d^2\mathbf{r} \psi_\alpha^*(\mathbf{r}) U_{\text{lat}}(\mathbf{r}) \psi_\beta(\mathbf{r})$ . The pseudo-magnetic field is derived as:

$$B_x = 2J_{xy}^U = \eta(V_0, \phi) U_0 \Delta\Phi, \quad (\text{D1})$$

where  $\eta = \int d^2\mathbf{r} \psi_x^*(\mathbf{r}) \sin(kx/2) \sin(ky/2) \psi_y(\mathbf{r})$  is the efficiency factor.

## Appendix E. Detecting protocol

For a low frequency GW/DPDM signal satisfying  $fT_{\text{life}} < 1/2$ , no additional pulses are applied in the signal detection step in Fig. 4. Consequently, the window function defined in the main text, simplifies to  $y(t) \equiv 1$ . Conversely, for high-frequency signals, periodic dynamical decoupling (PDD) sequences are employed, which consist of  $\hat{R}_z(\pi)$  pulses applied every  $1/(2f)$  time interval. This method prevents the cancellation of the accumulated phase  $\theta$  that occurs in different half periods of the signal cycle, and  $y(t)$  changes its sign with each application of a  $\pi$ -pulse. The  $\pi$ -pulse demands time  $t_p \simeq 100\mu\text{s}$  and is implemented by slightly breaking the degeneracy of  $p_{x,y}$  modes (Supplementary Materials).

## Appendix F. Noise channel analysis

The measurement sensitivity of our protocol (Fig.4) is defined as:

$$S = \frac{\sqrt{\langle J_y^2 \rangle}}{|\partial_h \langle J_y \rangle|} \sqrt{T}. \quad (\text{F1})$$

As shown in Eq. (4), the noise in the numerator encompasses both atomic projection noise and photonic quantum noise. For detecting a monochromatic gravitational wave of frequency  $f$ , the sensitivity is expressed as (Sup-

plementary Materials):

$$S = S_{\text{atom}} + S_{\text{photon}}. \quad (\text{F2})$$

The atomic noise contribution reads:

$$S_{\text{atom}}(f) = \left( \frac{\hbar}{\eta U_0 \sqrt{T}} \frac{(\Delta\theta)_{\text{proj}}}{Y(f)KL} \right)^2 \frac{1 + (f/f_p)^2}{(2\mathcal{F}/\pi)^2}. \quad (\text{F3})$$

where  $(\Delta\theta)_{\text{proj}}^2 = \xi_R^2/N$ ,  $Y(f)$  is the Fourier transform of  $y(t)$ , and  $\mathcal{F}$  and  $f_p = c/(4FL)$  are the finesse and pole frequency of FP cavity, respectively. Our setup mitigates atomic noise by employing an orbital squeezed state to minimize  $(\Delta\theta)_{\text{proj}}$ . The photonic noise mainly involves shot noise  $S_{\text{shot}}$  and radiation pressure noise  $S_{\text{rad}}$ , associated with the phase and amplitude fluctuations of the dark port input electrical field, as follows:

$$S_{\text{photon}}(f) = S_{\text{shot}} + S_{\text{rad}} = S_{\text{SQL}} \frac{4 \sin^2 \beta + \mathcal{K}^2}{2\mathcal{K}}, \quad (\text{F4})$$

with  $S_{\text{SQL}}(f) = 8\hbar/ML(2\pi f)^2$  being the SQL of the standard LIGO detector,  $\beta = \arctan(f/f_p)$  the phase shift induced by the FP cavity, and  $\mathcal{K}$  the optomechanical coupling strength. In our setup, the shot noise is significantly reduced due to the partial cancellation of phase fluctuations of counter-propagating laser beams experienced by the atoms. The radiation pressure noise is also suppressed because the signal laser power is reduced to  $10^{-5}$  of the LIGO interferometer.

We would like to remark that the sensitivity of our atom orbital sensor in detecting gravitational waves can be further enhanced by considering injection of photonic squeezed states at the dark port input as in the advanced LIGO, for the photonic noise in Eq. (F2) will be further suppressed for squeezed light [45–48].

### Appendix G. Strain sensitivity and detection threshold of $g_B$

For the construction of Fig. 2, the atomic sensor is designed with  $N = 8 \times 10^5$   $^7\text{Li}$  atoms trapped in the primary lattice with depth of  $V_0 = 6E_R$  ( $E_R$  is the photon recoil energy  $\hbar^2/2m\lambda^2$  with  $m$  the mass of atoms). The primary lattice is generated by a laser with a power of 1.7 W in each arm, operating with an efficiency of  $\eta = 0.6$ . The signal lattice has a depth of  $U_0 = 0.1E_R$ , with a laser power of 32 mW per arm, which is only about  $10^{-5}$  of the LIGO's laser power 5.2 kW. The test masses are of 40kg, and the arm length is  $L = 4\text{km}$ , aligning with the specifications of LIGO. The measurement pulse sequence is optimized for each frequency to ensure maximum sensitivity, which can be realized by quantum lock-in techniques [49–51]. The dark port input state is assumed to be the vacuum state for a fair comparison with the SQL of LIGO. The resulting curves, depicted in Fig. 2a for GWs and Fig. 2b for DPDMS, represent averages over polarizations and propagation directions of the respec-

tive signals (Supplementary Materials).

# Supplementary Information for “Squeezing atomic $p$ -orbital condensates for detecting gravitational waves”

Xinyang Yu, W. Vincent Liu, Xiaopeng Li

## Contents

S-1. Multi-orbital BEC in Bipartite Square Lattice	10
A. Optical Lattice Setup	10
B. Band Structure	12
C. Two-Mode Approximation	14
S-2. Orbital Squeezing of $p$ -orbital Bosons	15
A. Schwinger Representation of Angular Momentum	16
B. Squeezing $p$ -orbital Bosons to Heisenberg Limit	17
C. Rotation about $z$ -axis	20
S-3. Detecting Gravitational Waves	21
A. Theory	21
B. Lattice-deformation-mediated Interaction between GW and Bosons	26
C. Direct Interaction between GW and Bosons	28
D. Interaction between GW and the Optical Lattice $V_{\text{lat}}$	31
E. Detecting Protocol	32
S-4. Noise Budgets of the Orbital Atomic Sensor	34
A. Quantum Optical Description of the Atomic Sensor	35



	9
1. Quantized Electric Fields and Its Interfering Lattice	35
2. Interaction between Atoms and Quantized Light	40
3. Measurement Uncertainty	41
B. Calculation of the Full Strain Sensitivity Curve	45
C. Influence of Atomic Species on Sensitivity	48
D. Sky- and Polarization-averaging	51
S-5. Detecting Dark Photon Dark Matter	53
A. Dark Photon Electrodynamics	53
B. Coupling between DPDM and the Atomic Sensor	55
1. Coupling between DPDM and Atoms	56
2. Coupling between DPDM and Test Masses	56
C. $1\sigma$ Upper Limits of $g_D$	58
S-6. Parameters of the Orbital Atomic Sensor	59
References	61

## S-1 Multi-orbital BEC in Bipartite Square Lattice

Controlling Bose-Einstein condensates (BEC) of cold atoms in the  $p$ -orbital bands of optical lattices, a key new element in our atom-LIGO hybrid sensor, draws on nearly two decades of experiences in theoretical and experimental studies in the field [19, 20, 29], where high fidelity control techniques have been fully established. Multi-orbital BEC have been successfully realized in the experiments in various geometries from quasi 1D lattice [52, 53] to quasi-two dimensional checkerboard [18, 54, 55] and hexagonal lattices [22, 24] after the early theoretical proposals [56–58]. The experimental methods employed in this work are directly adapted from the Hamburg checkerboard optical lattice [18, 29]. In other words, the multi-orbital BEC employed in the orbital atom-LIGO quantum sensor is naturally feasible to current experimental setups with minimum modification required.

In the following, we briefly review the basics about the experimentally realized  $p$ -BEC states in bipartite square lattice, following the setup of [18, 29]. As depicted in Fig. S1, the experimental configuration of a square optical lattice bears a resemblance to gravitational interferometers like LIGO, with both systems operating on the principles of Michelson Interferometers (MI). The experimental setup of our orbital atomic sensor is shown in Fig. 1 in the main text and Fig. S1.

### A Optical Lattice Setup

The primary lattice potential  $V_{\text{lat}}$ , used for trapping  $p$ -orbital bosons, is generated by superimposing counter-propagating laser beams with a wavelength of  $\lambda = 532\text{nm}$  along

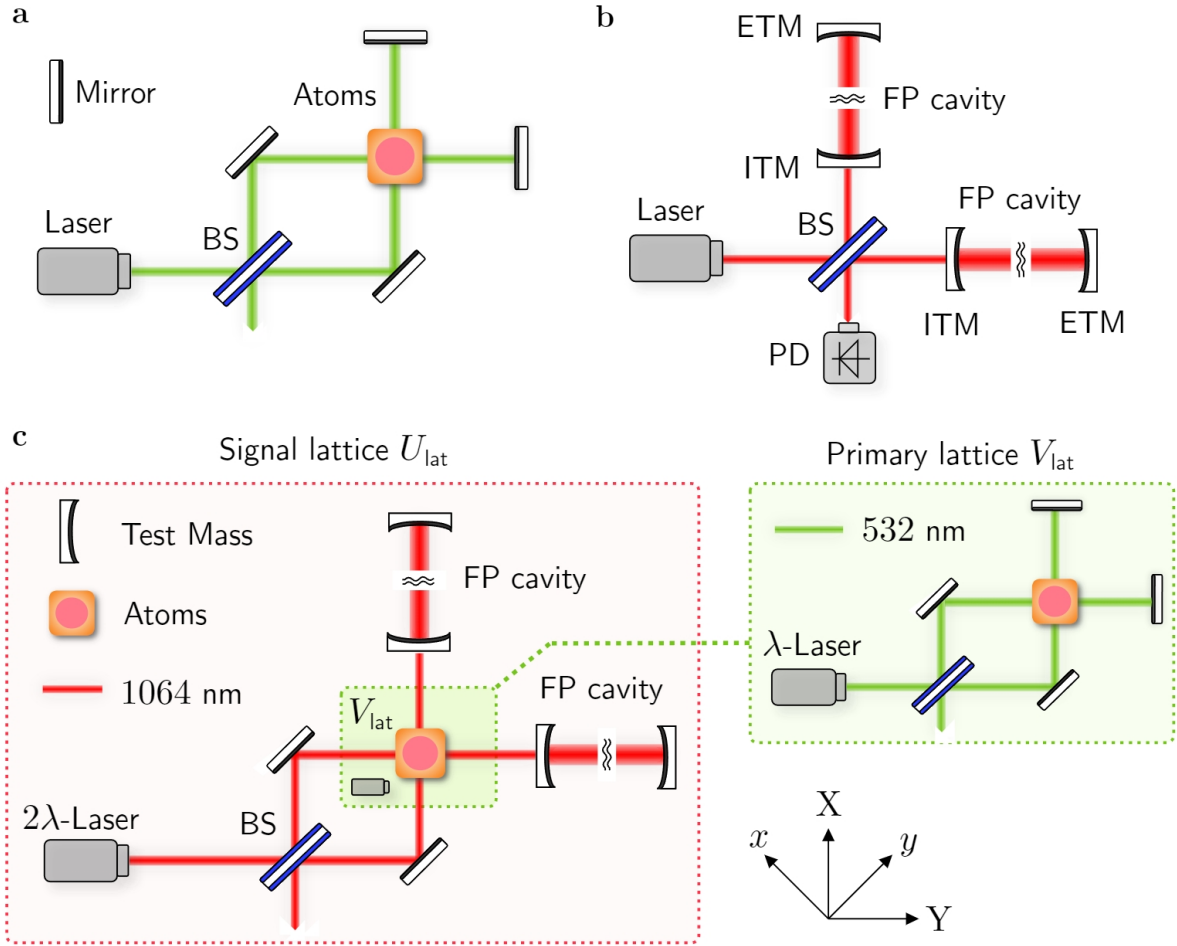


FIG. S1. Illustration of  $p$ -orbital BEC experiments [18], the LIGO observatory [59] and the orbital atomic sensor. **a**, Sketch of the optical lattice setup where two optical standing waves are superimposed. **b**, The LIGO observatory features two additional Fabry-Perot cavities (FP cavities) in each arm, which serve to increase the effective arm length. **c**, The orbital atomic sensor represents a synthesis of these two interferometric systems. The primary lattice  $V_{\text{lat}}$  confining the atoms is generated by the  $\lambda$ -laser (532 nm), while the signal lattice  $U_{\text{lat}}$  for signal detection is generated by  $2\lambda$ -laser (1064 nm). The acronyms used are BS = beam splitter, ITM = input test mass, ETM = end test mass, PD = photon detector.

the X, Y directions, as depicted in Fig. S1. The potential is expressed as:

$$V_{\text{lat}}(\mathbf{r}) = -\frac{V_0}{4} \left| \left[ (\mathbf{e}_z \cos \alpha + \mathbf{e}_Y \sin \alpha) e^{iKX} + r \mathbf{e}_z e^{-iKX} \right] + t e^{i\phi} \mathbf{e}_z (e^{iKY} + r e^{-iKY}) \right|^2, \quad (\text{S1})$$

where  $K = 2\pi/\lambda$  is the wave-vector of the laser with wavelength  $\lambda$  (to be referred to as  $\lambda$ -laser in the following),  $t < 1$  and  $r < 1$  account for imperfect optical transmission and reflection efficiencies,  $\alpha$  is used to adjust the anisotropy between  $p_{x,y}$  orbitals by rotating the polarizations of the light. When  $r = t = \cos \alpha = 1$ , we return to the case of perfect optics and the optical lattice has an exact  $D_4$  point group symmetry:

$$V_{\text{lat}}(X, Y) = -V_0 [\cos^2 KX + \cos^2 KY + 2 \cos \phi \cos KX \cos KY] . \quad (\text{S2})$$

In terms of the rotated coordinate  $x = \frac{1}{\sqrt{2}}(X + Y)$  and  $y = \frac{1}{\sqrt{2}}(Y - X)$ , Eq. (S2) takes the form of:

$$V_{\text{lat}}(x, y) = -V_0 [1 + \cos kx \cos ky + \cos \phi(\cos kx + \cos ky)] , \quad (\text{S3})$$

where  $k = \sqrt{2}K$  is the magnitude of reciprocal lattice vectors. (The photon recoil energy is still defined as  $E_R = \hbar^2 K^2/2m$  instead of  $\hbar^2 k^2/2m$ , where  $m$  is the atomic mass.) The lattice vectors of  $V_{\text{lat}}$  in  $(x, y)$  coordinate are  $\mathbf{a}_1 = a(1, 0)$  and  $\mathbf{a}_2 = a(0, 1)$  with  $a = 2\pi/k$  (Fig. S2). Its two local minimum are  $V_A = -2V_0(1 + \cos \phi)$  at  $\mathbf{r}_A = (0, 0)$  and  $V_B = -2V_0(1 - \cos \phi)$  at  $\mathbf{r}_B = (a/2, a/2)$ . In the following, we refer to  $V_{\text{lat}}$  as the primary optical lattice, while an signal lattice  $U_{\text{lat}}$  is employed for detecting signals of gravitational waves or ultralight dark matter (see Sec. S-3).

## B Band Structure

The band structure of  $V_{\text{lat}}$  is obtained by diagonalizing the non-interacting Hamiltonian  $\hat{H}_0$ :

$$\hat{H}_0 = \int d^3\mathbf{r} \hat{\Psi}_{3d}^\dagger(\mathbf{r}) \left( -\frac{\hbar^2}{2M} \nabla^2 + V_{\text{lat}}(\mathbf{r}) \right) \hat{\Psi}_{3d}(\mathbf{r}) , \quad (\text{S4})$$

where  $\hat{\Psi}_{3d}(\mathbf{r}) = \hat{\Psi}(\mathbf{r})\phi_0(z)$  is the bosonic field operators, and  $\phi_0(z)$  is the ground state

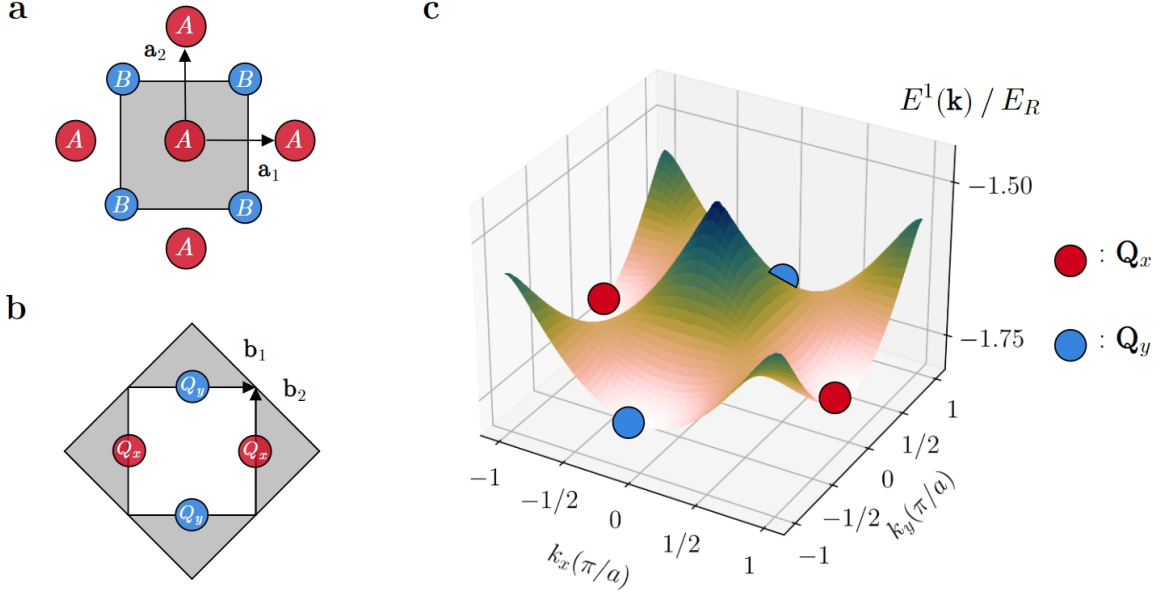


FIG. S2. **a**, Real-space configuration of the lattice potential  $V_{\text{lat}}$  in the  $x, y$  coordinate, with local minima at  $A(0, 0)$  and  $B(a/2, a/2)$ . **b**, The first Brillouin Zone of  $V_{\text{lat}}$ .  $\mathbf{Q}_{x,y}$  represent the two degenerate band minima in the first excited band. **c**, The first excited band spectrum  $E^1(\mathbf{k})$  obtained by numerically diagonalizing the Hamiltonian in Eq. (S4). The parameters are set as  $V_0 = 2E_R$  and  $\phi = 0.4\pi$ .

of the harmonic oscillator with circular frequency  $\omega_z$  along the  $z$  direction.  $\hat{\Psi}(\mathbf{r})$  has an expansion in the Bloch states basis as:

$$\hat{\Psi}(\mathbf{r}) = \sum_{\mathbf{k} \in \text{1BZ}} \sum_n \psi_{n,\mathbf{k}}(\mathbf{r}) \hat{b}_n(\mathbf{k}). \quad (\text{S5})$$

The dispersion relation of the first excited band is shown in Fig. S2. There are two degenerate ground states with time-reversal (TR) invariant quasi-momentum  $\mathbf{Q}_x = (\pi, 0)/a$  and  $\mathbf{Q}_y = (0, \pi)/a$  [20]. The so-called  $p$ -BEC states are the condensate of these two states.

The ground state manifold of  $N$  non-interacting  $p$ -orbital bosons are spanned by:

$$|N_x, N_y\rangle = \frac{[\hat{b}_x^\dagger(\mathbf{Q}_x)]^{N_x} [\hat{b}_y^\dagger(\mathbf{Q}_y)]^{N_y}}{\sqrt{N_x! N_y!}} |0\rangle \text{ with } N_x + N_y = N. \quad (\text{S6})$$

In experiments, we are able to prepare normal  $p$ -BEC states  $|p_x\rangle^{\otimes N} = |N, 0\rangle$  and



$|p_y\rangle^{\otimes N} = |0, N\rangle$  as well as chirality-breaking  $p_{\pm}$  states  $(|p_x\rangle \pm i|p_y\rangle)^{\otimes N}$  [18, 29] by tuning the interaction strength between atoms through Feshbach resonance techniques.

## C Two-Mode Approximation

Inspired by previous studies on interference of fragmented BEC of two internal states [30, 31] and in double wells [32, 33], we propose the two-mode approximation [34, 35] of  $p$ -orbital bosons describing the evolution of bosons from the initial  $p$ -BEC state as:

$$\hat{\Psi}(\mathbf{r}) = \psi_x(\mathbf{r})\hat{p}_x + \psi_y(\mathbf{r})\hat{p}_y, \quad (\text{S7})$$

where we have used the notation  $\psi_{\alpha}(\mathbf{r}) := \psi_{p_{\alpha}, \mathbf{Q}_{\alpha}}(\mathbf{r})$  as the single particle wavefunctions and  $\hat{p}_{\alpha} := \hat{b}_{p_{\alpha}}(\mathbf{Q}_{\alpha})$  Eq. (S5) as the annihilation operators of the corresponding modes, satisfying  $[\hat{p}_{\alpha}, \hat{p}_{\beta}^{\dagger}] = \delta_{\alpha, \beta}$  with  $\alpha, \beta = x, y$ .

In the two-mode approximation, the single-body Hamiltonian is given by:

$$\hat{H}_0 = \epsilon(\hat{n}_x + \hat{n}_y), \quad (\text{S8})$$

with  $\epsilon = E^1(\mathbf{Q}_{x,y})$  (Fig. S2) and  $\hat{n}_{\alpha}$  the number operator of its corresponding mode.

And the contact interaction  $V_{\text{int}}(\mathbf{r} - \mathbf{r}') = g_{3d}\delta(\mathbf{r} - \mathbf{r}')$  between bosons is described by:

$$\hat{H}_{\text{int}} = \frac{g_{3d}}{2} \int d^3\mathbf{r} \hat{\Psi}_{3d}^{\dagger}(\mathbf{r}) \hat{\Psi}_{3d}^{\dagger}(\mathbf{r}) \hat{\Psi}_{3d}(\mathbf{r}) \hat{\Psi}_{3d}(\mathbf{r}) = \sum_{\alpha_1 \sim 4 = x, y} U_{\alpha_1 \alpha_2 \alpha_3 \alpha_4} \hat{p}_{\alpha_1}^{\dagger} \hat{p}_{\alpha_2}^{\dagger} \hat{p}_{\alpha_3} \hat{p}_{\alpha_4}, \quad (\text{S9})$$

where  $g_{3d}$  is given by the 3d scattering length  $a_{3d}$  as  $g_{3d} = 4\pi\hbar^2 a_{3d}/M$ . The interaction coefficients  $U_{\alpha_1 \alpha_2 \alpha_3 \alpha_4}$  are given by:

$$U_{\alpha_1 \alpha_2 \alpha_3 \alpha_4} = \frac{g_{2d}}{2} \int d^2\mathbf{r} \psi_{\alpha_1}^*(\mathbf{r}) \psi_{\alpha_2}^*(\mathbf{r}) \psi_{\alpha_3}(\mathbf{r}) \psi_{\alpha_4}(\mathbf{r}), \quad (\text{S10})$$

with  $g_{2d} = g_{3d} \int |\phi_0(z)|^4 dz$ . The  $D_4$  lattice symmetry restricts that the only non-vanishing

(up to permutation of indices) coefficients are:

$$U_1 = U_{xxxx} = U_{yyyy} = \frac{g_{2d}}{2} \int d^2\mathbf{r} |\psi_x(\mathbf{r})|^4, \quad (\text{S11})$$

$$U_2 = U_{xyyx} = \frac{g_{2d}}{2} \int d^2\mathbf{r} |\psi_x(\mathbf{r})|^2 |\psi_y(\mathbf{r})|^2, \quad (\text{S12})$$

$$U_3 = U_{xxyy} = U_{yyxx}^* = \frac{g_{2d}}{2} \int d^2\mathbf{r} (\psi_x^*(\mathbf{r}))^2 (\psi_y(\mathbf{r}))^2. \quad (\text{S13})$$

In the harmonic limit  $V_0/E_R \gg 1$ ,  $U_1 = 3U_2 = 3U_3$ , while in a general case the ratio  $U_1/U_3$  varies with the parameters  $(V_0, \phi)$ , see Fig. 3a in main text. It is worth noting that  $U_2 \equiv U_3$  exactly for our checkerboard lattice because that  $\psi_{x,y}(\mathbf{r})$  are TR-invariant and thus real-valued. Furthermore,  $U_1 \geq U_2$  because  $U_1 - U_2 \propto \int d^2\mathbf{r} (|\psi_x(\mathbf{r})|^2 - |\psi_y(\mathbf{r})|^2)^2 \geq 0$ .

The interacting Hamiltonian only has three terms now:

$$\hat{H}_{\text{int}} = \frac{U_1}{2} (\hat{n}_x(\hat{n}_x - 1) + \hat{n}_y(\hat{n}_y - 1)) + 2U_2 \hat{n}_x \hat{n}_y + \frac{U_3}{2} (\hat{p}_x^\dagger \hat{p}_x^\dagger \hat{p}_y \hat{p}_y + \text{h.c.}). \quad (\text{S14})$$

It is notable that the pair hopping term,  $\hat{p}_x^\dagger \hat{p}_x^\dagger \hat{p}_y \hat{p}_y + \text{h.c.}$ , naturally arises in the  $p$ -orbital system. This term is crucial in engineering the the TACT Hamiltonian, as we will describe in Sec. S-2.

## S-2 Orbital Squeezing of $p$ -orbital Bosons

In this section, we will treat each two-mode boson as a pseudo-spin-1/2 system and study the dynamics of  $p$ -BEC states under the evolution of  $\hat{H}_{\text{int}}$ .

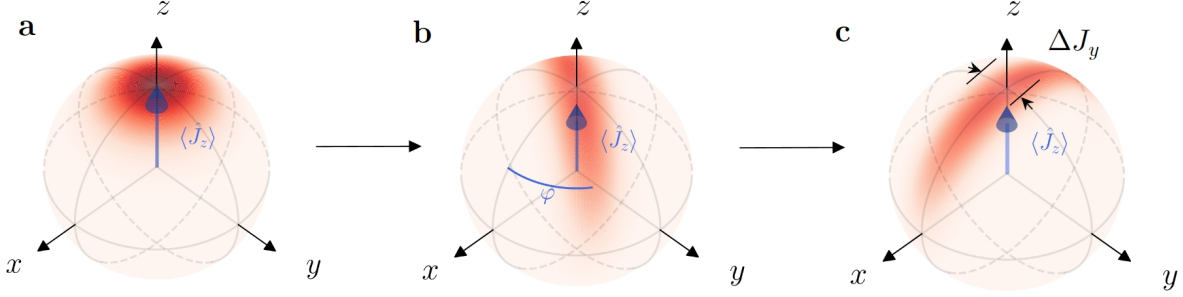


FIG. S3. Husimi-Q function representation of pseudo-spin states. **a**, The initial pseudo-spin coherent state  $|J, J\rangle$ . **b**, A orbital-squeezed state resulting from the evolution of  $|J, J\rangle$  under the Hamiltonian Eq. (S18), exhibiting a squeezing angle  $\varphi$  relative to the  $z$ -axis. **c**, The orbital-squeezed state following a rotation around the  $z$ -axis by  $\varphi$ , enhancing sensitivity to rotations about the  $x$ -axis. The parameters are  $U_1 = 2.5U_2 = 2.5U_3$  (Eq. (S14)) and  $N = 20$ .

## A Schwinger Representation of Angular Momentum

The Schwinger representation of angular momentum [26] is:

$$\hat{J}_z = \frac{1}{2} (\hat{n}_x - \hat{n}_y), \quad (\text{S15})$$

$$\hat{J}_+ = \hat{J}_x + i\hat{J}_y = \hat{p}_x^\dagger \hat{p}_y, \quad \hat{J}_- = \hat{p}_y^\dagger \hat{p}_x, \quad (\text{S16})$$

where we have chosen  $p_x(p_y)$  state to represent the pseudo-spin up (down) state, and  $\hat{J}_z$  measures the population difference between  $p_x$  and  $p_y$ . The initial  $p$ -BEC state is a coherent state,  $|\theta, \varphi\rangle$  (shown in Fig. S3) as:

$$|p_x\rangle^{\otimes N} = |\uparrow\rangle^{\otimes N} = |J = \frac{N}{2}, J_z = \frac{J}{2}\rangle = |\theta = 0, \varphi\rangle, \quad |p_y\rangle^{\otimes N} = |\pi, \varphi\rangle, \quad |p_+\rangle^{\otimes N} = |\pi/2, \pi/2\rangle.$$

Without loss of generality, we will always assume the initial state is prepared in the  $p_x$  condensate  $|p_x\rangle^{\otimes N}$ .

The full pseudo-spin (ps) Hamiltonian, denoted as  $\hat{H}_{\text{ps}} = \hat{H}_0 + \hat{H}_{\text{int}}$ , is rewritten in

terms of angular momentum operators as,

$$\begin{aligned}\hat{H}_{\text{ps}} &= \epsilon \hat{N} + \frac{U_1}{2} \left( \hat{n}_x^2 + \hat{n}_y^2 - \hat{N} \right) + 2U_2 \hat{n}_x \hat{n}_y + \frac{U_3}{2} \left( \hat{p}_x^\dagger \hat{p}_x^\dagger \hat{p}_y \hat{p}_y + \text{h.c.} \right) \\ &= \left( \epsilon - \frac{U_1}{2} \right) \hat{N} + \frac{1}{4} (U_1 + 2U_2) \hat{N}^2 + (U_1 - 2U_2) \hat{J}_z^2 + U_3 (\hat{J}_x^2 - \hat{J}_y^2)\end{aligned}\quad (\text{S17})$$

Since the total particle number  $\hat{N} = \hat{n}_x + \hat{n}_y$  is a conserved quantity,  $\hat{J}^2 = \hat{J}_x^2 + \hat{J}_y^2 + \hat{J}_z^2 = \frac{\hat{N}}{2} \left( \frac{\hat{N}}{2} + 1 \right)$  is also conserved, i.e., the state always evolve in the  $J = N/2$  subspace. The full Hamiltonian (up to a constant energy shift involving only  $\hat{N}$ ) then takes the form:

$$\hat{H}_{\text{ps}} = (3U_3 - U_1) \hat{J}_x^2 - (U_1 - U_3) \hat{J}_y^2. \quad (\text{S18})$$

which reproduces Eq. (2) of the main text.

The full Hamiltonian is a Lipkin-Meshkov-Glick(LMG) Hamiltonian [60, 61] in absence of external fields, which is a superposition of the one-axis-twisting Hamiltonian (OAT)  $\hat{J}_x^2(\hat{J}_y^2)$  and the two-axis-counter-twisting Hamiltonian (TACT)  $\hat{J}_x^2 - \hat{J}_y^2$ . For the checker-board optical lattice, we have  $U_2 = U_3$  by the time-reversal symmetry, and there are 3 special cases in the parameter space: (1)  $U_1 = U_3$  (Shallow lattice limit) gives rise to an OAT Hamiltonian  $\hat{H} = 2U_3 \hat{J}_x^2$ . (2)  $U_1 = 3U_3$  (Deep lattice limit, harmonic limit) also gives rise to an OAT Hamiltonian  $\hat{H} = -2U_3 \hat{J}_y^2$ . (3)  $U_1 = 2U_2$  gives rise to a TACT Hamiltonian  $\hat{H} = U_3(\hat{J}_x^2 - \hat{J}_y^2)$ .

## B Squeezing $p$ -orbital Bosons to Heisenberg Limit

We characterize the level of orbital squeezing by using the squeezing parameter  $\xi_S$  [62] or the metrological squeezing parameter  $\xi_R$  [37, 38] as:

$$\xi_S^2 = \frac{(\min \Delta J_\perp)^2}{N/4}, \quad (\text{S19})$$

$$\xi_R^2 = \frac{N(\min \Delta J_\perp)^2}{|\langle \mathbf{J} \rangle|^2} = \left( \frac{N/2}{|\langle \mathbf{J} \rangle|} \right)^2 \xi_S^2 \geq \xi_S^2. \quad (\text{S20})$$

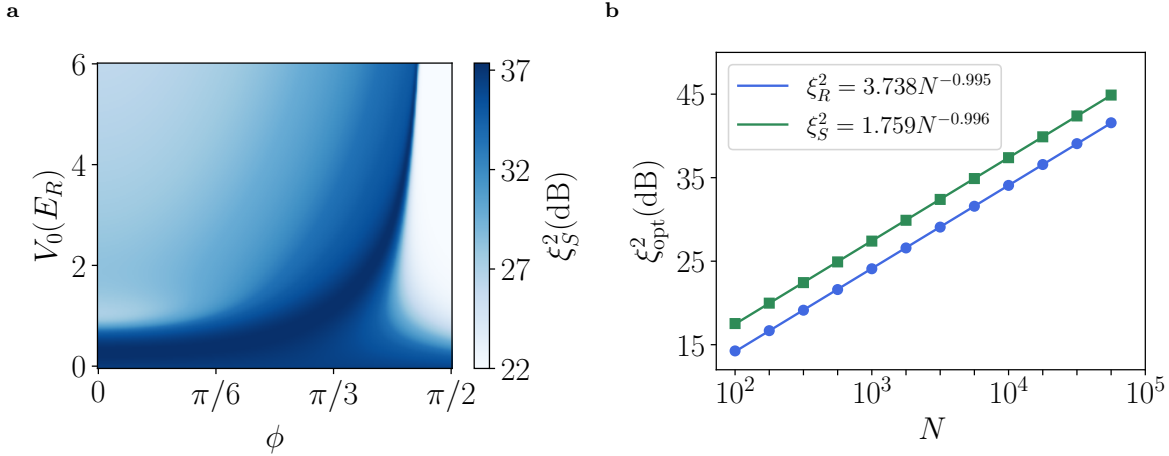


FIG. S4. Squeezing parameter  $\xi^2$  of the state  $|J, J\rangle$  under the time evolution of the Hamiltonian Eq. (S18). **a**,  $\xi_S^2$  for a total particle number  $N = 10^4$ . The optimal squeezing parameter is approximately 37 dB, approaching the Heisenberg limit  $\xi^2 \sim 1/N$ , which corresponds to a 40 dB squeezing. **b**, The scaling of the optimal squeezing parameters with  $N$ . The parameters used are  $V_0 = 6E_R$ ,  $\phi = 0.44857\pi$ , and  $\omega_z = 20\pi$  rad/s. Points represent numerically calculated data, and lines represent fitted curves.

where  $\min \Delta J_\perp$  is the minimal variance of the spin component perpendicular to the mean spin direction  $\langle \mathbf{J} \rangle$ . For our system  $\langle J_x \rangle = \langle J_y \rangle = \langle J_x J_y \rangle = \langle J_y J_z \rangle = \langle J_x J_z \rangle = 0$ , so the mean spin direction is  $\mathbf{e}_z$ . The squeezing effect of different parameters ( $V_0, \phi, N$ ) is shown in Fig. 3 in the main text and Fig. S4.

The metrological squeezing parameter is associated with phase sensitivity in Ramsey spectroscopy as  $\Delta\phi = \xi_R/\sqrt{N}$ . The state is squeezed for  $\xi_R < 1$ , as its noise beats the standard quantum limit (shot-noise limit)  $\Delta\phi < 1/\sqrt{N}$ . Conversely, the Heisenberg uncertainty principle imposes a fundamental limit on this squeezing, asserting that  $\xi_R^2 \geq \xi_S^2 \geq 1/N$  and consequently  $\Delta\phi \geq 1/N$ , establishing the lower bounds for the uncertainty in phase that quantum mechanics allows. The fitted curves in Fig. S4b  $\xi_R^2 = 3.738N^{-0.995}$  and  $\xi_S^2 = 1.759N^{-0.996}$  indicate that the squeezing effect generated by the interaction between  $p$ -orbital bosons achieves the Heisenberg limit. Comparing Fig. 3a in main text



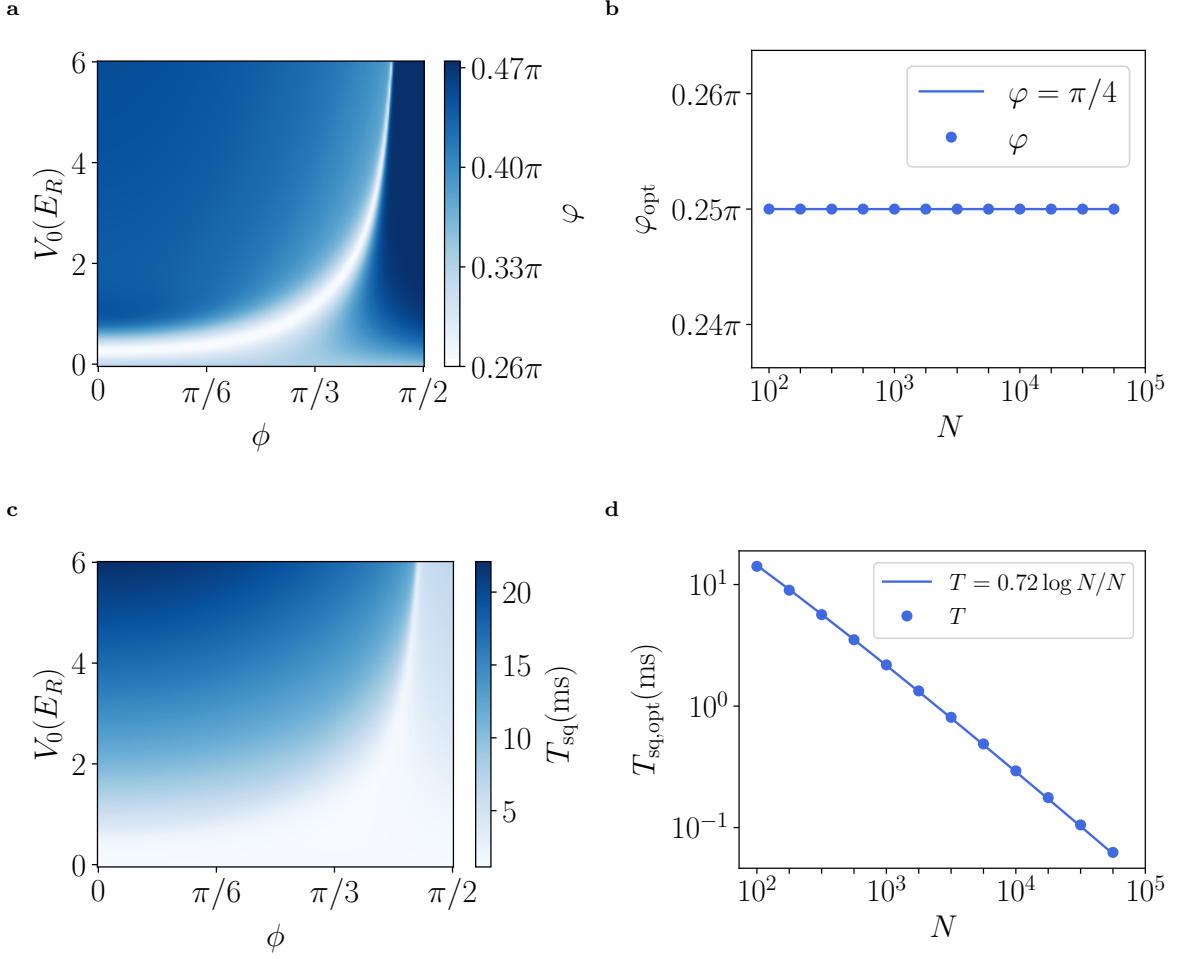


FIG. S5. Squeezing angle  $\varphi$  and squeezing time  $T_{\text{sq}}$  of the spin state  $|J, J\rangle$  under the time evolution of the Hamiltonian in Eq. (S18). **a**,  $\varphi$  as a function of potential parameters with total particle number  $N = 10^4$ . In the OAT limit,  $\varphi$  is close to  $\pi/2$ , while in the TACT limit,  $\varphi$  approaches  $\pi/4$ . **b**, The scaling of the optimal squeezing angle with  $N$ . **c**,  $T_{\text{sq}}$  with total particle number  $N = 10^4$ . **d**, The optimal squeezing time as a function of  $N$ . The parameters here corresponds to  $V_0 = 6E_R$ ,  $\phi = 0.44857\pi$ ,  $\omega_z = 20\pi$  rad/s.

and Fig. S4a, we observe that the optimal squeezing effect is achieved at  $U_1 = 2U_2 = 2U_3$ , where  $\hat{H}_{\text{spin}}$  becomes a TACT Hamiltonian.

Two other important quantities important for our detecting protocol are the optimal squeezing time  $T_{\text{opt}}$  and the optimal squeezing angle  $\varphi$ . The results are provided in Fig. S5.

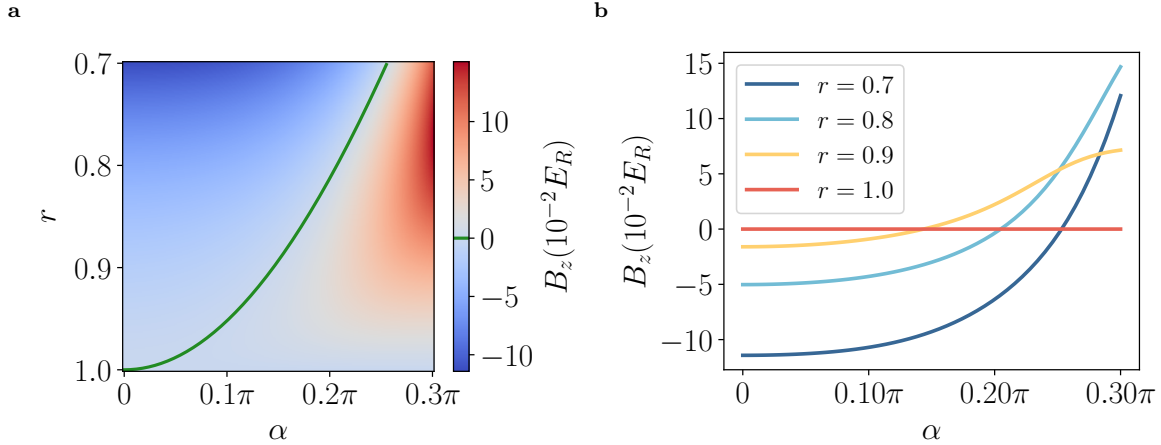


FIG. S6. Effective pseudo-magnetic field  $B_z$  arising from the energy asymmetry between  $p_x$  and  $p_y$  orbitals. (a)  $B_z$  plotted against the reflection coefficient  $r$  and polarization angle  $\alpha$ . The solid green line marks the condition  $r = \cos \alpha$  where the two  $p$ -orbitals are degenerate and the  $D_4$  point group symmetry is partially recovered. (b)  $B_z$  as a function of  $\alpha$  for specific  $r$  values.  $B_z$  is of typical magnitude  $10^{-2}E_R \sim 10^{-1}E_R$ .

## C Rotation about $z$ -axis

As demonstrated in Sec. S-3, the effective interaction between gravitational waves/dark photon dark matter and the lattice induces a tiny rotation about  $x$ -axis. To optimize the detection of this tiny rotation using orbital squeezing techniques, we need to align the most sensitive direction of the orbital squeezed state with the  $x$ -axis (Fig. S3 b-c).

A straightforward method to achieve this alignment involves a rotation about the  $z$ -axis, which can be induced by introducing a pseudo-magnetic field  $B_z \hat{J}_z = B_z (\hat{n}_x - \hat{n}_y)/2$ . This term accounts for the energy asymmetry between  $p_x$  and  $p_y$  orbitals, which can be adjusted by tuning the lattice parameters  $r, t, \alpha$  as defined in Eq. (S1). Taking  $r < 1$ , we have an energy shift between  $p_x$  and  $p_y$  orbitals because the resultant lack of lattice  $D_4$  symmetry [18, 29, 63]. This generates a pseudo-magnetic field along the  $z$ -axis.

In Fig. S6, we provide the results of  $B_z = 2(E^1(\mathbf{Q}_x) - E^1(\mathbf{Q}_y))$ . We find that  $B_z$  has

a typical value about  $5 \times 10^{-2} E_R$ . Therefore, the typical time required to rotate a state squeezed by TACT Hamiltonian about  $z$ -axis by  $\varphi = \pi/4$  is  $T_{\text{rot}}(\pi/4) = \pi\hbar/(4 \times 5 \times 10^{-2} E_R) \simeq 25\mu\text{s}$ .

### S-3 Detecting Gravitational Waves

In this section, we describe the process of sensing gravitational waves (GW) with our orbital atomic sensor. The underlying idea is that when a GW passes through the experimental apparatus, it induces a rotation of the  $p$ -orbital states around the  $x$ -axis of the pseudo-spin Bloch sphere by a minute angle  $\theta$  (see Fig. 4 in the main text). This rotation can be detected, with the sensitivity limited by the quantum noise of atoms and photons, which we will explore in detail in Sec. S-4. Throughout this paper, we use the convention  $\eta^{\mu\nu} = \text{diag}(1, -1, -1, -1)$  and  $x^\mu = (ct, \mathbf{r})$ .

## A Theory

Consider a monochromatic plane gravitational wave traveling along the  $\mathbf{e}_z$  direction, which perturbs the spacetime metric as  $g_{\mu\nu} = \eta_{\mu\nu} + h_{\mu\nu}$ . In the transverse-traceless(TT) gauge, the spacetime metric is given by:

$$h_{\mu\nu} = \begin{pmatrix} 0 & 0 & 0 & 0 \\ 0 & h_+ & h_\times & 0 \\ 0 & h_\times & -h_+ & 0 \\ 0 & 0 & 0 & 0 \end{pmatrix}, \quad (\text{S21})$$

where  $h_+(t, z)$  and  $h_\times(t, z)$  are the strain fields corresponding to the two independent polarization of the GW, plus and cross respectively. The spacetime interval is then expressed

as:

$$ds^2 = g_{\mu\nu}dx^\mu dx^\nu = -c^2dt^2 + (1 - h_+)dX^2 + 2h_\times dXdY + (1 + h_+)dY^2 + dz^2. \quad (\text{S22})$$

The coordinate frame employed here is the TT frame, wherein the coordinate position of a free test mass remains unchanged in the presence of a gravitational wave, provided the test mass is initially at rest [64]. Note that the polarization described here is aligned with the X, Y axes. A complete general-relativistic treatment of  $p$ -orbital bosons in curved spacetime  $g_{\mu\nu}$  involves the interaction between GWs and the bosons, as well as the effect of the GW on the trapping potentials. This is captured by the following action [65]:

$$S[\Psi; g^{\mu\nu}, V] = \int d^4x \sqrt{-g} [g^{\mu\nu} \partial_\mu \Psi^\dagger \partial_\nu \Psi - \kappa |\Psi|^4 - V(\mathbf{r}; g^{\mu\nu}) |\Psi|^2], \quad (\text{S23})$$

where  $g = \det(g_{\mu\nu})$  and  $\kappa$  is the atomic interaction coefficient. The first two terms represent the minimal coupling between atoms and GWs, and the third term  $V$  is given by:

$$V(\mathbf{r}; g^{\mu\nu}) = \frac{m^2 c^2}{2\hbar^2} + V_{\text{lat}}(\mathbf{r}; g^{\mu\nu}) + U_{\text{lat}}(\mathbf{r}; g^{\mu\nu}), \quad (\text{S24})$$

which accounts for the atomic mass, and the GW-induced deformation of the primary lattice  $V_{\text{lat}}$  for trapping atoms and signal lattice potential  $U_{\text{lat}}$  for signal detection. The complete atomic Hamiltonian is expressed as:

$$\hat{H} = \hat{H}_{\text{flat}} + \hat{H}_{\text{GW-B}} + \hat{H}_{\text{GW-EM}}. \quad (\text{S25})$$

Here,  $\hat{H}_{\text{flat}}$  corresponds to the Hamiltonian of  $p$ -orbital atoms in flat spacetime, while  $\hat{H}_{\text{GW-B}}$  and  $\hat{H}_{\text{GW-EM}}$  describe the direct coupling between GWs and bosons, and the photon-mediated coupling between GWs and atoms, respectively. As detailed in [S-3 C](#), the direct GW-boson coupling induces a pseudo-magnetic field along the  $z$ -axis, but with a negligible strength. Additionally, the impact of GWs on the primary optical lattice

potential  $V_{\text{lat}}$  is also found to be insignificant, as shown in [S-3 D](#). In contrast, the GW-induced deformation of the signal optical lattice  $U_{\text{lat}}$ , which has a wavelength twice that of  $V_{\text{lat}}$  and half the wave-vector, results in a detectable pseudo-magnetic field  $B_x$  that couples  $p_x$  and  $p_y$  orbital states. For instance,  $V_{\text{lat}}$  and  $U_{\text{lat}}$  could be generated using lasers with wavelengths of  $\lambda = 532$  nm and  $2\lambda = 1064$  nm, respectively. The expression for  $U_{\text{lat}}$  is given by:

$$U_{\text{lat}}(\mathbf{r}; \phi_U, \Phi_x, \Phi_y) = -U_0 \left\{ 1 + \cos\left(\frac{kx}{2} + \Phi_x\right) \cos\left(\frac{ky}{2} + \Phi_y\right) + \cos\phi_U \left[ \cos\left(\frac{kx}{2} + \Phi_x\right) + \cos\left(\frac{ky}{2} + \Phi_y\right) \right] \right\}, \quad (\text{S26})$$

where  $\Phi_{x,y}$  are tunable phases, and  $\phi_U$  denotes the phase difference between the standing waves of the laser in the X, Y arms having wavelength  $2\lambda$  (to be referred to as  $2\lambda$ -laser in the following). The phases are related with the phase accumulation in X, Y arms (defined in the main text) by  $\Phi_X = \Phi_x - \Phi_y$  and  $\Phi_Y = \Phi_x + \Phi_y$ . We require  $U_0 \ll V_0 = O(E_R)$  so that  $U_{\text{lat}}$  has little effect on the  $p$ -band and lattice structure associated with  $V_{\text{lat}}$ . In this limit, the two-mode approximation Eq. ([S7](#)) is still valid and the contribution of  $U_{\text{lat}}$  to the pseudo-spin Hamiltonian is:

$$\hat{H}_0^U = \sum_{\alpha\beta} J_{\alpha\beta}^U \hat{p}_\alpha^\dagger \hat{p}_\beta = J_{xx}^U \hat{N} + B_x \hat{J}_x, \quad (\text{S27})$$

$$J_{\alpha\beta}^U = \int d^2\mathbf{r} \psi_\alpha^*(\mathbf{r}) U_{\text{lat}}(\mathbf{r}; \phi_U, \Phi) \psi_\beta(\mathbf{r}), \quad (\text{S28})$$

Therefore, the interaction between GWs and  $U_{\text{lat}}$  effectively produces a pseudo-magnetic field  $B_x$  along the  $\mathbf{e}_x$  direction, given by:

$$B_x(\Phi; V_0, \phi) = -2U_0 \sin \Phi_x \sin \Phi_y \eta(V_0, \phi), \quad (\text{S29})$$

with the dimensionless “efficiency” parameter  $\eta$  depicted in [Fig. S7](#). The derivation of



this expression and the definition of  $\eta$  are detailed in S-3B.

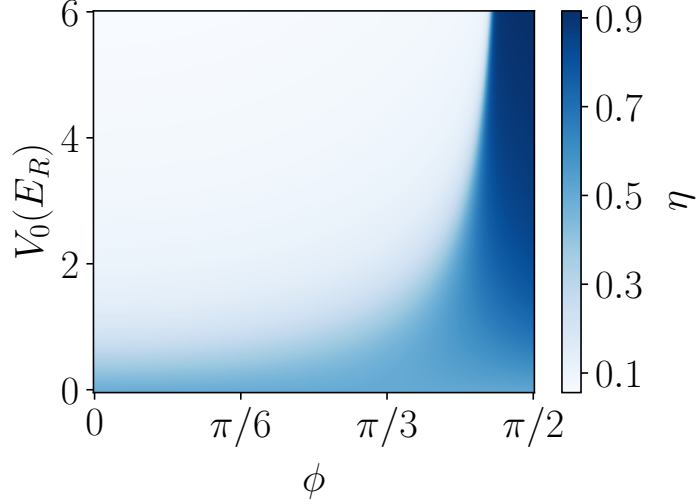


FIG. S7. Efficiency parameter  $\eta$  in Eq. (S44) as a function of potential parameters  $V_0$  and  $\phi$ . The efficiency increases with  $V_0$  and exceeds its harmonic limit (Eq. (S45)),  $1/e$ , across a broad range of potential parameters.

For simplicity, we first consider a plus-polarized GW propagating along the  $\mathbf{e}_z$  direction (the polarization and angular patterns are studied in Sec. S-4D). In the presence of such a GW,  $U_{\text{lat}}$  gets a (phase or real space) shift as  $U_{\text{lat}}(\mathbf{r}; \phi_U, \Phi_x, \Phi_y) \rightarrow U_{\text{lat}}(\mathbf{r}; \phi_U + \Delta\phi_U, \Phi_x, \Phi_y - \Delta\Phi/2) = U_{\text{lat}}(\mathbf{r} + \mathbf{l}_U; \phi_U + \Delta\phi_U, \Phi)$ . Here,  $\mathbf{l}_U = (0, -\Delta\Phi/k)$  (shown in Eq. (S46)). Similarly, the pseudo-magnetic field  $B_x$  shift as  $B_x(\Phi_x, \Phi_y) \rightarrow B_x(\Phi_x, \Phi_y - \Delta\Phi/2)$ , which is most sensitive to  $h_+$  when  $\Phi_x = \pi/2$  and  $\Phi_y = 0$  in the flat spacetime. As a result,  $B_x = 0$  in the absence of GW, and it gains a finite value when GW passes by:

$$B_x^{\text{GW}}(h_+; V_0, \phi, \mathcal{F}) = \eta(V_0, \phi) U_0 \Delta\Phi. \quad (\text{S30})$$

The measured GW signal also depends on the frequency of GWs and measuring protocol.

The rotation angle  $\theta$  acquired for a measurement with duration  $T$  is:

$$\theta = \int_0^T dt y(t) B_x^{\text{GW}}(t)/\hbar, \quad (\text{S31})$$

where  $y(t)$  is the modulation function (window function) of the pulse sequence applied in the measuring protocol. The rotated angle is detected at the end of each detection cycle by measuring the orbital polarization  $\langle J_y \rangle$  using time-of-flight experiment (see Fig. 4 in the main text).

For a monochromatic GW wave  $h_+(t) = h_{0,+} \cos(2\pi ft + \alpha)$ , the rotation angle is:

$$\theta = \mathcal{T}_\theta(f)h_{0,+} = \eta \frac{U_0 T}{\hbar} W(f, \alpha, T) \mathcal{T}_\Phi(f)h_{0,+}, \quad (\text{S32})$$

where the protocol-dependent weight function  $W(f, \alpha, T)$  is defined as the Fourier transformation of  $y(t)$ :

$$W(f, \alpha, T) = \frac{1}{T} \int_0^T dt y(t) \cos(2\pi ft + \alpha). \quad (\text{S33})$$

The weight function  $W$  is analyzed in detail in Sec. S-3 E. The transfer function of the Michelson Interferometer with FP cavity is [64]:

$$\mathcal{T}_\Phi(f) = \frac{\Delta\Phi}{h_{0,+}} = \frac{1}{2} \times 2KL \operatorname{sinc} \left( 2\pi f \frac{L}{c} \right) \frac{2\mathcal{F}/\pi}{\sqrt{1 + (f/f_p)^2}}, \quad (\text{S34})$$

where  $L$  is the arm length,  $\mathcal{F}$  is the finesse of the FP cavity, and  $f_p = c/(4\mathcal{F}L)$  is the pole frequency. The additional factor 1/2 accounts for the fact that  $U_{\text{lat}}$  is generated by laser with wavevector  $K/2$ . The shift of phase accumulation  $\Phi_{X,Y}$  of lasers in the X, Y arms is given by:

$$\Delta\Phi_X = \frac{1}{2} \mathcal{T}_\Phi(f)h_{0,+}, \quad (\text{S35})$$

$$\Delta\Phi_Y = -\frac{1}{2} \mathcal{T}_\Phi(f)h_{0,+}. \quad (\text{S36})$$

The transfer function of a pure MI (without FP cavity) corresponding to our primary  $\lambda$ -laser is:

$$\mathcal{T}_{\Phi'}(f) = \frac{\Delta\Phi'}{h_{0,+}} = 2KL' \operatorname{sinc} \left( 2\pi f \frac{L'}{c} \right). \quad (\text{S37})$$

where we have assumed the  $\lambda$ -laser is cycling in a pure MI with arm length  $L' \sim 1\text{m}$  (see Fig.S1c). The arm-length of LIGO interferometer is  $L = 4\text{km}$ , for which the sinc terms in Eq. (S34) and Eq. (S37) are well approximated by 1 in the frequency region  $f < 10^3\text{Hz}$  of our interest in this study.

## B Lattice-deformation-mediated Interaction between GW and Bosons

In this section we demonstrate the derivation of pseudo-magnetic field  $B_x$  in Eq. (S29), and analyze its behaviour in the presence of a GW, under the condition where  $V_0/U_0 \gg 1$ . We first divide the whole integral Eq. (S28) into contribution from different unit cells  $\Omega_{\mathbf{R}}$  as:

$$J_{\alpha\beta}^U = \sum_{\mathbf{R}} (-1)^{R_\alpha+R_\beta} \int_{\Omega_0} d^2\mathbf{r} \psi_\alpha^*(\mathbf{r}) U_{\text{lat}}(\mathbf{r} + \mathbf{R}; \phi_U, \Phi) \psi_\beta(\mathbf{r}), \quad (\text{S38})$$

where  $\psi_\alpha(\mathbf{r} + \mathbf{R}) = (-1)^{R_\alpha} \psi_\alpha(\mathbf{r})$  is used. Given that the lattice vectors of  $U_{\text{lat}}$  are  $2\mathbf{a}_1$  and  $2\mathbf{a}_2$ , we decompose  $\mathbf{R} = (2m + m_r)\mathbf{a}_1 + (2n + n_r)\mathbf{a}_2$  with  $m_r, n_r \in \mathbb{Z}_2$  denoting the relative position in the enlarged unit cell. Using  $\sum_{m,n} 1 = 1/4 \sum_{\mathbf{R}} 1 = N_{\text{lat}}/4$ , we obtain:

$$J_{\alpha\beta}^U = \frac{1}{4} \sum_{m_r, n_r \in \mathbb{Z}_2} (-1)^{R_\alpha+R_\beta} \int d^2\mathbf{r} \psi_\alpha^*(\mathbf{r}) U_{\text{lat}}(\mathbf{r} + m_r\mathbf{a}_1 + n_r\mathbf{a}_2) \psi_\beta(\mathbf{r}). \quad (\text{S39})$$

The summation of  $m_r, n_r$  leads to:

$$\frac{1}{4} \sum_{m_r, n_r \in \mathbb{Z}_2} (-1)^{m_r+n_r} U_{\text{lat}}(\mathbf{r} + m_r\mathbf{a}_1 + n_r\mathbf{a}_2) = -U_0 \cos(kx/2 + \Phi_x) \cos(ky/2 + \Phi_y), \quad (\text{S40})$$

$$\frac{1}{4} \sum_{m_r, n_r \in \mathbb{Z}_2} U_{\text{lat}}(\mathbf{r} + m_r\mathbf{a}_1 + n_r\mathbf{a}_2) = -U_0. \quad (\text{S41})$$

By inserting these into (S38), and noticing that  $\psi_{x(y)}$  has odd parity along  $x(y)$  direction, we obtain:

$$J_{xx}^U = J_{yy}^U = -U_0, \quad (\text{S42})$$

$$J_{xy}^U = J_{yx}^U = -U_0 \sin \Phi_x \sin \Phi_y \eta(V_0, \phi), \quad (\text{S43})$$

$$\eta(V_0, \phi) = \int d^2\mathbf{r} \psi_x^*(\mathbf{r}; V_0, \phi) \sin(kx/2) \sin(ky/2) \psi_\beta(\mathbf{r}; V_0, \phi). \quad (\text{S44})$$

From Eq. (S43), we obtain the expression of pseudo-magnetic field

In the harmonic limit  $V_0/E_R \gg 1$ , we expand the Bloch functions in terms of the localized Wannier functions of  $V_{\text{lat}}$  at each site  $\mathbf{R}$  as  $\psi_\alpha(\mathbf{r}) = N_{\text{lat}}^{-1/2} \sum_{\mathbf{R}} (-1)^{R_\alpha} \omega_\alpha(\mathbf{r} - \mathbf{R})$  (Fig. S2). The Wannier functions are given by  $\omega_\alpha(\mathbf{r}) = \sqrt{\frac{2}{\pi l_H^2}} \frac{x_\alpha}{l_H} e^{-r^2/2l_H^2}$  with the characteristic length  $l_H = (\frac{\hbar^2}{Mk^2V_0(1+\cos\phi)})^{1/4}$ . The dimensionless parameter  $\eta(V_0, \phi)$  takes a form of:

$$\eta_{\text{har}}(V_0, \phi) = \frac{\pi^2 l_H^2}{2a^2} \exp\left(-\frac{\pi^2 l_H^2}{2a^2}\right). \quad (\text{S45})$$

The maximal value of  $\eta(V_0, \phi)$  in the harmonic limit is  $1/e$ , which occurs when  $\pi^2 l_H^2/2a^2 = 1$ . Numerical results of  $\eta(V_0, \phi)$  taking into account the unharmonicity of the lattice potential are shown in Fig. S7. We observe that in general  $\eta$  is not necessarily less than  $1/e$ .

We now consider the influence of a GW on the pseudo-magnetic-field  $B_x$ . For a monochromatic plus-polarized GW with frequency  $f$ , the change of arm length imparts an additional phase  $\Delta\Phi_{X,Y} = \pm\Delta\Phi/2 = \pm\mathcal{T}_\Phi(f)h_{0,+}/2$  (see Eq. (S34) for the definition of  $\mathcal{T}_\Phi$ ) to the counter-propagating electromagnetic field with wavelength  $K = 2\pi/\lambda$  upon reflection from the X, Y arm ends. As a result, the optical lattice is modified by the GW

from its flat spacetime form Eq. (S26) as follows:

$$\begin{aligned}
U_{\text{lat}}(\mathbf{X}, \mathbf{Y}; U_0, \phi_U) &\rightarrow -\frac{U_0}{4} \left| \left( e^{iKX/2} + e^{-i(\Phi_X + \Delta\Phi_X)} e^{-iKX/2} \right) \right. \\
&\quad \left. + e^{i(\phi_U + \Phi_Y/2)} \left( e^{iKY/2} + e^{-i(\Phi_Y + \Delta\Phi_Y)} e^{-iKY/2} \right) \right|^2 \\
&= U_{\text{lat}}(\mathbf{X} + \Delta\mathbf{X}, \mathbf{Y} + \Delta\mathbf{Y}; U_0, \phi_U + \Delta\phi_U), \tag{S46}
\end{aligned}$$

with  $\Delta\mathbf{X} = -\Delta\mathbf{Y} = \Delta\Phi/K$  are the real space shift of the lattice caused by the GW,  $\Delta\phi_U = (\Delta\Phi_X - \Delta\Phi_Y)/2 = \Delta\Phi/2$  accounts for the relative phase shift and  $\Delta\Phi_x = (\Delta\Phi_X + \Delta\Phi_Y)/2 = 0$ ,  $\Delta\Phi_y = (\Delta\Phi_Y - \Delta\Phi_X)/2 = -\Delta\Phi/2$ . In the  $(x, y)$  coordinate, the lattice deformation can be described as  $U_{\text{lat}}(\mathbf{r}; \phi_U, \Phi_x, \Phi_y) \rightarrow U_{\text{lat}}(\mathbf{r} + \mathbf{l}_U; \phi + \Delta\phi_U, \Phi_x, \Phi_y)$  in the presence of the GW with  $\mathbf{l}_U = \frac{1}{\sqrt{2}}(\Delta\mathbf{X} + \Delta\mathbf{Y}, \Delta\mathbf{Y} - \Delta\mathbf{X}) = (0, -\Delta\Phi/k)$ .

The GW-induced lattice deformation can also be seen as a shift of phase parameters because  $U_{\text{lat}}(\mathbf{r} + \mathbf{l}_U; \phi + \Delta\phi_U, \Phi_x, \Phi_y) = U_{\text{lat}}(\mathbf{r}; \phi + \Delta\phi_U, \Phi_x, \Phi_y - \Delta\Phi/2)$ . Consequently, the coefficients  $J_{\alpha\beta}^U$  undergo a corresponding shift  $J_{\alpha\beta}^U(\Phi_x, \Phi_y) \rightarrow J_{\alpha\beta}^U(\Phi_x, \Phi_y - \Delta\Phi/2)$  in the presence of a GW. Setting  $\Phi_x = \pi/2, \Phi_y = 0$  results in  $J_{xy}^U = 0$  in the flat spacetime, and it gains a finite value  $J_{xy}^U = \eta U_0 \Delta\Phi/2$  when a GW passes by.

For the same reason, the potential  $V_{\text{lat}}$  gets a real space shift  $\mathbf{l}_V = (0, -\Delta\Phi'/(2k))$  and a phase shift  $\Delta\phi = \mathcal{T}_\Phi(f)/\mathcal{T}_{\Phi'}(f) \times \Delta\phi_U$  (see Eq. (S34) and Eq. (S37)).

## C Direct Interaction between GW and Bosons

This section analyzes the interaction directly between the GW and the trapped bosons. Note that  $\Phi$  is used to denote a scalar field instead of the phase accumulation in the arm in this section.

Consider a scalar field  $\Phi$  with  $\Phi^4$  interaction minimally coupled to the gravity back-

ground  $g^{\mu\nu}$  [65]:

$$S[\Phi; h^{\mu\nu}] = \int d^4x \sqrt{-g} \left( g^{\mu\nu} \partial_\mu \Phi^\dagger \partial_\nu \Phi - \frac{1}{2} \frac{m^2 c^2}{\hbar^2} |\Phi|^2 - \kappa |\Phi|^4 \right) \quad (\text{S47})$$

with  $g \equiv \det(g_{\mu\nu})$  the determinant of the covariant metric tensor and  $\kappa$  the interaction coefficient between bosons. In the presence of a weak gravitational wave  $h_{\mu\nu}$  described by Eq. (S21), the spacetime metric is perturbed as  $g_{\mu\nu} = \eta_{\mu\nu} + h_{\mu\nu}$ . Its inverse is  $g^{\mu\nu} = \eta^{\mu\nu} - h^{\mu\nu}$  with  $h^{\mu\nu} = \eta^{\mu\rho} \eta^{\nu\lambda} h_{\rho\lambda}$ . As a result, we have a perturbative expansion:

$$\sqrt{-g} = \sqrt{1 - h_+^2 - h_\times^2} = 1 + O(h^2), \quad (\text{S48})$$

$$g^{\mu\nu} \partial_\mu \Phi^\dagger \partial_\nu \Phi = \eta^{\mu\nu} \partial_\mu \Phi^\dagger \partial_\nu \Phi - \left[ h_+ |\partial_x \Phi|^2 + h_\times (\partial_x \Phi^\dagger \partial_y \Phi + \text{h.c.}) - h_+ |\partial_y \Phi|^2 \right]. \quad (\text{S49})$$

We now take the non-relativistic limit. We first factor out the fast oscillating phase term, corresponding to the rest energy of  $\Phi$ , by defining the new field  $\Psi$  as:

$$\Phi(\mathbf{r}, t) = \frac{\hbar}{\sqrt{2m}} \exp\left(-i \frac{mc^2}{\hbar} t\right) \Psi(\mathbf{r}, t). \quad (\text{S50})$$

The new field  $\Psi(\mathbf{r}, t)$  now only has slowly time variations and satisfies  $\partial_t \Psi \ll -imc^2 \Psi / \hbar$ . By substituting Eq. (S50) into Eq. (S47) and drop the  $\partial_t \Psi^\dagger \partial_t \Psi$  term, we obtain the action of  $\Psi$  in the GW background in the non-relativistic limit to the first order of  $h$  as:

$$S[\Psi; h^{\mu\nu}] = \int d^4x \left\{ i\hbar \Psi^\dagger \partial_t \Psi - \frac{\hbar^2}{2m} \left[ |\nabla \Psi|^2 + h_+ (|\partial_x \Psi|^2 - |\partial_y \Psi|^2) + h_\times (\partial_x \Psi^\dagger \partial_y \Psi + \text{h.c.}) \right] - \frac{\hbar^4}{4m^2} \kappa |\Psi|^4 \right\}. \quad (\text{S51})$$

The conjugate momentum field of  $\Psi$  is described by:

$$\pi = \frac{\partial \mathcal{L}_{\text{GW}}}{\partial (\partial_t \Psi)} = i\hbar \Psi^\dagger. \quad (\text{S52})$$

As a result, the Hamiltonian describing the coupling between bosons and gravitational

wave is:

$$\hat{H} = \int d^3x (\pi \partial_t \Psi - \mathcal{L}_{\text{GW}}) = \hat{H}_B + \hat{H}_{\text{GW-B}}, \quad (\text{S53})$$

$$\hat{H}_B = \int d^3x \left( \frac{\hbar^2}{2m} |\nabla \hat{\Psi}|^2 + \frac{\hbar^4}{4m^2} \kappa |\hat{\Psi}|^4 \right), \quad (\text{S54})$$

$$\hat{H}_{\text{GW-B}} = \int d^3x \left[ h_+ \left( |\partial_x \hat{\Psi}|^2 - |\partial_y \hat{\Psi}|^2 \right) + h_\times (\partial_x \hat{\Psi}^\dagger \partial_y \hat{\Psi} + \text{h.c.}) \right]. \quad (\text{S55})$$

In the following we analyze the effect of GW under the two-mode approximation (S7). The field operators  $\hat{\Psi}$  in 3-dimensional space are now expanded as  $\hat{\Psi}(\mathbf{r}, z) = \psi_x(\mathbf{r})\phi_0(z)\hat{p}_x + \psi_y(\mathbf{r})\phi_0(z)\hat{p}_y$  with  $\phi_0(z)$  the normalized ground state of the trap potential along the  $\mathbf{e}_z$  direction. The direct interaction between the gravitational wave and the  $p$ -orbital bosons,  $\hat{H}_{\text{GW-B}}$  is obtained as:

$$\hat{H}_{\text{GW-B}} = \sum_{\alpha\beta} J_{\alpha\beta}^{\text{GW-B}} \hat{p}_\alpha^\dagger \hat{p}_\beta, \quad (\text{S56})$$

$$J_{\alpha\beta}^{\text{GW-B}} = \int d^2x \left[ h_+ (\partial_x \psi_\alpha^*(\mathbf{r}) \partial_x \psi_\beta(\mathbf{r}) - \partial_y \psi_\alpha^*(\mathbf{r}) \partial_y \psi_\beta(\mathbf{r})) + h_\times (\partial_x \psi_\alpha^*(\mathbf{r}) \partial_y \psi_\beta(\mathbf{r}) + \text{h.c.}) \right]. \quad (\text{S57})$$

By lattice translation symmetry, the coupling between the two  $p$ -orbitals  $J_{xy}^{\text{GW-B}}$  vanishes.

And for the diagonal terms  $J_{xx}^{\text{GW-B}}$  and  $J_{yy}^{\text{GW-B}}$ , we have:

$$J_{xx}^{\text{GW-B}} = -J_{yy}^{\text{GW-B}} = h_+ \int d^2x (|\partial_x \psi_x(\mathbf{r})|^2 - |\partial_y \psi_x(\mathbf{r})|^2), \quad (\text{S58})$$

considering the parity symmetry of the Bloch function  $\psi_x(-x, y) = -\psi_x(x, y)$  and  $\psi_y(x, -y) = -\psi_y(x, y)$ . As a consequence, the direct coupling between GW and bosons lead to an energy shift between  $p_{x,y}$  orbitals and generates a pseudo-magnetic field along the  $z$ -axis, as detailed in Sec. S-2 C. Its magnitude is given by:

$$B_z^{\text{GW-B}} = 2J_{xx}^{\text{GW-B}} \leq 2h_+ \int d^2x (|\partial_x \psi_x(\mathbf{r})|^2 + |\partial_y \psi_x(\mathbf{r})|^2) = 2h_+ \epsilon_k(\mathbf{Q}_x), \quad (\text{S59})$$

where the inequality holds because  $|\partial_\alpha \psi_\beta(\mathbf{r})|^2$  is non-negative. Here,  $\epsilon_k(\mathbf{Q}_x)$  represents the two-dimensional kinetic energy of the Bloch states and is typically of order  $O(E_R)$ . The ratio between the direct GW-Boson coupling  $B_z^{\text{GW-B}}$  and the  $2\lambda$ -laser mediated  $B_x$  is given by:

$$\frac{B_z^{\text{GW-B}}}{B_x} \leq \frac{2\epsilon_k(\mathbf{Q}_x)}{\eta U_0 \Delta \Phi} \sim \frac{1}{KL\mathcal{F}} \sim \frac{1}{10^{10}\mathcal{F}}, \quad (\text{S60})$$

where we have used Eq. (S29). This ratio indicates that the direct coupling between GWs and bosons is approximately ten orders of magnitude smaller than the  $2\lambda$ -laser mediated coupling between GWs and bosons. Therefore,  $B_z^{\text{GW-B}}$  is negligible when considering the interaction of GWs with our orbital atomic sensor.

## D Interaction between GW and the Optical Lattice $V_{\text{lat}}$

This section examines the effects of a gravitational wave (GW) on the primary optical lattice created by a  $\lambda$ -laser. As a GW passes through, it modulates the phase of the laser beam at its own frequency by changing the effective path length of the laser beam. This modulation induces a deformation in the optical lattice, denoted as  $(\delta V_{\text{lat}})_{\text{GW}}$ . Within the two-mode approximation, this deformation further leads to a modification of the single-body Hamiltonian, expressed as:

$$\hat{H}_{\text{GW}}^V = \sum_{\alpha\beta} J_{\alpha\beta}^V \hat{p}_\alpha^\dagger \hat{p}_\beta, \quad J_{\alpha\beta}^V = \int d^2\mathbf{r} \psi_\alpha^*(\mathbf{r}) (\delta V_{\text{lat}})_{\text{GW}} \psi_\beta(\mathbf{r}), \quad (\text{S61})$$

(Note that  $J^V$  arises from the GW-induced lattice deformation  $(\delta V)_{\text{GW}}$  and represents the change in the coupling coefficients due to the GW. In contrast,  $J^U$ , as defined in the main text and Eq. (S28), has non-zero components even in the flat spacetime.)



Now we have:

$$J_{\alpha\beta}^V = \int d^2\mathbf{r} \psi_{\alpha}^*(\mathbf{r})(\mathbf{l}_V \cdot \nabla + \Delta\phi\partial_{\phi})V_{\text{lat}}(\mathbf{r}; \phi)\psi_{\beta}(\mathbf{r}), \quad (\text{S62})$$

where  $\mathbf{l}_V = (0, -\Delta\Phi'/(2k))$  is GW-induced lattice shift in the real space, as analyzed in Sec. S-3B. Due to the translation symmetry  $\psi_{\alpha}(\mathbf{r} + \mathbf{R}) = (-1)^{R_{\alpha}}\psi_{\alpha}(\mathbf{r})$  and  $V_{\text{lat}}(\mathbf{r} + \mathbf{R}) = V_{\text{lat}}(\mathbf{r})$ , we have  $J_{xy}^V = J_{yx}^{V*} = 0$ . The remaining two coefficients  $J_{xx}^V, J_{yy}^V$  are non-vanishing. Due to the  $D_4$  symmetry of  $p_{x,y}$  orbitals,  $J_{xx}^V = J_{yy}^V$ , indicating that the  $\lambda$ -laser mediated coupling between GW and bosons only leads to an overall energy shift of the  $p$ -orbital states, which cannot be detected.

Under the harmonic approximation, these two coefficients are given by,

$$\begin{aligned} J_{xx}^V = J_{yy}^V &= \int d^2\mathbf{r} \omega_x^*(\mathbf{r})(\mathbf{l}_V \cdot \nabla + \Delta\phi\partial_{\phi})V_{\text{lat}}(\mathbf{r}; \phi)\omega_x(\mathbf{r}) \\ &= 2V_0 \sin\phi \left(1 - \frac{\pi^2 l_H^2}{a^2}\right) \exp\left(-\frac{\pi^2 l_H^2}{a^2}\right) \Delta\phi, \end{aligned} \quad (\text{S63})$$

## E Detecting Protocol

This section elaborates on the detecting protocol illustrated in Fig. 4 of the main text. Our detection strategy involves a consecutive repetition of measurement cycles (Fig. 4 in the main text). Each cycle consists of five steps, taking a total amount of time,  $T = 1.11\text{s}$ . The photons carrying the GW signal interact with the  $p$ -orbital bosons in the fourth step for a time duration of one second, which is reasonably accessible to the current cold atom technology.

For an alternating monochromatic GW described by  $h_+(t) = h_{0,+} \cos(2\pi ft + \alpha)$ , the induced pseudo-magnetic field  $B_x(t) \propto \cos(2\pi ft + \alpha)$  oscillates temporally, leading to a temporal averaging of the rotation angle  $\theta$  to zero in the high-frequency limit  $fT_{\text{life}} \gg 1$ . To restore our ideal detecting sensitivity, we apply  $\pi$ -pulse sequences to the pseudo-spin,

facilitating the accumulation of  $\theta$  in different half cycles of the pseudo-magnetic field.

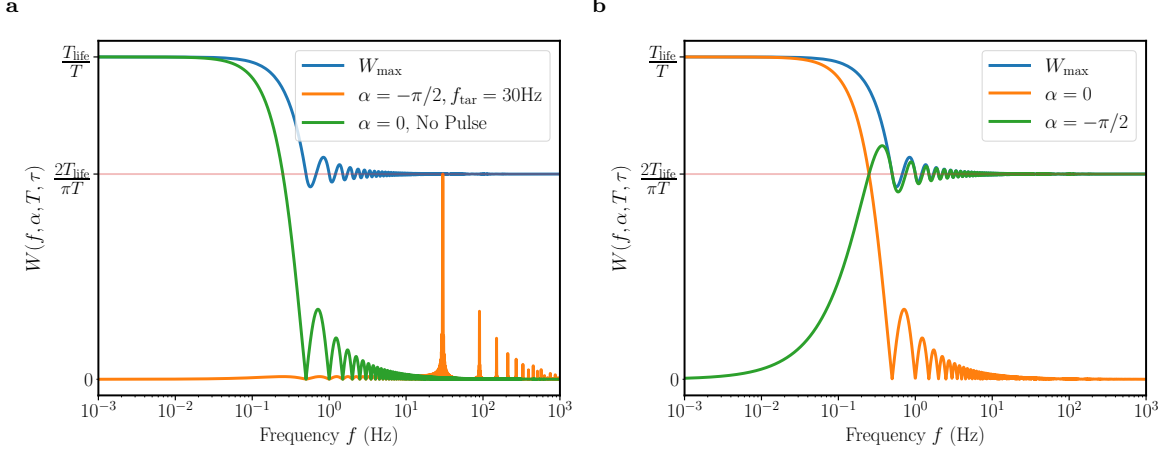


FIG. S8. Weight function defined in Eq. (S64). **a**: Weight function without lock-in technique compared with the maximum weight function  $W_{\max}$  (blue line).  $W$  with  $\alpha = -\pi/2$ ,  $f_{\text{tar}} = 30\text{Hz}$  (orange line) has a maximum sensitivity at  $f = f_{\text{tar}}$ , while  $W$  with  $\alpha = 0$  and no  $\pi$  pulse (green line) achieves maximum weight function in low-frequency regime. **b**: Frequency locked-in weight function  $W(f, \alpha, \tau = 1/(2f))$ .  $W_{\max}$  corresponds to  $\alpha = 0$  in the low frequency regime  $f < 0.1\text{Hz}$  and  $\alpha = -\pi/2$  in the high frequency  $f > 1\text{Hz}$  regime.

We adopt a simple periodic dynamical decoupling (PDD) multi-pulse sequence within our protocol. This sequence involves the application of evenly spaced  $\hat{R}_z(\pi)$  pulses with duration  $t_p$  at every  $\tau$  time units, accompanied by a window function  $y(t)$  that alternates in sign with each pulse application. As detailed in S-2 C, the duration of a single  $\pi$  pulse is approximately  $t_p \simeq 100 \mu\text{s}$ , which is significantly less than the minimum period  $\tau_{\min} = 1/(2f_{\max})$  for our frequency range of interest between  $10^{-3}$  Hz and  $10^3$  Hz. The weight function in Eq. (S33), is given as (Fig. S8, [36]):

$$W(f, \alpha, T, \tau) = \frac{1}{2\pi f T} \left[ \sin(\alpha) - (-1)^n \sin(2\pi f T_{\text{life}} + \alpha) + 2 \sum_{j=1}^n (-1)^j \sin(2\pi f t_j + \alpha) \right]. \quad (\text{S64})$$

Here,  $t_j$  represents the time of the  $j$ -th  $\pi$ -pulse application with  $0 < t_j = j\tau < T_{\text{life}}$  for  $j = 1, 2, \dots, n$ . From Eq. (S64), we observe: (1) for a quasi-static signal with

$fT_{\text{life}} \ll 1$ , no pulses are necessary, and the weight function simplifies to  $W = -\frac{T_{\text{life}}}{T} \text{sinc}(\pi f T_{\text{life}}) \cos(\pi f T_{\text{life}} + \alpha)$ . (2) for an ac signal, the weight function peaks at  $f = 1/(2\tau)$  with a bandwidth  $\Delta f \simeq 1/T_{\text{life}}$ , and the peak value is  $W \simeq -\frac{2T_{\text{life}}}{\pi T} \sin(\alpha)$ . As a consequence, to detect a signal at the target frequency  $f_{\text{tar}}$ , we apply pulse sequences with spacing  $\tau = 1/(2f_{\text{tar}})$ .

For both dc and ac signals, the accumulated phase  $\theta$  is dependent on the frequency  $f$  and the initial phase  $\alpha$  of the signal, which are generally unknown a priori. According to Ref. [66], the sensitivity is moderately reduced by a factor of  $\sqrt{2(1 + \sqrt{2}/\pi^2)} \simeq 1.5$  due to this uncertainty. However, quantum (double) lock-in techniques, as detailed in [49–51], enable the extraction of this information, thereby maximizing our detection sensitivity. The corresponding weight function is given by  $W_{\text{max}} = \max_{\alpha} W(f, \alpha, T, \tau = \frac{1}{2f}) = \frac{T_{\text{life}}}{T}$  for  $fT_{\text{life}} \ll 1$  and  $W_{\text{max}} = \frac{2T_{\text{life}}}{\pi T}$  for  $fT_{\text{life}} \gg 1$ .

## S-4 Noise Budgets of the Orbital Atomic Sensor

In order to analyze the sensitivity of our orbital atomic sensor, we need to calculate the time-evolution of the variance of  $p$ -orbital polarization in its interaction with the LIGO light. Quantum fluctuations of both atoms and photons are incorporated consistently in the framework of quantum optics. In this section, we present the quantum optics theory and analyze the noise budgets to determine the strain sensitivity of our gravitational wave (GW) detection protocol, as illustrated in Figure 2a. The parameters of our orbital atomic sensor is summarized in Table S1.

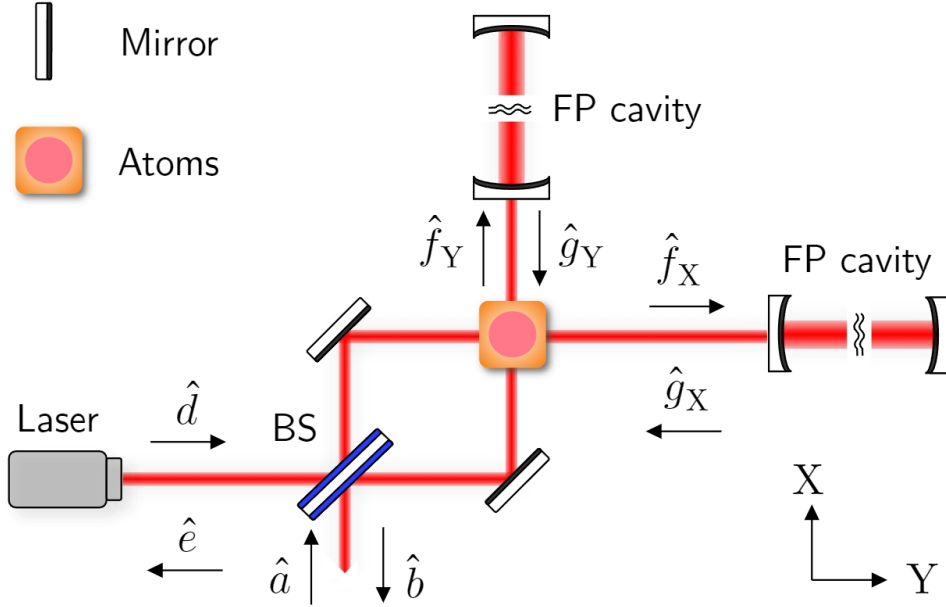


FIG. S9. Electric field mode operators in the orbital atomic sensor setup, as defined in Eq. (S65) and Eq. (S72). For clarity, only the  $2\lambda$ -laser (1064 nm) is depicted. The distances from the beam-splitter (BS) to the Fabry-Perot cavity (FP cavity) mirrors and the cavity lengths are assumed to be integer multiples of  $2\lambda$ .

## A Quantum Optical Description of the Atomic Sensor

This section provides a quantum optics framework to describe the detection process of our orbital atomic sensor. A standard quantum optics notation [67] is adopted here.

### 1 Quantized Electric Fields and Its Interfering Lattice

The positive frequency part of the quantized electric field in the X arm propagating to the right (as shown in Fig. S9) is expressed as (For simplicity, at this moment we do not write down the operators with angular frequency near  $2\omega_0$ , corresponding to our  $\lambda$ -laser,

and we will discuss their contribution to the noise in Sec. [S-4 A 3](#)):

$$\hat{E}_R^{(+)}(t) = \sqrt{\frac{2\pi\hbar\omega_0}{\mathcal{A}c}} e^{-i\omega_0 t} \left[ \hat{f}_{X,0} + \int_0^\infty \left( \hat{f}_{X,+} e^{-i\Omega t} + \hat{f}_{X,-} e^{i\Omega t} \right) \frac{d\Omega}{2\pi} \right], \quad (\text{S65})$$

$$= \sqrt{\frac{2\pi\hbar\omega_0}{\mathcal{A}c}} e^{-i\omega_0 t} \left( F_0 + \hat{F}_X(t) \right). \quad (\text{S66})$$

Here,  $\omega_0 = cK/2$  is the angular frequency of the  $2\lambda$ -laser (also called the carrier frequency), and  $\mathcal{A} = \pi w^2/2$  is the effective cross sectional area of the beam with  $w$  the beam waist. The operator  $\hat{f}_0$  is the annihilation operator for the  $\omega_0$  mode, with  $F_0 = \sqrt{P_{\text{arm},2\lambda}/\hbar\omega_0}$  being its expectation value. The power of light in each Michelson Interferometer arm is  $P_{\text{arm}}$ , and the circulating power inside the cavity is  $P_{\text{cav}} = 2\mathcal{F}P_{\text{arm}}/\pi$ . The operators  $\hat{f}_{X,\pm}(\Omega) = \hat{f}_{X,\omega_0\pm\Omega}$  correspond to the side band annihilation operators at angular frequency  $\omega_0 \pm \Omega$ . Given that our interesting frequency regime satisfies  $\Omega/2\pi < 10^3\text{Hz} \ll \omega_0/2\pi \sim 10^{15}\text{Hz}$ , we approximate all  $\omega \pm \Omega$  with  $\omega$  in the square root, and extend our integral over  $\Omega$  to infinity. The classical amplitude  $F_0$  of  $\hat{a}_0$  is taken as real, and the operator  $\hat{F}$  encapsulates the quantum fluctuations. These fluctuations are described by:

$$\hat{F}_X = \Delta\hat{f}_X + \int_0^\infty \left( \hat{f}_{X,+} e^{-i\Omega t} + \hat{f}_{X,-} e^{i\Omega t} \right) \frac{d\Omega}{2\pi} = \text{Her}(\hat{F}) + i\text{AHer}(\hat{F}), \quad (\text{S67})$$

where  $\Delta\hat{f}_X = \hat{f}_{X,0} - F_0$ ,  $\text{Her}(\hat{F}_X)$  and  $\text{AHer}(\hat{F}_X)$  are the hermitian and anti-hermitian part of  $\hat{F}$  respectively, given by:

$$\text{Her}(\hat{F}_X) = \frac{1}{2} \left( \Delta\hat{f}_X + \sqrt{2} \int_0^\infty \hat{f}_{X,1} e^{-i\Omega t} \frac{d\Omega}{2\pi} \right) + \text{h.c.}, \quad (\text{S68})$$

$$\text{AHer}(\hat{F}_X) = \frac{1}{2} \left( -i\Delta\hat{f}_X + \sqrt{2} \int_0^\infty \hat{f}_{X,2} e^{-i\Omega t} \frac{d\Omega}{2\pi} \right) + \text{h.c.}, \quad (\text{S69})$$

with  $\hat{f}_1 = (\hat{f}_+ + \hat{f}_-^\dagger)/\sqrt{2}$  and  $\hat{f}_2 = (\hat{f}_+ - \hat{f}_-^\dagger)/\sqrt{2}i$  being the two-photon amplitude and phase quadrature operators [\[68\]](#). (Subscripts have been omitted for simplicity). Their

commutation relations are:

$$\left[ \hat{f}_1(\Omega), \hat{f}_1^\dagger(\Omega') \right] = \left[ \hat{f}_2(\Omega), \hat{f}_2^\dagger(\Omega') \right] = O\left(\frac{\Omega}{\omega_0}\right) \simeq 0, \quad (\text{S70})$$

$$\left[ \hat{f}_1(\Omega), \hat{f}_2^\dagger(\Omega') \right] = \left[ \hat{f}_1^\dagger(\Omega), \hat{f}_2(\Omega') \right] = 2\pi i \delta(\Omega - \Omega'). \quad (\text{S71})$$

Following a similar approach to Eq. (S66), the electric field in the Y arm propagating upwards is described by

$$\hat{E}_U^{(+)}(t) = \sqrt{\frac{2\pi\hbar\omega_0}{\mathcal{A}c}} e^{-i\omega_0 t} e^{i(\phi_U + \Phi_Y/2)} \left( F_0 + \hat{F}_Y(t) \right) \quad (\text{S72})$$

where the additional phase  $\phi_U + \Phi_Y/2$  represents the phase difference between the classical electric fields in Y and X arms. The total electric fields in the X, Y arm are therefore:

$$\hat{E}^{(+)}(t, \mathbf{r}) = \hat{E}_X^{(+)}(t, \mathbf{r}) + \hat{E}_Y^{(+)}(t, \mathbf{r}), \quad (\text{S73})$$

$$\hat{E}_X^{(+)}(t, \mathbf{r}) = e^{i\text{KX}/2} \hat{E}_R^{(+)}(t) + e^{-i\text{KX}/2} e^{-i\Phi_X} \hat{E}_L^{(+)}(t), \quad (\text{S74})$$

$$\hat{E}_Y^{(+)}(t, \mathbf{r}) = e^{i\text{KY}/2} \hat{E}_U^{(+)}(t) + e^{-i\text{KY}/2} e^{-i\Phi_Y} \hat{E}_D^{(+)}(t), \quad (\text{S75})$$

where  $\Phi_{X,Y}$  are the tunable phases. The subscripts  $R, L, U, D$  denote the right, left, up and down propagating fields, respectively. Their corresponding electric field operators are obtained by substituting  $\hat{f}$  with  $\hat{f}_X, \hat{g}_X$  into Eq. (S66) and  $\hat{f}_Y, \hat{g}_Y$  into Eq. (S72). Note that all four fields share the same classical amplitude  $F_0$ . A linear transformation is performed at the beam-splitter, described in terms of the two-photon operators as:

$$\hat{f}_{X,j} = \frac{\hat{d}_j - \hat{a}_j}{\sqrt{2}}, \quad \hat{f}_{Y,j} = \frac{\hat{d}_j + \hat{a}_j}{\sqrt{2}}, \quad (\text{S76})$$

for  $j = 1, 2$ , where  $\hat{a}$  and  $\hat{d}$  represent annihilation operators of the dark port input and bright port input respectively, as shown in Fig. S9. And the input-output relation of the

FP cavities (Fig. S9) are expressed as [67]:

$$\hat{g}_1(\Omega) = \Delta\hat{g}_1 = e^{2i\beta} \hat{f}_1, \quad (\text{S77})$$

$$\hat{g}_2(\Omega) = \eta_{\text{YX}} e^{i\beta} \frac{\tilde{h}}{h_{\text{SQL}}} \sqrt{\mathcal{K}} + \Delta\hat{g}_2, \quad \Delta\hat{g}_2(\Omega) = e^{2i\beta} (\hat{f}_2 - \mathcal{K}\hat{f}_1), \quad (\text{S78})$$

where  $\eta_{\text{YX}}$  takes the value +1 for Y arm and -1 for X arm. The standard quantum limit of a conventional interferometer is represented by  $h_{\text{SQL}}(\Omega) = \sqrt{8\hbar/M\Omega^2 L^2}$ . The Fourier transform of the GW strain  $h(t)$  is denoted by  $h(\Omega)$ , satisfying:

$$\tilde{h}(\Omega) = \int_{-\infty}^{\infty} h(t) e^{i\Omega t} \frac{d\Omega}{2\pi}. \quad (\text{S79})$$

Since  $h(t)$  is real, it follows that  $\tilde{h}^*(\Omega) = \tilde{h}(-\Omega)$ , and thus  $g_j^\dagger(\Omega) = g_j(-\Omega)$ . The phase shift  $\beta$  induced by the FP cavity and the optomechanical coupling strength  $\mathcal{K}$  are defined as:

$$\beta(\Omega) = \arctan\left(\frac{\Omega}{\Omega_p}\right), \quad \mathcal{K}(\Omega) = \frac{16\omega_0 P_{\text{arm},2\lambda}}{ML^2} \frac{1}{\Omega^2(\Omega_p^2 + \Omega^2)}, \quad (\text{S80})$$

with  $\Omega_p = \pi c/(2\mathcal{F}L)$  being the angular frequency of the pole frequency  $f_p$  of FP cavity, as defined around Eq. (S34). Note that the cavity length is assumed to be adjusted to integer multiple of the carrier wavelength, ensuring no net phase shift for the carrier light travelling between two end mirrors of the cavity or upon reflection from the front mirror. Consequently,  $\Delta\hat{g}_{\text{X,Y}} = \Delta\hat{f}_{\text{X,Y}}$ .

Now, the optical lattice experienced by atoms is treated as an operator acting on the photon Hilbert space. This operator includes its classical value  $U_{\text{lat}}$  (see Eq. (S26)) and quantum fluctuations:

$$\begin{aligned} \hat{U}_{\text{lat}}(t, \mathbf{r}) &= -\frac{1}{2} \alpha_{2\lambda} \overline{\hat{E}^{(-)}(t, \mathbf{r}) \hat{E}^{(+)}(t, \mathbf{r})}, \quad (\text{S81}) \\ &\simeq -\frac{\hat{U}_0}{4} \left| \left( e^{i\text{KX}/2} e^{i\hat{\Phi}_L} + e^{-i\text{KX}/2} e^{-i\hat{\Phi}_X} e^{i\hat{\Phi}_R} \right) + e^{i(\phi_U + \Phi_Y/2)} \left( e^{i\text{KY}/2} e^{i\hat{\Phi}_U} + e^{-i\text{KY}/2} e^{-i\hat{\Phi}_Y} e^{i\hat{\Phi}_D} \right) \right|^2. \end{aligned}$$

Here,  $\alpha_{2\lambda}$  is the atomic polarizability at wavelength  $2\lambda$ , and  $\overline{A(t)}$  represents the time average of  $A(t)$  over a short period, typically of several multiples  $2\pi/\omega_0$ . In the second line we have omitted the second-order fluctuations  $O(\hat{F}^2/|F_0|^2)$ . The lattice depth is now expressed as  $\hat{U}_0 = U_0 + \Delta\hat{U}_0$ , where  $\Delta\hat{U}_0$  accounts for quantum fluctuation. (As will be detailed in Sec. S-4 A 3,  $\Delta\hat{U}_0$  will not contribute to our sensitivity at the leading order of fluctuation, hence its expression is not elaborated here.) The differential accumulated phase after round trips in the X,Y arms is given by:

$$\Delta\hat{\Phi} = \hat{\Phi}_X - \hat{\Phi}_Y, \quad (\text{S82})$$

$$\hat{\Phi}_X = \Phi_X + \hat{\Phi}_L - \hat{\Phi}_R = \Phi_X + \frac{1}{F_0} \left( \text{AHer}(\hat{F}_X) - \text{AHer}(\hat{G}_X) \right), \quad (\text{S83})$$

$$\hat{\Phi}_Y = \Phi_Y + \hat{\Phi}_U - \hat{\Phi}_D = \Phi_Y + \frac{1}{F_0} \left( \text{AHer}(\hat{F}_Y) - \text{AHer}(\hat{G}_Y) \right). \quad (\text{S84})$$

Using Eq. (S69) and Eq. (S78), the expression of  $\hat{\Phi}_\alpha$  is simplified to:

$$\begin{aligned} \hat{\Phi}_\alpha &= \Phi_\alpha + \frac{1}{2F_0} \left[ \left( -i\Delta\hat{f}_\alpha + i\Delta\hat{g}_\alpha + \sqrt{2} \int_0^\infty (\hat{f}_{\alpha,2} - \hat{g}_{\alpha,2}) e^{-i\Omega t} \frac{d\Omega}{2\pi} \right) + \text{h.c.} \right], \\ &= \Phi_\alpha - \frac{\sqrt{2}}{2F_0} \int_{-\infty}^\infty \left[ (e^{2i\beta} - 1) \hat{f}_{\alpha,2} - \mathcal{K}e^{2i\beta} \hat{f}_{\alpha,1} + \eta_{YX} e^{i\beta} \frac{\tilde{\hbar}}{h_{\text{SQL}}} \sqrt{2\mathcal{K}} \right] e^{-i\Omega t} \frac{d\Omega}{2\pi}, \end{aligned}$$

with  $\alpha = X, Y$ . Consequently, the differential phase shift is given by:

$$\begin{aligned} \Delta\hat{\Phi} &= \Phi_X - \Phi_Y + \frac{1}{F_0} \int_{-\infty}^\infty \left[ (e^{2i\beta} - 1) \hat{a}_2 - \mathcal{K}e^{2i\beta} \hat{a}_1 + e^{i\beta} \frac{\tilde{\hbar}}{h_{\text{SQL}}} \sqrt{2\mathcal{K}} \right] e^{-i\Omega t} \frac{d\Omega}{2\pi}, \\ &= \Phi_X - \Phi_Y + \int_{-\infty}^\infty \mathcal{T}_\Phi(f) e^{i\beta} (\tilde{\hbar} + \hat{h}_n) e^{-i2\pi ft} df, \end{aligned} \quad (\text{S85})$$

where the transfer function  $\mathcal{T}_\Phi(f) = \mathcal{T}_\Phi(-f)$  takes the form of:

$$\mathcal{T}_\Phi(f) = \frac{1}{F_0} \frac{\sqrt{2\mathcal{K}}}{h_{\text{SQL}}} = \frac{1}{2} \times 2\text{KL} \frac{2\mathcal{F}/\pi}{\sqrt{1 + (f/f_p)^2}}, \quad (\text{S86})$$



which recovers Eq. (S34). The fluctuation  $\hat{h}_n$  is expressed as:

$$\hat{h}_n(f) = h_{\text{SQL}} \frac{2i \sin \beta \hat{a}_2 - e^{i\beta} \mathcal{K} \hat{a}_1}{\sqrt{2\mathcal{K}}}. \quad (\text{S87})$$

It is important to note that the fluctuating term  $\hat{h}_n(f)$  originating  $(\hat{\Phi}_L - \hat{\Phi}_R) - (\hat{\Phi}_U - \hat{\Phi}_D)$  differs from the extra-cavity readout term  $\hat{\Phi}_D - \hat{\Phi}_R$  of a conventional interferometer like LIGO, which has the expression:

$$\hat{h}_{n,\text{LIGO}}(f) = h_{\text{SQL}} \frac{e^{i\beta} \hat{a}_2 - e^{i\beta} \mathcal{K} \hat{a}_1}{\sqrt{2\mathcal{K}}}. \quad (\text{S88})$$

Compare Eqs. (S87) and (S88), we can see that the shot noise for our atomic sensor (corresponding to  $\hat{a}_2$ ) is reduced in the low frequency regime  $2 \sin \beta < 1$ , or equivalently  $f < \sqrt{3} f_p$  with  $f_p$  the pole frequency of the FP cavity.

## 2 Interaction between Atoms and Quantized Light

The Hamiltonian that describes the interaction between atoms and the quantized electric field, expanding upon the classical light case shown in Eqs. (S27) and (S28), is:

$$\hat{H}_{\text{atom-photon}} = \sum_{\alpha\beta} \hat{J}_{\alpha\beta}^U \hat{p}_\alpha^\dagger \hat{p}_\beta = \hat{J}_{xx}^U \hat{N} + \hat{B}_x \hat{J}_x, \quad (\text{S89})$$

$$\hat{J}_{\alpha\beta}^U = \int d^2\mathbf{r} \psi_\alpha^*(\mathbf{r}) \hat{U}_{\text{lat}}(t, \mathbf{r}) \psi_\beta(\mathbf{r}), \quad (\text{S90})$$

where  $\hat{J}_{\alpha\beta}^U$  is an operator that incorporates both classical expectation values and quantum fluctuations of the photon states. The term  $\hat{J}_{xx}^U \hat{N}$  commutes with the operator  $\hat{J}_y$  that we measure, and thus do not contribute to the signal or noise. The interacting Hamiltonian that contributes to our measurement is:

$$\hat{H}(t) = y(t) \hat{B}_x \hat{J}_x, \quad (\text{S91})$$

where  $y(t)$  is the window function corresponding to our detecting protocol (see Sec. S-3 E).

By setting  $\Phi_X = \Phi_Y = \pi/2$  and substituting Eq. (S85) into Eq. (S29), the expression for the pseudo-magnetic field is obtained as:

$$\hat{B}_x(t) = \eta(V_0, \phi) \hat{U}_0 \int_{-\infty}^{\infty} \mathcal{T}_\Phi(f) e^{i\beta} (\tilde{h} + \hat{h}_n) e^{-i2\pi ft} df, \quad (\text{S92})$$

The orbital rotation angle  $\theta$  about  $\mathbf{e}_z$  axis, acquired for a measurement with duration  $T$ , now includes quantum fluctuations:

$$\hat{\theta} = \int_0^T dt y(t) \hat{B}_x(t) / \hbar, \quad (\text{S93})$$

$$= \frac{\eta \hat{U}_0 T}{\hbar} \int_{-\infty}^{\infty} \mathcal{T}_\Phi(f) Y(f, \beta) (\tilde{h} + \hat{h}_n) df, \quad (\text{S94})$$

where  $Y(f, \beta)$  is defined as the Fourier transform of  $e^{i\beta} y(t)$ :

$$Y(f, \beta(f)) = \frac{1}{T} \int_0^T e^{i\beta} y(t) e^{-i2\pi ft} dt, \quad (\text{S95})$$

whose real part is the weight function defined in Eq. (S33).

### 3 Measurement Uncertainty

In our protocol (as depicted in Fig. 4 of the main text), we measure the orbital polarization  $\langle J_y \rangle$  after a time evolution  $T$  under the interacting Hamiltonian Eq. (S91), starting from the initial product state  $|\psi\rangle = |\xi_R\rangle_{\text{atom}} \otimes |\alpha\rangle_{\text{photon}}$ . Here,  $|\xi_R\rangle_{\text{atom}}$  is the Heisenberg-limited atomic squeezed state, and  $|\alpha\rangle_{\text{photon}} = |\alpha\rangle_{\omega_0} \otimes_{\Omega} |0_{\omega_0 \pm \Omega}\rangle$  is the coherent state of the  $\hat{d}_0$  mode entering the beam-splitter (see Figure S9). All dark port input modes are assumed to be in the vacuum state. After a time evolution of duration  $T$ , the product state becomes entangled between atoms and photons:

$$|\psi_T\rangle = e^{-i \int_0^T dt \hat{H}(t) / \hbar} |\psi\rangle = e^{-i \hat{\theta} \hat{J}_x} |\psi\rangle, \quad (\text{S96})$$

with the orbital rotation angle  $\hat{\theta}$  defined in Eq. (S94). The expectation value of our  $\hat{J}_y$  and  $\hat{J}_y^2$  measurement (to leading order) are:

$$\langle \hat{J}_y \rangle_T = \langle \cos \hat{\theta} \hat{J}_y - \sin \hat{\theta} \hat{J}_z \rangle \simeq -\langle \hat{\theta} \rangle \langle \hat{J}_z \rangle, \quad (\text{S97})$$

$$\langle \hat{J}_y^2 \rangle_T = \langle \cos^2 \hat{\theta} \hat{J}_y^2 - \sin \hat{\theta} \cos \hat{\theta} \{ \hat{J}_y, \hat{J}_z \} + \sin^2 \hat{\theta} \hat{J}_z^2 \rangle \simeq \langle \hat{J}_y^2 \rangle + \langle \hat{\theta}^2 \rangle \langle \hat{J}_z^2 \rangle, \quad (\text{S98})$$

where  $\langle \hat{A} \rangle_T$  and  $\langle \hat{A} \rangle$  denote expectation values of  $\hat{A}$  with state  $|\psi\rangle_T$  and  $|\psi\rangle$  respectively. We have also used the fact that  $\langle \hat{J}_y \rangle = \langle \hat{J}_y \hat{J}_z \rangle = 0$  for our orbital squeezed state. From Eq. (S98), we identify two main sources of measurement noise: the atomic projection noise  $\langle \hat{J}_y^2 \rangle = |\langle J_z \rangle|^2 (\Delta\theta)_{\text{proj}}^2$ , and the photonic quantum fluctuation  $\langle \hat{\theta}^2 \rangle$ . In the absence of a GW signal, the fluctuation  $\Delta\hat{U}_0$  does not contribute to  $\langle \hat{\theta}^2 \rangle$  at the leading order of fluctuation. The variance  $\langle \hat{\theta}^2 \rangle$  is calculated according to Eq. (S94),

$$\langle \hat{\theta}^2 \rangle = \left( \frac{\eta U_0 T}{\hbar} \right)^2 \int_{-\infty}^{\infty} \int_{-\infty}^{\infty} \mathcal{T}_{\Phi}(f) \mathcal{T}_{\Phi}(f') Y(f, \beta) Y(f', \beta') \langle \hat{h}_n(f) \hat{h}_n(f') \rangle df df', \quad (\text{S99})$$

$$= \int_0^{\infty} |\mathcal{T}_{\theta}(f)|^2 S_{\text{photon}}(f) df, \quad (\text{S100})$$

where  $\mathcal{T}_{\theta}(f) = \eta U_0 T W_{\text{max}}(f) \mathcal{T}_{\Phi}(f) / \hbar$  and  $W_{\text{max}}(f) = |Y(f, \beta)|$ . (For the definition of weight function  $W$  and its maximum  $W_{\text{max}}$ , please refer to Sec. S-3 E). The single-sided noise spectral density  $S_{\text{photon}}(f)$  is defined by:

$$\langle \hat{h}_n(f) \hat{h}_n(f') \rangle = \langle \hat{h}_n(f) \hat{h}_n(-f')^{\dagger} \rangle = \frac{1}{2} S_{\text{photon}}(f) \delta(f + f'). \quad (\text{S101})$$

The factor 1/2 accounts for the fact that  $S_{\text{photon}}(f)$  is single-sided (instead of double-sided) and satisfies  $S_{\text{photon}}(f) = S_{\text{photon}}(-f)$ . By inserting Eq. (S87) into Eq. (S101), we

obtain:

$$S_{\text{photon}}(f) = h_{\text{SQL}}^2 \frac{4 \sin^2 \beta + \mathcal{K}^2}{2\mathcal{K}} = S_{\text{shot},2\lambda}(f) + S_{\text{rad},2\lambda}(f), \quad (\text{S102})$$

$$S_{\text{shot},2\lambda}(f) = h_{\text{SQL}}^2 \frac{2 \sin^2 \beta}{\mathcal{K}} = \frac{2\hbar(2\pi f)^2}{c\text{K}P_{\text{arm},2\lambda}}, \quad (\text{S103})$$

$$S_{\text{rad},2\lambda}(f) = h_{\text{SQL}}^2 \frac{\mathcal{K}}{2} = \left( \frac{8}{ML(2\pi f)^2} \right)^2 \frac{\hbar\text{K}P_{\text{arm},2\lambda}}{2c} \left( \frac{2\mathcal{F}/\pi}{\sqrt{1 + (f/f_p)^2}} \right)^2, \quad (\text{S104})$$

where  $S_{\text{shot},2\lambda}(f)$  (Fig. S14b) originating from  $(e^{2i\beta} - 1)\hat{a}_1$  represents the quantum fluctuation of the phase of dark port input state, and  $S_{\text{rad},2\lambda}(f)$  (Fig. S14a) stemming from  $k\hat{a}_2$  represents the fluctuation of the position of test masses induced by the quantum fluctuation of the radiation pressure. It is worth noting that the photonic noise  $S_{\text{photon}}(f)$  can be further reduced by injecting photonic squeezed states [45–48].

Then, let us deal with the noise arising from the  $\lambda$ -laser, which is used to generate the primary lattice (see Fig. S1 for a detailed optical layout). Its interaction with gravitational waves also creates two side-bands at angular frequency  $2\omega_0 \pm \Omega$  (note that  $2\omega_0 = c\text{K} = 2\pi c/\lambda$ ), and these modes contribute to the electric field as:

$$\hat{E}_{R,\lambda}^{(+)}(t) = \sqrt{\frac{2\pi\hbar\omega_0}{\mathcal{A}c}} e^{-2i\omega_0 t} \int_0^\infty \left( \hat{f}_{X,2\omega_0+\Omega} e^{-i\Omega t} + \hat{f}_{X,2\omega_0-\Omega} e^{i\Omega t} \right) \frac{d\Omega}{2\pi}, \quad (\text{S105})$$

and similarly for all the electric fields propagating along other directions as described in Sec. S-4 A. The optical lattice generated by the  $\lambda$ -laser is given by:

$$\hat{V}_{\text{lat}}(t, \mathbf{r}) = -\frac{\hat{V}_0}{4} \left| \left( e^{i\text{K}X} e^{i\hat{\Phi}'_R} + e^{-i\hat{\Phi}'_X} e^{i\hat{\Phi}'_L} e^{-i\text{K}X} \right) + e^{i\phi} \left( e^{i\hat{\Phi}'_U} e^{i\text{K}Y} + e^{i\hat{\Phi}'_D} e^{-i\hat{\Phi}'_Y} e^{-i\text{K}Y} \right) \right|^2,$$

where  $\hat{V}_0$ ,  $\Delta\hat{\Phi}'$ ,  $\hat{\phi}$  now all contain quantum corrections. However, these corrections do not contribute noises to Eq. (S98). Although they do influence  $\eta(V_0, \phi)$ , the fluctuation of  $\eta$  does not produce noise in the absence of a GW signal.

Now suppose a plus-polarized monochromatic GW, described by  $h_+(t) = h_{0,+} \cos(2\pi ft + \alpha)$  with  $\tilde{h}(f') = h_{0,+} [e^{i\alpha}\delta(f' - f) + e^{-i\alpha}\delta(f' + f)]/2$ , interacts with our

atomic sensor, then Eq. (S97) is reduced to:

$$\langle \hat{J}_y \rangle_T = -|\langle J_z \rangle| \frac{\eta U_0 T}{\hbar} W(f, \alpha + \beta) h_{0,+} = -|\langle J_z \rangle| \mathcal{T}_\theta(f) h_{0,+}, \quad (\text{S106})$$

where we assume lock-in techniques are used to maximize  $W(f, \alpha + \beta)$  (see Section S-3 E).

The variance of our  $\hat{J}_y$  measurement when  $h_{0,+} = 0$  is given by:

$$(\Delta J_y)^2 = \langle \hat{J}_y^2 \rangle_T = |\langle J_z \rangle|^2 ((\Delta\theta)_{\text{proj}}^2 + (\Delta\theta)_{\text{photon}}^2). \quad (\text{S107})$$

Here, the photonic quantum fluctuation is represented by  $(\Delta\theta)_{\text{photon}}^2$ , which is defined to be  $\langle \hat{\theta}^2 \rangle$ , whose expression is given by Eq. (S100).  $|\langle J_z \rangle|$  in Eq. (S98) are approximated with  $|\langle J_z \rangle|^2$  because that  $(\Delta J_z)^2 / |\langle J_z \rangle|^2 \sim 1/N$  vanishes when  $N$  is large. The signal-to-noise-ratio (SNR) of our measurement is given by:

$$\text{SNR} = \frac{\langle \hat{J}_y \rangle_T}{(\Delta J_y)} = \frac{|\mathcal{T}_\theta(f)| h_{0,+}}{[(\Delta\theta)_{\text{proj}}^2 + \int_0^\infty |\mathcal{T}_\theta(f')|^2 S_{\text{photon}}(f') df']^{1/2}}. \quad (\text{S108})$$

For a periodic GW with frequency  $f$ , the SNR is given in terms of the strain sensitivity  $\sqrt{S_n(f)}$  as [64],

$$\text{SNR} = \sqrt{\frac{T}{S_n(f)}} h_{0,+}. \quad (\text{S109})$$

Combining Eq. (S108) and Eq. (S109), the square of strain sensitivity of our orbital atomic sensor is derived as:

$$S_n(f) = T \left( \frac{(\Delta\theta)_{\text{proj}}}{\mathcal{T}_\theta(f)} \right)^2 + T \frac{\int_0^\infty |\mathcal{T}_\theta(f')|^2 S_{\text{photon}}(f') df'}{|\mathcal{T}_\theta(f)|^2}, \quad (\text{S110})$$

$$\simeq S_{\text{atom}}(f) + \frac{T}{T_{\text{life}}} S_{\text{photon}}(f),$$

$$\simeq S_{\text{atom}}(f) + S_{\text{photon}}(f), \quad (\text{S111})$$

where the noise spectral density contributed by atoms is  $S_{\text{atom}}(f) = T ((\Delta\theta)_{\text{proj}} / \mathcal{T}_\theta(f))^2$ .

In the second line, we have used the fact that  $W_{\text{max}}$  has a bandwidth  $\Delta f = 1/T_{\text{life}}$  (see

Sec. S-3E) and so does  $\mathcal{T}_\theta(f)$ . For our current settings, with  $T = 1.11\text{s}$  and  $T_{\text{life}} = 1\text{s}$ , the ratio  $T/T_{\text{life}}$  leads to a reduction of the photon noise sensitivity  $S_{\text{photon}}^{1/2}$  by 0.2dB, which is thus negligible. This is further confirmed by our numerical simulation results, as shown in Figure S10. By substituting Eq. (S32) into equation S111, we obtain an expression of  $S_{\text{atom}}$  as:

$$S_{\text{atom}}^{1/2}(f) = \sqrt{T} \frac{(\Delta\theta)_{\text{proj}}}{\mathcal{T}_\theta(f)} = \frac{\hbar}{\eta U_0 \sqrt{T}} \frac{(\Delta\theta)_{\text{proj}}}{W_{\text{max}}(f) KL} \frac{\sqrt{1 + (f/f_p)^2}}{2\mathcal{F}/\pi}. \quad (\text{S112})$$

The frequency-dependent behavior of  $S_{\text{atom}}$  is depicted in Figure S14d.

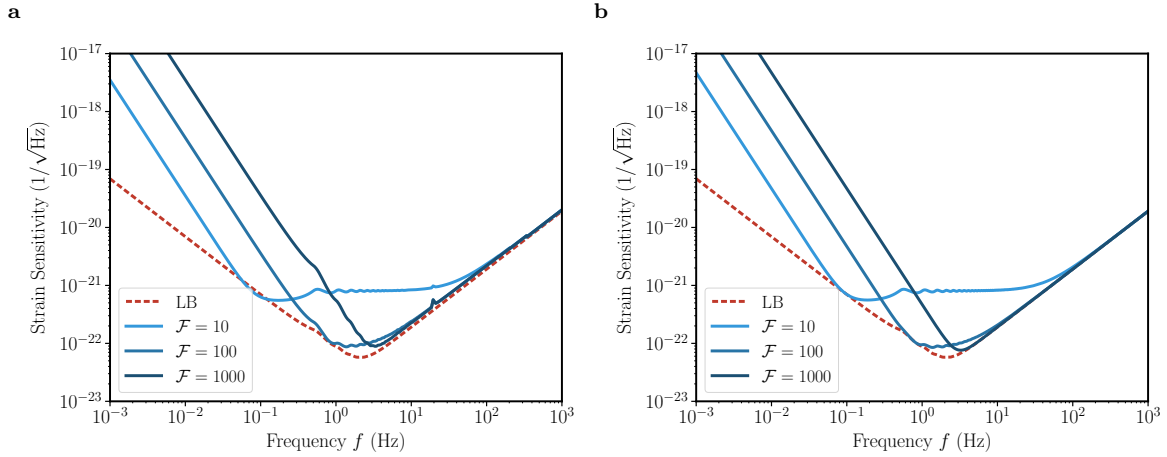


FIG. S10. Comparison of sensitivity curves: **a**, derived from the exact formula Eq. (S110); **b**, derived from the approximate formula Eq. (S111). The difference between the sensitivities in these two plots is less than 0.2 dB, which justifies the approximation in Eq. (S111).  $\mathcal{F}$  stands for the finesse of cavities. LB represents the optimal sensitivity obtained by varying cavity finesse.

## B Calculation of the Full Strain Sensitivity Curve

In conclusion, considering the fundamental noises of our atomic sensor, which include the quantum projection noise of atoms and quantum fluctuations of photon, the full strain

sensitivity Eq. (S111) is given by:

$$S_n(f) = S_{\text{atom}}(f) + S_{\text{photon}}(f), \quad (\text{S113})$$

$$= \frac{S_0(f)}{2} \left( \frac{1}{\mathcal{A}(f, \mathcal{F})} + \mathcal{A}(f, \mathcal{F}) \right) + S_{\text{shot}, 2\lambda}(f). \quad (\text{S114})$$

where the dependence on cavity finesse is absorbed into  $\mathcal{A}$ . The expressions of  $S_0(f)$  and  $\mathcal{A}$  are given by:

$$S_0(f) = \frac{16\hbar}{ML^2(2\pi f)^2} \frac{(\Delta\theta)_{\text{proj}}}{\eta U_0 W(f, T)} \sqrt{\frac{\hbar P_{\text{BS}, 2\lambda}}{2KcT}}, \quad (\text{S115})$$

$$\mathcal{A}(f, \mathcal{F}) = \frac{4}{M(2\pi f)^2} \frac{\eta U_0 W(f, T)}{(\Delta\theta)_{\text{proj}}} \sqrt{\frac{2T}{\hbar c} K^3 P_{\text{arm}, 2\lambda}} \left( \frac{2\mathcal{F}/\pi}{\sqrt{1 + (f/f_p)^2}} \right)^2. \quad (\text{S116})$$

It is evident from Fig. S11 that, in the low frequency region  $f \ll f_A$ ,  $\mathcal{A} \gg 1$ , and

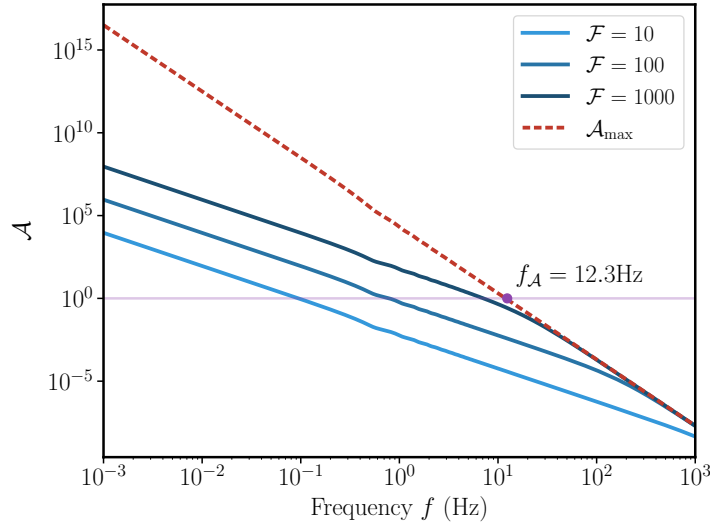


FIG. S11.  $\mathcal{A}(f, \mathcal{F})$  as a decreasing function of  $f$  and increasing function of  $\mathcal{F}$ . The critical frequency at which  $\mathcal{A}_{\text{max}} = 1$ , which is defined in Eq. (S118), is given by  $f_A = 12.3\text{Hz}$ . When  $f < f_A$ , the lower bound of the sum of radiation pressure of the  $2\lambda$ -laser and the quantum projection noise of atom equals to  $S_0(f)$ , as described by Eq. (S117).

the radiation pressure dominates the noise; while in the high frequency region  $f \gg f_A$ ,  $\mathcal{A} \ll 1$ , the quantum projection noise dominates.

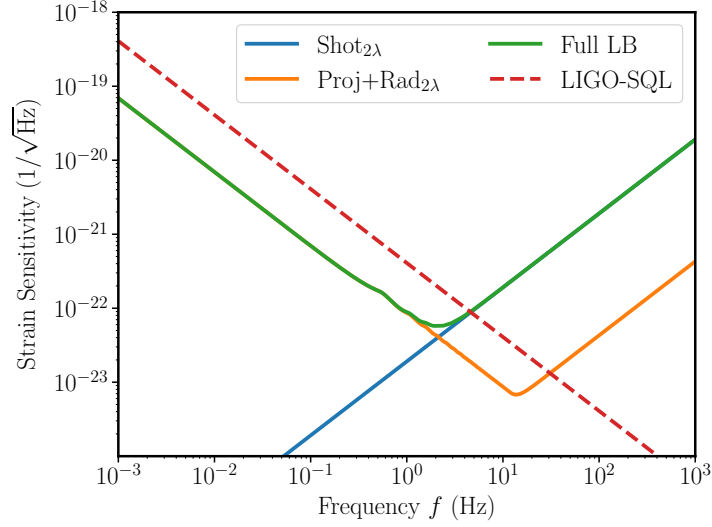


FIG. S12. Shot noise of the  $2\lambda$ -laser compared with the full lower bound. For frequencies in the regime  $f < f_c = 1.87\text{Hz}$ , the ratio  $S_{\text{shot},2\lambda}(f)/S_{\text{LB}}(f)$  is less than 1dB, and the full lower bound is well approximated by  $S_{\text{atom}} + S_{\text{rad},2\lambda}$ .

Since  $S_0(f)$  and  $S_{\text{shot},2\lambda}(f)$  are independent of  $\mathcal{F}$ , we optimize the strain sensitivity at each frequency by varying the finesse. The envelop of these optimized curves will be denoted as  $S_{\text{LB}}(f) = \min_{\mathcal{F}} S_n(f)$ , which has the expression:

$$S_{\text{LB}}(f) = \begin{cases} S_0(f) + S_{\text{shot},2\lambda}(f) & \text{if } f \leq f_A, \\ S_0(f) \frac{\mathcal{A}_{\text{max}}^{-1} + \mathcal{A}_{\text{max}}}{2} + S_{\text{shot},2\lambda}(f) & \text{if } f > f_A. \end{cases} \quad (\text{S117})$$

Here,  $f_A = 12.3\text{Hz}$  is the critical frequency at which  $\mathcal{A}_{\text{max}} = 1$ , where  $\mathcal{A}_{\text{max}}(f) = \max_{\mathcal{F}} \mathcal{A}(f, \mathcal{F})$  is plotted in Fig. S11 and its expression is given by:

$$\mathcal{A}_{\text{max}}(f) = \frac{4c^2}{ML^2(2\pi f)^4} \frac{\eta U_0 W(f, T)}{(\Delta\theta)_{\text{proj}}} \sqrt{\frac{2T}{\hbar c} K^3 P_{\text{arm},2\lambda}}. \quad (\text{S118})$$

As shown in Fig. S11 and Fig. S12, for  $f < f_c = 1.87\text{Hz}$ , the lower bound is well



approximately by  $S_{\text{LB}}(f) = S_0(f)$ , which takes a form of:

$$S_{\text{LB}}(f) = S_{\text{SQL}}(f) \frac{(\Delta\theta)_{\text{proj}}}{\eta U_0 W(f, T)} \sqrt{\frac{2\hbar P_{\text{arm}, 2\lambda}}{KcT}}. \quad (\text{S119})$$

Here,  $S_{\text{SQL}}(f) = 8\hbar/ML(2\pi f)^2$ , as defined in the main text, represents the SQL of a conventional interferometric GW detector with test mass  $M$  and arm length  $L$ .

To investigate the scaling relationship of  $S_{\text{LB}}(f)$  with atomic parameters, we observe that  $U_0 = \alpha_{2\lambda} I_U/2$ . Here,  $\alpha_{2\lambda}$  denotes the dynamic polarizability of atoms at the  $2\lambda$  wavelength, and  $I_U$  is the intensity of the  $2\lambda$ -laser used to generate  $U_{\text{lat}}$  in each Michelson arm. Assuming a laser waist radius of  $w = 50 \mu\text{m}$ , the power of the  $2\lambda$ -laser in each arm is calculated as  $P_{\text{arm}, 2\lambda} = \pi w^2 I_U/2$ . Consequently, the lower bound takes a form of:

$$S_{\text{LB}}(f) = S_{\text{SQL}}(f) \frac{(\Delta\theta)_{\text{proj}}}{\eta\sqrt{U_0 T}} \frac{1}{W(f, T)} \sqrt{\frac{2\pi\hbar w^2}{Kc\alpha_{2\lambda}}}, \quad (\text{S120})$$

which recovers Eq. (3) in the main text with  $C_{\text{atom}}$  given by:

$$C_{\text{atom}}(f, T) = \frac{1}{W(f, T)} \sqrt{\frac{2\pi\hbar w^2}{Kc\alpha_{2\lambda}}}. \quad (\text{S121})$$

For current experimental parameters, orbital squeezed states are crucial to ensure that  $C_{\text{atom}}(f, T)(\Delta\theta)_{\text{proj}}/\eta\sqrt{U_0 T} < 1$ . From Fig. S13, we can see that without orbital squeezing, the atomic sensor behaves worse than the SQL of a conventional sensor.

## C Influence of Atomic Species on Sensitivity

Our previous calculations assume an atomic sensor composed of  ${}^7\text{Li}$ . This section investigates how different atomic species affect sensor performance, mainly considering the following three aspects:

1. The signal lattice depth  $U_0$  would vary with different atoms. The projection noise  $S_{\text{atom}}^{1/2}(f)$  is inversely proportional to the signal lattice depth  $U_0$ , as indicated by Eq. (S112).

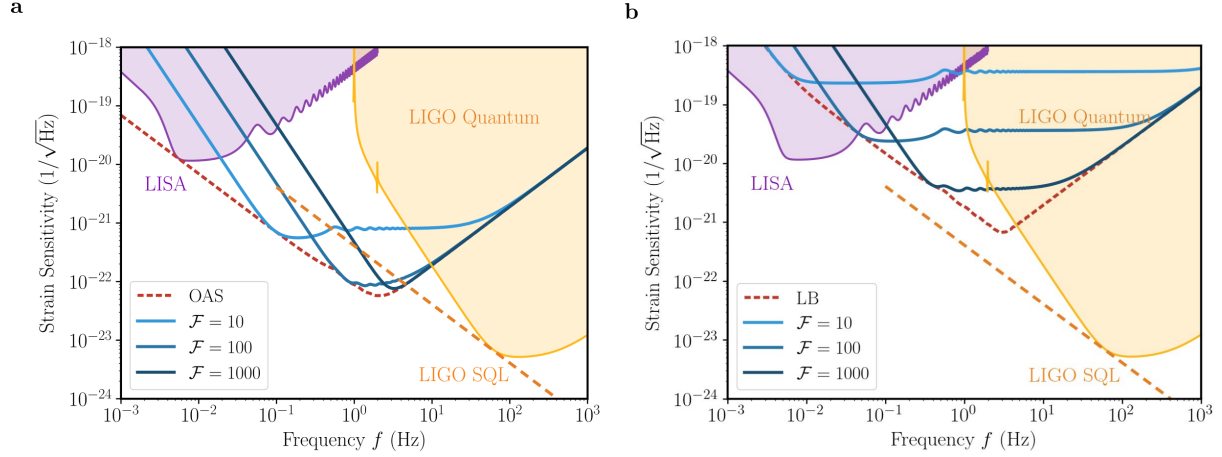


FIG. S13. Comparisons of squeezed orbital states and  $p$ -orbital condensed state. **a**: Orbital atomic sensor achieves a 8 dB improvement over LIGO's SQL if the initial state for detection is  $|\xi_R\rangle_{\text{atom}} \otimes |\text{vac}\rangle_{\text{photon}}$ . Here,  $|\xi_R\rangle_{\text{atom}}$  represents an orbital squeezed state of atoms with a squeezing parameter  $\xi_R$ , and  $|\text{vac}\rangle_{\text{photon}}$  denotes the vacuum dark port input state. **b**: Orbital atomic sensor behaves worse than LIGO's SQL if the initial state for detection is a orbital condensed state  $|p_x\rangle_{\text{atom}}^{\otimes N} \otimes |\text{vac}\rangle_{\text{photon}}$ .

However,  $U_0$  cannot be arbitrarily large for the experimental constraints in optical lattices. Specifically, the trap lattice depth  $V_0$  must be of the order of magnitude  $O(E_R)$  to maintain the stability of the  $p$ -orbital condensate. Moreover, the two-mode-approximation condition requires  $V_0 \gg U_0$ . For a consistent comparison, we set  $V_0 = 6E_R$  and  $U_0 = 0.1E_R$  for all atomic species. Given that  $E_R = \hbar^2 K^2 / 2m$  is inversely proportional to the atomic mass, a lighter atom such as  ${}^7\text{Li}$  results in reduced quantum projection noise, as illustrated in Figure S14d.

2. The laser power  $P_{\text{arm}}$  used to generated optical lattices vary with atoms. The radiation pressure noise  $S_{\text{rad}}^{1/2}(f)$  experienced by the test masses is proportional to the square root of the laser power  $P_{\text{arm}} = \pi w^2 U_0 / \alpha_{\text{atom}}$ , and thus depends on the atomic polarizability (as well as the lattice depths  $V_0$  and  $U_0$ ). For convenience, we list the polarizability of Li, Rb, Cs [69] as :  $\alpha_{\text{Li}}(532\text{nm}) = 284.36$  a.u.,  $\alpha_{\text{Li}}(1064\text{nm}) = 260.66$  a.u.,  $\alpha_{\text{Rb}}(532\text{nm}) = 258.78$  a.u.,  $\alpha_{\text{Rb}}(1064\text{nm}) = 722.37$  a.u.,  $\alpha_{\text{Cs}}(532\text{nm}) = 220.07$  a.u.,  $\alpha_{\text{Cs}}(1064\text{nm}) = 1372.9$  a.u., with the atom unit given by  $1 \text{ a.u.} = 1.6479 \times 10^{-41} \text{ Hz}/(\text{V}/\text{m})^2$ .

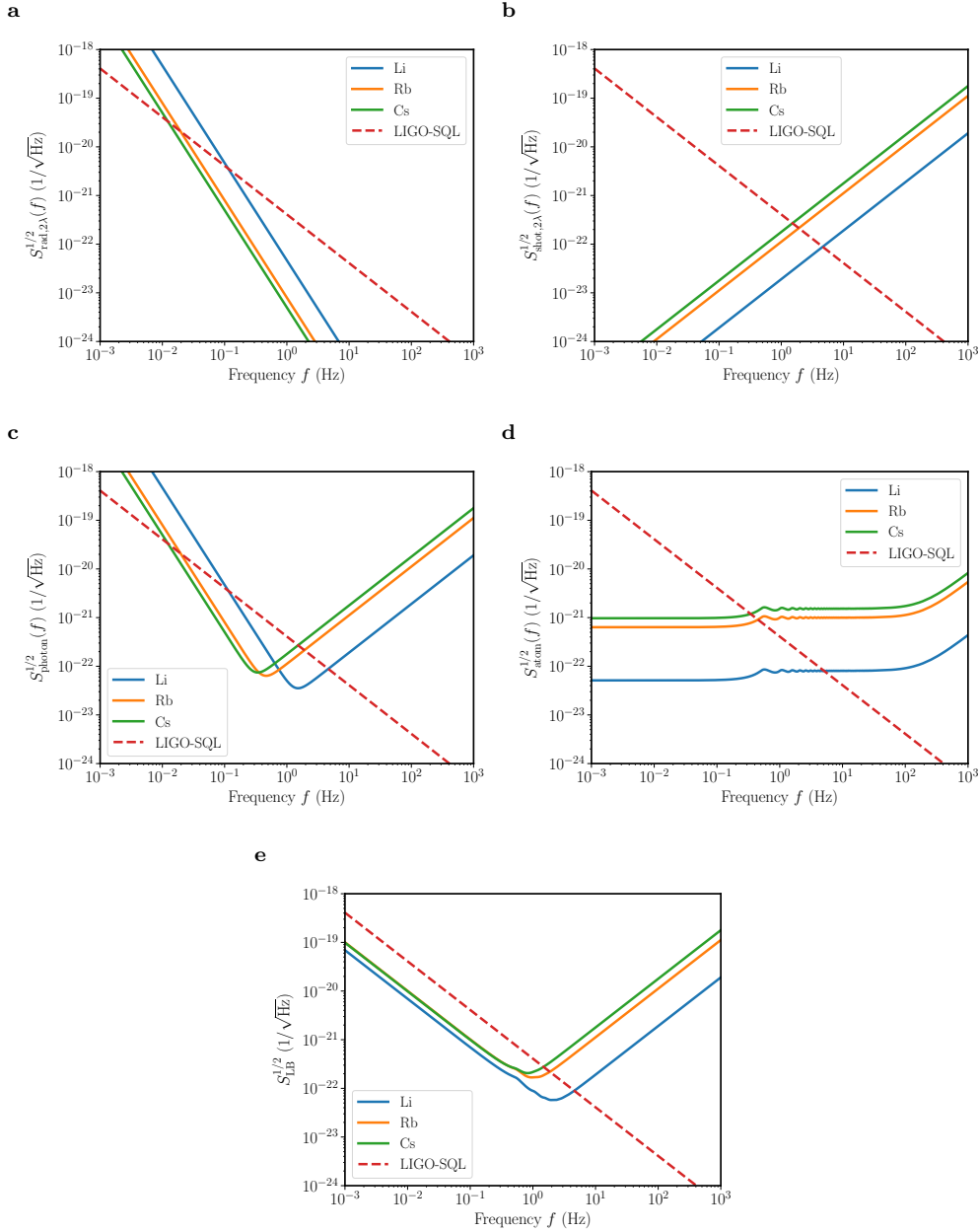


FIG. S14. Detection sensitivity with different atomic species such as  ${}^7\text{Li}$ ,  ${}^{87}\text{Rb}$  and  ${}^{133}\text{Cs}$ . **a:** Radiation pressure noise of the  $2\lambda$ -laser in Eq. (S104) with  $\mathcal{F} = 100$ , **b:** Shot noise of the  $2\lambda$ -laser in Eq. (S103) with  $\mathcal{F} = 100$ , **c:** Full photon noise in Eq. (S102) with  $\mathcal{F} = 100$ , **d:** Quantum projection noise of atoms in Eq. (S112) with  $\mathcal{F} = 100$ , **e:** Full lower bound of the strain sensitivity in Eq. (S117).  ${}^7\text{Li}$  performs the best near 1Hz because that  $S_{\text{LB}}$  scales as the recoil energy as  $E_R^{-1/2}$  in this regime and  ${}^7\text{Li}$  has the largest recoil energy among the alkali metal atoms.

3. The interaction control largely depends on atoms: The interaction between  ${}^7\text{Li}$  atoms is more manageable and experimentally accessible compared to other alkali atoms. Specifically, the preparation of cold atomic  $p$ -orbital squeezing begins with a weakly interacting BEC in the excited band of a bipartite optical lattice [18, 22, 24]. Squeezing in the  $p$ -orbital is achieved by an interaction quench, where the interaction strength is abruptly increased. This is accessible to the current cold atom technology using Feshbach resonances. For instance, in  ${}^7\text{Li}$  atoms, a broad Feshbach resonance is present at approximately 737 G [43, 44]. The initial  $p$ -orbital BEC is formed with the weakly interacting state  $|F = 1, m_F = -1\rangle$ . The interaction quench is realized by driving a Raman transition that converts the atomic internal state to  $|F = 1, m_F = 1\rangle$ , which exhibits strongly repulsive interactions.

As shown in Figure S14e,  ${}^7\text{Li}$  exhibits the highest sensitivity, considering the feasible parameters in atomic optical lattice experiments. We expect  ${}^7\text{Li}$  to be the optimal choice for the atomic species in our orbital atomic sensor.

## D Sky- and Polarization-averaging

This section addresses the pattern function and angular sensitivity of our atomic sensor. In the above calculations of sensitivity curves, a plus-polarized gravitational wave propagating along  $\mathbf{e}_z$  direction is assumed. Now consider a generic gravitational wave  $h_{ij}(t) = h_+(t)\mathbf{e}_{ij}^+ + h_\times(t)\mathbf{e}_{ij}^\times$  propagating along  $\mathbf{e}_n = (\theta, \phi)$  direction, where  $\mathbf{e}_{ij}^{+, \times}$  are the polarization tensors of  $+$ ,  $\times$  polarization, and  $(\theta, \phi)$  the sky-angles. The GW-induced phase shifts in the X, Y arms are generalized from Eq. (S35) and Eq. (S36) to [64]:

$$\Delta\Phi_X = \frac{1}{2}\mathcal{T}_\Phi h_{XX} = \frac{1}{2}\mathcal{T}_\Phi \left[ h_+ (\cos^2\theta \cos^2\phi - \sin^2\phi) + h_\times \cos\theta \sin(2\phi) \right], \quad (\text{S122})$$

$$\Delta\Phi_Y = \frac{1}{2}\mathcal{T}_\Phi h_{YY} = \frac{1}{2}\mathcal{T}_\Phi \left[ h_+ (\cos^2\theta \sin^2\phi - \cos^2\phi) - h_\times \cos\theta \sin(2\phi) \right], \quad (\text{S123})$$

where the expressions for  $h_{XX}$  and  $h_{YY}$  incorporate the directional dependence of the GW. Consequently, the GW-induced pseudo-magnetic field, previously given by Eq. (S29), must be revised. Notably, in a general scenario where  $\Phi_{x,y}$  are not set to 0 or  $\pi$ , the pseudo-magnetic field  $B_x$  can be non-zero even in the absence of a GW. The additional pseudo-magnetic field  $\Delta B_x$  induced by the GW is:

$$\Delta B_x = \frac{\partial B_x}{\partial \Phi_x} \Delta \Phi_x + \frac{\partial B_x}{\partial \Phi_y} \Delta \Phi_y = \frac{1}{2} \eta(V_0, \phi) U_0 \mathcal{T}_\Phi(f) (\sin \Phi_X h_{XX} - \sin \Phi_Y h_{YY}), \quad (\text{S124})$$

where  $\Phi_{X,Y}$  are the phase accumulations in X, Y arms and relates to the phases  $\Phi_{x,y}$  in Eq. (S26) by  $\Phi_X = \Phi_x - \Phi_y$  and  $\Phi_Y = \Phi_x + \Phi_y$ . The input GW signal is derived by comparing Eq. (S29) and Eq. (S124):

$$h(t) = \frac{1}{2} (\sin \Phi_X h_{XX} - \sin \Phi_Y h_{YY}) = h_+(t) F_+(\theta, \phi; \psi = 0) + h_\times(t) F_\times(\theta, \phi; \psi = 0). \quad (\text{S125})$$

Here,  $F_{+,\times}$  are the pattern function of our atomic sensor, and  $\psi$  is the polarization angle, indicating the orientation of the X, Y axes relative to the axis to whom GW polarization is defined. The pattern functions are then given by:

$$F_+(\theta, \phi; 0) = \frac{1}{2} \left[ (\cos^2 \theta \cos^2 \phi - \sin^2 \phi) \sin \Phi_X - (\cos^2 \theta \sin^2 \phi - \cos^2 \phi) \sin \Phi_Y \right], \quad (\text{S126})$$

$$F_\times(\theta, \phi; 0) = \cos \theta \sin \phi \cos \phi (\sin \Phi_X + \sin \Phi_Y), \quad (\text{S127})$$

$$F_+(\theta, \phi; \psi) = F_+(\theta, \phi; 0) \cos 2\psi - F_\times(\theta, \phi; 0) \sin 2\psi, \quad (\text{S128})$$

$$F_\times(\theta, \phi; \psi) = F_+(\theta, \phi; 0) \sin 2\psi + F_\times(\theta, \phi; 0) \cos 2\psi. \quad (\text{S129})$$

These pattern functions describe how our atomic sensor response to GWs with different propagating direction and polarizations. The sky- and polarization- averaged signal response function is further defined as the average of pattern functions, and have the

expressions [10, 64]:

$$\begin{aligned}\mathcal{R}(f) &= \langle |F_+|^2 \rangle = \langle |F_\times|^2 \rangle = \frac{1}{8\pi^2} \int_0^\pi \sin\theta d\theta \int_0^{2\pi} d\phi \int_0^{2\pi} d\psi |F_+(\theta, \phi; \psi)|^2, \\ &= \frac{1}{15} (\sin^2\Phi_X + \sin\Phi_X \sin\Phi_Y + \sin^2\Phi_Y) \leq \frac{1}{5}.\end{aligned}\tag{S130}$$

The maximum response is achieved when  $\Phi_X = \Phi_Y = \pi/2$ , or equivalently  $\Phi_x = \pi/2, \Phi_y = 0$  (up to  $\pi$  phases), which also maximize the pseudo-magnetic field induced by a plus-polarized GW (see Eq. (S29)). It is also remarking that under these parameters, there is no pseudo-magnetic field in the flat spacetime. The sky- and polarization- averaged sensitivity is obtained as [10]:

$$S_n^{\text{avg}}(f) = \frac{S_n(f)}{\mathcal{R}(f)} = 5S_n(f) \quad (\text{when } \Phi_x = \pi/2, \Phi_y = 0)\tag{S131}$$

All the sensitivity curves plotted in figures of the main text or Supplementary Information represent the sky- and polarization- averaged sensitivity.

## S-5 Detecting Dark Photon Dark Matter

Interferometric gravitational-wave detectors, such as LIGO, are known to be sensitive to Dark Photon Dark Matter (DPDM) [6, 39–41]. Our orbital atomic sensor thus also provides a sensitive probe for DPDM. This section explores the mechanisms by which our atomic sensor detects DPDM signals and the derivation of the upper bound of the coupling constant between DPDM and normal matter.

### A Dark Photon Electrodynamics

This section examines the fundamental properties of DPDM, mainly following Refs. [70–72]. The dark photon is a spin-1 gauge boson beyond the standard model, as a potential

ultralight candidate for dark matter. Unlike heavier candidates like Weakly Interacting Massive Particles (WIMPs), the ultralight dark photon is characterized by its classical, wave-like nature due to its high phase space density  $n_{\text{phase}}$ , given by:

$$n_{\text{phase}} = \frac{\rho_{\text{DM}}}{m_A c^2} \lambda_A^3 \simeq 10^6 \left( \frac{1\text{eV}/c^2}{m_A} \right)^4, \quad (\text{S132})$$

where  $\lambda_A = 2\pi\hbar/(m_A v_{\text{DM}})$  and  $m_A$  are the de Broglie wavelength and mass of the dark photon, respectively. The virial velocity  $v_{\text{DM}}$  and local energy density  $\rho_{\text{DM}}$  of dark matter are observed to be  $v_{\text{DM}} = 230\text{km/s}$  and  $\rho_{\text{DM}} = 0.4\text{GeV}/\text{cm}^3$  [70], respectively. For  $m_A \lesssim 0.1\text{eV}/c^2$ ,  $n_{\text{phase}} \gg 1$ , allowing the dark photon field to be treated as a classical condensate wave, whose spatial components are expressed as:

$$\mathbf{A}(t, \mathbf{x}) = \mathbf{A}_0 \cos(\omega t - \mathbf{k} \cdot \mathbf{x} + \phi_A), \quad (\text{S133})$$

where  $\mu_0$  is the magnetic permeability in the vacuum,  $\mathbf{A}_0, \omega, \mathbf{k}$  is the polarization vector, angular frequency and wave vector of the dark photon field, and  $\phi_A$  is its random phase. The magnitude of  $\mathbf{A}_0$  is determined by the local density by  $|\mathbf{A}_0| = \frac{1}{\omega} \sqrt{\frac{2\rho_{\text{DM}}}{\epsilon_0}}$ . The dispersion relation of dark photon is  $\hbar\omega = \sqrt{(\hbar kc)^2 + (m_A c^2)^2} \simeq m_A c^2 + \frac{1}{2} m_A v_{\text{DM}}^2$ , which leads to the frequency variation of the signal  $\Delta f = \frac{1}{2} \left( \frac{v_{\text{DM}}}{c} \right)^2 f$ , where the frequency of dark photon relates to its mass by  $f = \frac{m_A c^2}{2\pi\hbar}$ . This further results in the coherence time of the dark matter  $T_{\text{coh}}$  given by:

$$T_{\text{coh}}(f) = \frac{1}{\Delta f} = \frac{2}{f} \left( \frac{c}{v_{\text{DM}}} \right)^2. \quad (\text{S134})$$

In the Lorentz gauge  $\partial_\mu A^\mu = 0$ , the temporal component of  $A^\mu$  is of magnitude  $\frac{v_{\text{DM}}}{c} |\mathbf{A}_0|$ , which is negligible in calculating the dark electric field  $\mathbf{E}$ . The dark electric and magnetic

fields generated by the dark photon are described by:

$$\mathbf{E}(t, \mathbf{x}) \simeq -\partial_t \mathbf{A} = \omega \mathbf{A}_0 \sin(\omega t - \mathbf{k} \cdot \mathbf{x} + \phi_A), \quad (\text{S135})$$

$$\mathbf{B}(t, \mathbf{x}) = \nabla \times \mathbf{A} = \mathbf{k} \times \mathbf{A}_0 \sin(\omega t - \mathbf{k} \cdot \mathbf{x} + \phi_A). \quad (\text{S136})$$

The ratio of the dark magnetic field to the dark electric field is  $\frac{|\mathbf{B}|}{|\mathbf{E}|} = \frac{v_{\text{DM}}}{c^2} \simeq 10^{-3}/c$ , suggesting that the dark magnetic field is negligible in the interaction between dark photons and ordinary matter. The magnitude of  $\mathbf{E}_0$  is given by  $|\mathbf{E}_0| = \omega |\mathbf{A}_0| = \sqrt{\frac{2\rho_{\text{DM}}}{\epsilon_0}} = 3.80 \times 10^3 \text{kg} \cdot \text{m}/(\text{C} \cdot \text{s}^2)$ .

## B Coupling between DPDM and the Atomic Sensor

The dark photon is expected to couple to conserved currents in the standard model. The Lagrangian describing the coupling of  $A^\mu$  to current  $J_{\text{D}}^\mu$  (D = B-L for baryon-lepton and D = B for baryon) is given by:

$$\mathcal{L} = -\frac{1}{4\mu_0} F^{\mu\nu} F_{\mu\nu} + \frac{1}{2\mu_0} \left(\frac{m_{AC}}{\hbar}\right)^2 A^\mu A_\mu - e g_{\text{D}} J_{\text{D}}^\mu A_\mu, \quad (\text{S137})$$

where  $\mu_0$  is the vacuum magnetic permeability,  $F_{\mu\nu} = \partial_\mu A_\nu - \partial_\nu A_\mu$  is the dark photon field strength tensor, and  $g_{\text{D}}$  is the  $U(1)_{\text{D}}$  coupling constant normalized to the electromagnetic coupling constant  $e$ . As a consequence, dark photon exerts force  $\mathbf{F}$  on ordinary matter, as described by:

$$\mathbf{F}(t, \mathbf{x}) = e g_{\text{D}} q_{\text{D}} \mathbf{E}(t, \mathbf{x}) \quad (\text{S138})$$

In this equation,  $q_{\text{D}}$  denotes the  $U(1)_{\text{D}}$  charge of the test masses, with  $q_{\text{B}}$  being the sum of the number of protons and neutrons, and  $q_{\text{B-L}}$  being the number of neutrons.

We now analyze the interaction between DPDM and our complete atomic sensor, which mainly involves two parts: the coupling between DPDM and atoms, and the coupling



between DPDM and test masses.

## 1 Coupling between DPDM and Atoms

As detailed in [S-4 C](#), the atomic sensor is most sensitive when composed of  ${}^7\text{Li}$ . This section focuses on the interaction between DPDM and  ${}^7\text{Li}$  atoms. A single  ${}^7\text{Li}$  atom contains 3 protons and 4 neutrons (along with 3 electrons). Consequently, the dark photon exerts a force on a single  ${}^7\text{Li}$  atom, the magnitude of which is given by:

$$F_{\text{DM}} = 4eg_{\text{B-L}}|\mathbf{E}_0| = 2.43 \times 10^{-39} \left( \frac{g_{\text{B-L}}}{10^{-24}} \right) \text{ kg} \cdot \text{m/s}^2. \quad (\text{S139})$$

The potential energy induced by the dark photon force is typically of the order:

$$V_{\text{DM}} = F_{\text{DM}}a = 9.17 \times 10^{-46} \left( \frac{g_{\text{B-L}}}{10^{-24}} \right) \text{ kg} \cdot \text{m}^2/\text{s}^2 = 1.38 \times 10^{-17} \left( \frac{g_{\text{B-L}}}{10^{-24}} \right) E_R, \quad (\text{S140})$$

where  $a = \lambda/\sqrt{2}$  is the lattice constant of the trap potential (see [S-1 A](#)) and  $E_R = h^2/2m\lambda^2$  is the photon recoil energy of  ${}^7\text{Li}$ , with  $m$  being its mass. Considering the constraints from the Eöt-Wash experiment [[11](#), [12](#)] and the MICROSCOPE experiment [[13–16](#)], which have excluded dark photon signals with  $g_{\text{B-L}} \geq 10^{-24}$  for  $m_A < 10^{-13} \text{eV}/c^2$ , the dark photon-induced potential therefore satisfies  $V_{\text{DM}} \leq 10^{-16} E_R$  is considered negligible.

## 2 Coupling between DPDM and Test Masses

For our interferometric setup, the dark photon is coupled to the four test masses (two ITMs and two ETMs, see [Fig. 1](#) in the main text). This interaction results in a time-varying acceleration and oscillation of the test masses, described by:

$$\mathbf{a}(t) = eg_{\text{D}} \frac{q_{\text{D}}}{M} \omega \mathbf{A}_0 \sin(\omega t - \mathbf{k} \cdot \mathbf{x} + \phi_A), \quad (\text{S141})$$

$$\delta \mathbf{x}(t) = -eg_{\text{D}} \frac{q_{\text{D}}}{M} \frac{\mathbf{A}_0}{\omega} \sin(\omega t - \mathbf{k} \cdot \mathbf{x} + \phi_A). \quad (\text{S142})$$

For silica test masses, similar to those in LIGO, the charge-to-mass ratios are  $q_B/M = 5.61 \times 10^{26} \text{ kg}^{-1}$  and  $q_{B-L}/M = 2.80 \times 10^{26} \text{ kg}^{-1}$  [6]. The B – L coupling induces oscillations on the order of  $|\delta\mathbf{x}_0|$ , calculated as:

$$|\delta\mathbf{x}_0| = e g_{B-L} \frac{q_{B-L}}{M} \frac{\mathbf{A}_0}{\omega} = 4.32 \times 10^{-15} \left( \frac{1\text{Hz}}{f} \right)^2 \left( \frac{g_{B-L}}{10^{-24}} \right) \text{ m}. \quad (\text{S143})$$

Such oscillations result in a non-zero phase accumulation  $\Phi_{X,Y}$  of lasers in the X, Y arms. Given that our orbital atomic sensor is capable of detecting displacements  $\delta\mathbf{x}$  of the order of  $h_{0,+}L \simeq 10^{-23} \times 4\text{km} \simeq 10^{-20}\text{m}$ , it is expected to be sensitive to dark photon-induced oscillation signals near  $f = 1\text{Hz}$  for  $g_{B-L} \lesssim 10^{-24}$ , assuming their existence. The effective gravitational wave signal  $h_{\text{eff}}(t)$  due to  $\delta\mathbf{x}(t)$  is given by [41]:

$$h_{\text{eff}}(t) = h_1(t) + h_2(t), \quad (\text{S144})$$

$$h_1(t) = \frac{e g_D}{\pi f L} \frac{q_D}{M} \sin^2(\pi f L/c) \times (\mathbf{n} - \mathbf{m}) \cdot \mathbf{A}_0 \sin \phi(t), \quad (\text{S145})$$

$$h_2(t) = -\frac{e g_D}{c^2} \frac{q_D}{M} \times \left[ (\mathbf{n} \cdot \mathbf{A}_0) (\mathbf{n} \cdot \mathbf{v}_{\text{DM}}) - (\mathbf{m} \cdot \mathbf{A}_0) (\mathbf{m} \cdot \mathbf{v}_{\text{DM}}) \right] \cos \phi(t), \quad (\text{S146})$$

where  $\mathbf{n}, \mathbf{m}$  are unit vectors along the interferometer arms, and  $\phi(t) = \omega(t - L/c) + \phi_A$ . The term  $h_1(t)$  accounts for the light travel time delay, while  $h_2(t)$  results from the phase difference experienced by the test masses. The phase difference is estimated to be  $\mathbf{k} \cdot \Delta\mathbf{x} \simeq 6.14 \times 10^{-8} f/\text{Hz}$ , which is minute for LIGO but significant for longer interferometers like LISA (see Fig. 2b of the main text). The total effective strain, considering no interference between  $h_1(t)$  and  $h_2(t)$  after time averaging, is:

$$\langle h_{\text{eff}}^2 \rangle = \langle h_1^2 \rangle + \langle h_2^2 \rangle, \quad (\text{S147})$$

$$\langle h_1^2 \rangle = \frac{e^2 g_D^2 \rho_{\text{DM}}}{6\pi^4 f^4 L^2 \epsilon_0} \left( \frac{q_D}{M} \right)^2 \sin^4(\pi f L/c) \times (1 - \mathbf{n} \cdot \mathbf{m}), \quad (\text{S148})$$

$$\langle h_2^2 \rangle = \frac{e^2 g_D^2 \rho_{\text{DM}}}{18\pi^2 f^2 c^4 \epsilon_0} (1 - (\mathbf{n} \cdot \mathbf{m})^2). \quad (\text{S149})$$

In this context, the notation  $\langle \dots \rangle$  represents an average over time, as well as averaging across the propagation direction and polarization states of the dark photon. The geometry factor  $\mathbf{n} \cdot \mathbf{m}$  is given by  $\mathbf{n} \cdot \mathbf{m} = 0$  for LIGO (as well as our sensor) and  $\mathbf{n} \cdot \mathbf{m} = 1/2$  for LISA.

## C $1\sigma$ Upper Limits of $g_D$

This section evaluates the detection threshold for dark photon dark matter using our atomic sensor. Employing a semi-coherent method [41, 71], data are segmented into intervals of duration  $T_{\text{coh}}$ . The  $1\sigma$  detection upper limit for  $g_D$  is derived as:

$$\langle h_{\text{eff}}^2 \rangle (g_D) = \frac{S_n(f)}{T_{\text{eff}}(f)}, \quad (\text{S150})$$

where  $\langle h_{\text{eff}}^2 \rangle$  represents the effective strain of dark photons,  $S_n(f)$  is the full strain sensitivity of our atomic sensor, and  $T_{\text{eff}}(f)$  is the effective observation time, defined by:

$$T_{\text{eff}}(f) = \begin{cases} T_{\text{obs}} & \text{if } T_{\text{obs}} > T_{\text{coh}} \\ \sqrt{T_{\text{obs}} T_{\text{coh}}(f)} & \text{if } T_{\text{obs}} \leq T_{\text{coh}} \end{cases}, \quad (\text{S151})$$

Here,  $T_{\text{obs}}$  denotes the total observation time and  $T_{\text{coh}}$  the coherence time of dark photon dark matter given by Eq. (S134). The  $1\sigma$  detection upper limit for  $g_B$  and  $g_{B-L}$  of our orbital atomic sensor is shown in Fig. S15.

For generating Fig. 2b in the main text, we apply Eq. (S150) to translate the strain sensitivity of gravitational waves from LISA [10], LIGO [9], and our atomic sensor into the corresponding detection upper limit for  $g_D$ . We assume a total observation time of  $T_{\text{obs}} = 2$  y.r. for the calculations. The parameters of our orbital atomic sensor is summarized in Table S1.

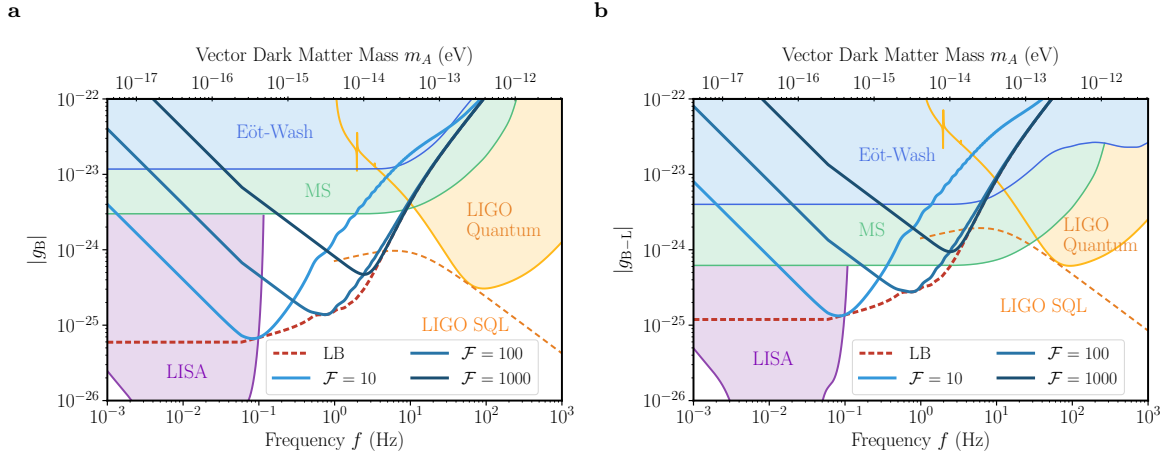


FIG. S15.  $1\sigma$  detection upper limit of dark matter by the orbital atomic sensor. **a**, Upper limit of the dark photon/baryon coupling  $|g_B|$ ; **b**, Upper limit of the dark photon/baryon coupling  $|g_{B-L}|$ . For comparison, we show the limits of LIGO [6], LISA [10], Eöt-Wash [11, 12], and MICROSCOPE (MS) experiments [13–16].

## S-6 Parameters of the Orbital Atomic Sensor

Table S1 presents the proposed parameters for our orbital atomic sensor, which are used to generate Fig. 2 in the main text.

Parameter	Units	Value
Arms length $L$	km	4
Mirror mass $M$	kg	40
FP cavity finesse $\mathcal{F}$		$1 \sim 10^4$
Primary laser power $P_{\text{arm},\lambda}$	W	1.77
Signal laser power $P_{\text{arm},2\lambda}$	mW	32.2
Atomic parameters		
Atom numbers $N$		$8 \times 10^5$
Atom species		${}^7\text{Li}$
$p$ orbital states lifetime $T_{\text{life}}$	s	1
Optical Lattice parameters		
Primary Laser wavelength $\lambda$	nm	532
Primary lattice depth $V_0$	$E_R$	6
Signal lattice depth $U_0$	$E_R$	0.1
Efficiency $\eta$		0.6

TABLE S1. List of parameters

- 
- [1] N. Yunes, M. C. Miller, and K. Yagi, *Nature Reviews Physics* **4**, 237 (2022).
  - [2] M. R. Mosbech, A. C. Jenkins, S. Bose, C. Boehm, M. Sakellariadou, and Y. Y. Y. Wong, *Phys. Rev. D* **108**, 043512 (2023).
  - [3] G. Bertone and T. M. P. Tait, *Nature* **562**, 51 (2018).
  - [4] G. Bertone, *Nuclear Physics B* **1003**, 116487 (2024), special Issue of Nobel Symposium 182 on Dark Matter.
  - [5] S. M. Vermeulen, P. Relton, and Others, *Nature* **600**, 424 (2021).
  - [6] R. Abbott et al. (LIGO Scientific Collaboration, Virgo Collaboration, and KAGRA Collaboration), *Phys. Rev. D* **105**, 063030 (2022).
  - [7] A. G. Abac, R. Abbott, H. Abe, and Others (LIGO Scientific, Virgo, and KAGRA Collaborations), *Phys. Rev. D* **110**, 042001 (2024).
  - [8] Y. Cui, P. Saha, and E. I. Sfakianakis, *Phys. Rev. Lett.* **133**, 021004 (2024).
  - [9] J. Aasi, B. P. Abbott, and R. Abbott, *Classical and Quantum Gravity* **32**, 074001 (2015).
  - [10] T. Robson, N. J. Cornish, and C. Liu, *Classical and Quantum Gravity* **36**, 105011 (2019).
  - [11] S. Schlamminger, K.-Y. Choi, T. A. Wagner, J. H. Gundlach, and E. G. Adelberger, *Phys. Rev. Lett.* **100**, 041101 (2008).
  - [12] T. A. Wagner, S. Schlamminger, J. H. Gundlach, and E. G. Adelberger, *Classical and Quantum Gravity* **29**, 184002 (2012).
  - [13] P. Touboul, G. Métris, and M. e. a. Rodrigues, *Phys. Rev. Lett.* **119**, 231101 (2017).
  - [14] J. Bergé, P. Brax, G. Métris, M. Pernot-Borràs, P. Touboul, and J.-P. Uzan, *Phys. Rev. Lett.* **120**, 141101 (2018).
  - [15] P. Fayet, *Phys. Rev. D* **97**, 055039 (2018).
  - [16] P. Touboul, G. Métris, M. Rodrigues, and Others (MICROSCOPE Collaboration), *Phys. Rev. Lett.* **129**, 121102 (2022).
  - [17] L. Pezzè, A. Smerzi, M. K. Oberthaler, R. Schmied, and P. Treutlein, *Rev. Mod. Phys.* **90**, 035005 (2018).
  - [18] G. Wirth, M. Ölschläger, and A. Hemmerich, *Nature Physics* **7**, 147 (2011).
  - [19] M. Lewenstein and W. V. Liu, *Nature Physics* **7**, 101 (2011).
  - [20] X. Li and W. V. Liu, *Reports on Progress in Physics* **79**, 116401 (2016).
  - [21] M. Mamaev, J. H. Thywissen, and A. M. Rey, *Advanced Quantum Technologies* **3**, 1900132 (2020).
  - [22] S. Jin, W. Zhang, X. Guo, X. Chen, X. Zhou, and X. Li, *Phys. Rev. Lett.* **126**, 035301 (2021).
  - [23] H. Shui, S. Jin, Z. Li, F. Wei, X. Chen, X. Li, and X. Zhou, *Phys. Rev. A* **104**, L060601 (2021).
  - [24] X.-Q. Wang, G.-Q. Luo, J.-Y. Liu, W. V. Liu, A. Hemmerich, and Z.-F. Xu, *Nature* **596**, 227 (2021).
  - [25] V. Venu, P. Xu, M. Mamaev, F. Corapi, T. Bilitewski, J. P. D’Incao, C. J. Fujiwara, A. M. Rey, and J. H. Thywissen, *Nature* **613**, 262 (2023).
  - [26] J. Ma, X. Wang, C.-P. Sun, and F. Nori, *Physics Reports* **509**, 89 (2011).
  - [27] T. Hernández Yanes, M. Płodzień, M. Mackoīt Sinkevičienė, G. Žlabys, G. Juzeliūnas, and E. Witkowska, *Phys. Rev. Lett.* **129**, 090403 (2022).
  - [28] C. Luo, H. Zhang, A. Chu, C. Maruko, A. M. Rey, and J. K. Thompson, *Hamiltonian engineering of collective xyz spin models in an optical cavity* (2024).
  - [29] T. Kock, C. Hippler, A. Ewerbeck, and A. Hemmerich, *Journal of Physics B: Atomic, Molecular and Optical Physics* **49**, 042001 (2016).
  - [30] D. S. Hall, M. R. Matthews, J. R. Ensher, C. E. Wieman, and E. A. Cornell, *Phys. Rev. Lett.* **81**, 1539 (1998).
  - [31] D. S. Hall, M. R. Matthews, C. E. Wieman, and E. A. Cornell, *Phys. Rev. Lett.* **81**, 1543 (1998).
  - [32] Y. Shin, M. Saba, T. A. Pasquini, W. Ketterle, D. E. Pritchard, and A. E. Leanhardt, *Phys. Rev. Lett.* **92**, 050405 (2004).
  - [33] T. Schumm, S. Hofferberth, L. M. Andersson, S. Wildermuth, S. Groth, I. Bar-Joseph, J. Schmiedmayer, and P. Krüger, *Nature physics* **1**, 57 (2005).
  - [34] A. J. Leggett, *Reviews of modern physics* **73**, 307 (2001).
  - [35] B. Dalton and S. Ghanbari, *Journal of Modern Optics* **59**, 287 (2012).
  - [36] C. L. Degen, F. Reinhard, and P. Cappellaro, *Rev. Mod. Phys.* **89**, 035002 (2017).
  - [37] D. J. Wineland, J. J. Bollinger, W. M. Itano, F. L. Moore, and D. J. Heinzen, *Phys. Rev. A* **46**, R6797 (1992).
  - [38] D. J. Wineland, J. J. Bollinger, W. M. Itano, and D. J. Heinzen, *Phys. Rev. A* **50**, 67 (1994).
  - [39] A. Pierce, K. Riles, and Y. Zhao, *Phys. Rev. Lett.* **121**, 061102 (2018).

- [40] Y. Michimura, T. Fujita, S. Morisaki, H. Nakatsuka, and I. Obata, *Phys. Rev. D* **102**, 102001 (2020).
- [41] S. Morisaki, T. Fujita, Y. Michimura, H. Nakatsuka, and I. Obata, *Phys. Rev. D* **103**, L051702 (2021).
- [42] M. Pitkin, S. Reid, S. Rowan, and J. Hough, *Living reviews in relativity* **14**, 1 (2011).
- [43] S. E. Pollack, D. Dries, M. Junker, Y. P. Chen, T. A. Corcovilos, and R. G. Hulet, *Phys. Rev. Lett.* **102**, 090402 (2009).
- [44] R. G. Hulet, J. H. V. Nguyen, and R. Senaratne, *Review of Scientific Instruments* **91**, 011101 (2020).
- [45] J. Aasi, J. Abadie, B. Abbott, R. Abbott, T. Abbott, M. Abernathy, C. Adams, T. Adams, P. Addesso, R. Adhikari, *et al.*, *Nature Photonics* **7**, 613 (2013).
- [46] Y. Ma, H. Miao, B. H. Pang, M. Evans, C. Zhao, J. Harms, R. Schnabel, and Y. Chen, *Nature Physics* **13**, 776 (2017).
- [47] D. Ganapathy, W. Jia, M. Nakano, and Others (LIGO O4 Detector Collaboration), *Phys. Rev. X* **13**, 041021 (2023).
- [48] W. Jia, V. Xu, K. Kuns, and Others, *Science* **385**, 1318 (2024).
- [49] S. Kotler, N. Akerman, Y. Glickman, A. Keselman, and R. Ozeri, *Nature* **473**, 61 (2011).
- [50] G. Wang, Y.-X. Liu, J. M. Schloss, S. T. Alsid, D. A. Braje, and P. Cappellaro, *Phys. Rev. X* **12**, 021061 (2022).
- [51] S. Chen, M. Zhuang, R. Fang, Y. Chen, C. Han, B. Lu, J. Huang, and C. Lee, *Communications Physics* **7**, 189 (2024).
- [52] T. Müller, S. Fölling, A. Widera, and I. Bloch, *Phys. Rev. Lett.* **99**, 200405 (2007).
- [53] L. Niu, S. Jin, X. Chen, X. Li, and X. Zhou, *Phys. Rev. Lett.* **121**, 265301 (2018).
- [54] M. Hachmann, Y. Kiefer, J. Riebeschl, R. Eichberger, and A. Hemmerich, *Phys. Rev. Lett.* **127**, 033201 (2021).
- [55] J. Vargas, M. Nuske, R. Eichberger, C. Hippler, L. Mathey, and A. Hemmerich, *Phys. Rev. Lett.* **126**, 200402 (2021).
- [56] A. Isacsson and S. M. Girvin, *Phys. Rev. A* **72**, 053604 (2005).
- [57] A. B. Kuklov, *Phys. Rev. Lett.* **97**, 110405 (2006).
- [58] W. V. Liu and C. Wu, *Phys. Rev. A* **74**, 013607 (2006).
- [59] L. S. Collaboration, *Nature Physics* **7**, 962 (2011).
- [60] J. Ma and X. Wang, *Phys. Rev. A* **80**, 012318 (2009).
- [61] H. Lipkin, N. Meshkov, and A. Glick, *Nuclear Physics* **62**, 188 (1965).
- [62] M. Kitagawa and M. Ueda, *Phys. Rev. A* **47**, 5138 (1993).
- [63] Z. Cai and C. Wu, *Phys. Rev. A* **84**, 033635 (2011).
- [64] M. Maggiore, *Gravitational Waves. Vol. 1: Theory and Experiments* (Oxford University Press, 2007).
- [65] V. Mukhanov and S. Winitzki, *Introduction to quantum effects in gravity* (Cambridge university press, 2007).
- [66] J. M. Taylor, P. Cappellaro, L. Childress, L. Jiang, D. Budker, P. Hemmer, A. Yacoby, R. Walsworth, and M. Lukin, *Nature Physics* **4**, 810 (2008).
- [67] H. J. Kimble, Y. Levin, A. B. Matsko, K. S. Thorne, and S. P. Vyatchanin, *Phys. Rev. D* **65**, 022002 (2001).
- [68] S. L. Danilishin and F. Y. Khalili, *Living Reviews in Relativity* **15**, 1 (2012).
- [69] P. Barakhshan, A. Marrs, A. Bhosale, B. Arora, R. Eigenmann, and M. S. Safronova, *Portal for High-Precision Atomic Data and Computation* (version 2.0). University of Delaware, Newark, DE, USA. URL: <https://www.udel.edu/atom>.
- [70] H.-K. Guo, K. Riles, F.-W. Yang, and Y. Zhao, *Commun. Phys.* **2**, 155 (2019).
- [71] A. L. Miller, P. Astone, G. Bruno, S. Clesse, S. D'Antonio, A. Depasse, F. De Lillo, S. Frasca, I. La Rosa, P. Leaci, C. Palomba, O. J. Piccinni, L. Pierini, L. Rei, and A. Tanasijczuk, *Phys. Rev. D* **103**, 103002 (2021).
- [72] D. Carney, A. Hook, Z. Liu, J. M. Taylor, and Y. Zhao, *New Journal of Physics* **23**, 023041 (2021).